

GNSS inter-system bias estimation, modeling, and prediction

vorgelegt von

M.Sc.

Nan Jiang

von der Fakultät VI – Planen Bauen Umwelt
der Technischen Universität Berlin
zur Erlangung des akademischen Grades

Doktor der Ingenieurwissenschaften

– Dr.-Ing. –

genehmigte Dissertation

Promotionsausschuss:

Vorsitzender: Prof. Dr.-Ing. Jürgen Oberst

Gutachter: Prof. Dr.-Ing Harald Schuh

Gutachter: Prof. Dr.-Ing Robert Weber

Gutachter: Prof. Dr.-Ing Guochang Xu

Tag der wissenschaftlichen Aussprache: 17. Januar 2019

Berlin 2019

Abstract

Up to now, the precise point positioning (PPP) has stepped from the single system mode into the multi-GNSS combination. The key point of multi-GNSS integrated PPP is to carefully calibrate the inter-system-bias (ISB) between different systems. If ISB can be modeled, this error will be well corrected. It will significantly increase the usability of satellites and enhance compatibility and interoperability between different systems. The main objective of this thesis was to generate a high-accuracy ISB model that can calibrate the deviations between different satellite systems, and utilize the prediction ISB derived from this model as an a priori information to obtain benefits for the integrated PPP. In this context, effective methods, including the optimization choice of the function - and the stochastic model, and the preprocessing of precise clock products have been applied. The primary research approaches and the derived results of this thesis are summarized as follows:

Usually, the data processing models for ISB are divided into two categories. One represents the function model that mainly focuses on the parameter setting and error correcting. The second is the stochastic model, primarily dealing with the weight distribution and the precision configuration. Both directly determine the accuracy and reliability of the parameter estimation. Thus, two different function models for ISB estimation were investigated and analyzed, followed by the equivalence proof of these two models in theory. Then, data of GPS/BDS and GPS/Galileo constellations are used for revealing the numerical equivalence between these two functions. The results indicate they are closely resembling. Therefore, the equivalence of these two models is successfully verified, both in theory and numerical analysis. Thus, this part of the study guided us to choose a candidate for a functional model for the ISB estimation.

Four different stochastic models for ISB estimation have been assessed and studied. The results of convergence time and positioning accuracy indicated the highest accuracy and shortest convergence time would be achieved when the same ISB stochastic model in the PPP solutions as in the step of generation of the precise clock product executed by analysis centers (ACs) is applied. In other words, when using precise products from different ACs, the matched ISB stochastic model needs to be utilized.

Because ISB has a strong correlation with the satellite clock, a method of precise clock product preprocessing has to be deployed to detect and repair the ISB jumps. Here it was learned, the true reason for ISB jumps is caused by the extreme values (maxima and/or minima) of satellite clock data in the frequency domain. After all extreme points had been detected, we classified them into three types. To smooth the ISB jumps, a different preprocessing method for each kind of the extreme points have been used. The result of the ISB continuity processing depicts that ISB jumps can be effectively detected and repaired by the proposed method of the precise clock product preprocessing. Relying on this part of the study, a smooth and sequential ISB series could be achieved, as the basis for the consecutive modeling.

In the last step, a high accuracy and effective ISB model has been established. The test of the fitting accuracy denotes that the proposed ISB model has high fitting precision and is suitable for ISB prediction. After comparing the predicted ISB with the real ISB values, it was found that the prediction accuracy dropped day by day. Thus, the optimum prediction duration was set to one day. Three schemes, namely "Normal", "Cons", and "Fix" were designed to investigate the influence of the ISB model for the combined PPP. Compared with scheme "Normal" with ISB estimation, the convergence times of schemes "Cons." with ISB constraints and "Fix" with fixed ISB can be shortened mainly in the Up component, while they can achieve the same accuracy positioning level. In the case of poor observation conditions that likely occur in, e.g., urban areas, deep gorges, and forest areas, the integrated PPP using schemes

“Cons.” and “Fix” clearly indicate advantages over the “Normal” PPP mode because of the fewer parameter (ISB) estimations.

Keywords: GNSS; inter-system-bias; function model; stochastic model; ISB modeling; ISB prediction

Zusammenfassung

In den vergangenen 20 Jahren hat sich das Precise-Point-Positioning (PPP) vom Single-System-Modus zu einer Multi-GNSS-Kombination entwickelt. Der entscheidende Punkt bei Multi-GNSS-integrierten PPPs ist dabei die sorgfältige Kalibrierung des sogenannten Inter-System-Bias (ISB) zwischen den verschiedenen Systemen. Kann der ISB modelliert werden, sind Fehler sehr gut zu korrigieren. Dadurch wird die Nutzbarkeit von Satelliten erheblich erhöht und die Kompatibilität und Interoperabilität zwischen den verschiedenen Systemen verbessert. Das wesentliche Ziel dieser Arbeit war die Erstellung eines hochpräzisen ISB-Modells, das die Unterschiede zwischen verschiedenen Satellitensystemen kalibriert und dessen Vorhersagedaten a priori zur Optimierung der integrierten PPP nutzen kann. Dabei kamen effektive Methoden wie die Optimierung der Wahl des Funktionsmodells und des stochastischen Modells sowie die Vorverarbeitung der genauen Satellitenuhrprodukte zum Einsatz. Die wesentlichen Forschungsansätze und die Ergebnisse dieser Arbeit sind wie folgt zusammengefasst:

Normalerweise sind die Datenverarbeitungsmodelle in zwei Kategorien unterteilt: Eines stellt das Funktionsmodell dar, das hauptsächlich die Parametereinstellungen und die Fehlerkorrekturen steuert. Das andere ist das stochastische Modell, welches in erster Linie die Gewichtsverteilung und die Präzisionskonfiguration prozessiert. Beide zusammen bestimmen direkt die Genauigkeit und Zuverlässigkeit der Parameterschätzung. Zunächst wurden zwei verschiedene Funktionsmodelle für die ISB-Schätzung untersucht und analysiert. Zudem wird der Äquivalenznachweis dieser beiden Modelle theoretisch ermittelt. Anschließend werden Daten der GPS-Konstellationen BDS und Galileo verwendet, um die numerische Äquivalenz zwischen beiden Funktionen darzulegen. Die Ergebnisse ähneln einander sehr stark, wodurch die Gleichwertigkeit beider Modelle sowohl theoretisch als auch

numerisch erfolgreich überprüft wurde. Diese Teilstudie wurde nun genutzt einen Kandidaten für ein Funktionsmodell für die ISB-Schätzung auszuwählen.

In einem nächsten Schritt wurden vier verschiedene stochastische Modelle für die ISB-Schätzung bewertet und untersucht. Die Ergebnisse zeigten, dass bei Verwendung des gleichen ISB Stochastik Modells in den PPP-Lösungen wie im Schritt der Erzeugung eines genauen Uhrprodukts, das von Analysezentren (ACs) ausgeführt wird, die höchste Genauigkeit in der Positionierung und die kürzeste Konvergenzzeit erreicht werden. Daraus war abzuleiten, dass bei Verwendung der genauen Produkte verschiedener ACs, das passende stochastische ISB-Modell verwendet werden muss.

ISB weist eine hohe Korrelation zur Satellitenuhr auf. Daher wurde eine Methode der präzisen Vorverarbeitung von Uhrprodukten verwendet, um die ISB-Sprünge erkennen und reparieren zu können. Dabei stellte sich heraus, dass die ISB-Sprünge durch Extremwerte (Maxima und/oder Minima) der Satellitentaktdaten im Frequenzbereich verursacht werden. Nachdem alle Extrempunkte erkannt waren, wurden sie in drei Typen klassifiziert. Um die ISB-Sprünge zu glätten, wurde für jede Art des Extrempunkts eine andere Vorverarbeitungsmethode gewählt. Das Ergebnis der ISB-Kontinuität zeigt, dass ISB-Sprünge durch das vorgeschlagene Verfahren der präzisen Vorverarbeitung von Uhrprodukten effektiv erkannt und repariert werden können. Basierend auf diesem Teil der Studie konnte eine glatte und sequenzielle ISB-Serie prozessiert werden, die die Grundlage der folgenden ISB-Modellierung bildete.

In einem letzten Schritt wird ein hochgenaues und effektives ISB-Modell etabliert. Der Test der Passgenauigkeit zeigt an, dass das vorgeschlagene ISB-Modell eine hohe Genauigkeit aufweist und sich für die ISB-Vorhersage eignet. Bei einem Vergleich der vorhergesagten ISB mit realen ISB-Werten konnte festgestellt werden, dass die Vorhersagegenauigkeit von Tag zu Tag abnimmt. Somit wurde die optimale Vorhersagedauer auf einen Tag festgelegt. Mit drei verschiedenen Schemata ("Normal", "Cons" und "Fix") wurde

der Einfluss des ISB-Modells auf das kombinierte PPP untersucht. Verglichen mit dem Schema "Normal" mit ISB-Schätzung, können die Konvergenzzeiten der Schemata "Cons." mit ISB-Einschränkungen und "Fix" mit festem ISB hauptsächlich in der Up-Komponente verkürzt werden und dabei trotzdem das gleiche Genauigkeitsniveau in der Positionierung erreichen. Bei schlechten Beobachtungsbedingungen wie sie z.B. in Stadtgebieten, tiefen Schluchten und Waldgebieten vorkommen, hat das integrierte PPP mit den Schemata "Cons." und "Fix" Vorteile gegenüber dem "Normal" PPP-Modus, da weniger ISB Parameter abgeschätzt werden müssen.

Stichwörter: GNSS; Inter-System-Bias; Funktionsmodell; Stochastisches Modell; ISB-Modellierung; ISB Vorhersage

Table of Contents

Title Page	i
Abstract	iii
Zusammenfassung	vi
Table of Contents	ix
List of Abbreviations	xi
List of Figures	xiii
List of Tables	xvii
1 Introduction	1
1.1 Research background	1
1.1.1 Global navigation satellite systems	1
1.1.2 Multi-GNSS combined PPP and inter-system bias	10
1.2 Motivation	12
1.3 Main contributions	14
1.4 Overview of the dissertation	15
2 Multi-GNSS data models and processing	17
2.1 Introduction	17
2.2 GNSS observations	17
2.2.1 Code pseudorange	17
2.2.2 Carrier phase	19
2.3 GNSS error sources	21
2.3.1 Errors associated with the satellite	23
2.3.2 Errors associated with the receiver	29
2.3.3 Errors related to signal propagation	32
2.4 Models of precise point positioning	35
2.4.1 PPP function model	35
2.4.2 Stochastic model of PPP	38
2.5 Parameter estimation	39
2.5.1 Least squares	39
2.5.2 Kalman filter	41
3 Two different function models for ISB estimation and equivalence proof	44
3.1 Introduction	44
3.2 Methodology and equivalence proof	44
3.2.1 Function model of independent system	45
3.2.2 Function model of dependent system	47
3.2.3 Equivalence of two models	48
3.3 Experiment and analysis of results	51
3.3.1 Comparison of positioning accuracy and convergence time	53

3.3.2	Comparison of different estimated ISB	58
3.4	Summary	63
4	Assessment of different stochastic models for ISB.....	65
4.1	Introduction	65
4.2	Descriptions of ISB stochastic models.....	66
4.3	Experimental data and processing strategies	68
4.4	Results and discussion	70
4.4.1	Pseudorange observation residuals	71
4.4.2	Convergence time and positioning accuracy.....	74
4.4.3	Accuracy improvement during the convergence period	81
4.4.4	Comparison of estimated ISBs	82
4.5	Summary	84
5	Preprocessing of satellite clock product for ISB jumps detecting and repairing .	86
5.1	Introduction	86
5.2	Experimental data and processing strategies	86
5.3	The relationship between ISB and satellite clock and clock preprocessing.....	88
5.3.1	The correlation verification between ISB and satellite clock in the time domain	89
5.3.2	Convert the satellite clock data (time domain) into the frequency domain	95
5.3.3	Detection of small extrema of CFD.....	97
5.3.4	Classification of extrema of CFD and clock preprocessing	98
5.3.5	Improvement of continuity of ISB.....	102
5.4	Summary	107
6	Inter-system bias modeling and prediction	109
6.1	Introduction	109
6.2	Experimental data.....	109
6.3	Estimation model and processing strategy	111
6.3.1	PPP model for ISB estimation	111
6.3.2	ISB modeling and coefficients estimation.....	115
6.4	Results and discussion	116
6.4.1	Impacts of convergence period for ISB estimation	117
6.4.2	Elimination of ISB day jumps and smoothing	120
6.4.3	ISB modeling	125
6.4.4	ISB prediction with the model	132
6.4.5	Analysis of convergence time and PPP accuracy	136
6.5	Summary	140
7	Conclusions and outlooks.....	142
7.1	Conclusions	142
7.2	Outlooks.....	145
	References:	146
	Acknowledgments	155

List of Abbreviations

AC	Analysis Center
BDS	the Chinese BeiDou Navigation Satellite System
CDMA	Code Division Multiple Access
CFD	Clock Frequency Data
DFT	Discrete Fourier Transform
DI	Data Interrupt
DOY	Day of Year
ECEF	Earth-Centered Earth-Fixed
EKF	Extended Kalman Filter
ESA	the European Space Agency
EU	European Union
FDMA	Frequency Division Multiple Access
FFT	Fast Fourier Transform
FM	Frequency Modulation
Galileo	the European Union Satellite Navigation System
GBM	MGEX Precise Product from GFZ
GC	GPS and BDS
GE	GPS and Galileo
GEO	GEostationary Orbit
GF	Geometry-Free
GFZ	GFZ German Research Centre for Geosciences
GIOVE	Galileo In-Orbit Validation Element
GLONASS	the Russian GLObal NAVigation Satellite System
GMF	Global Mapping Function
GNSS	Global Navigation Satellite System
GPS	Global Positioning System
HMW	Hatch-Melbourne-Wubben
IF	Ionospheric-Free
IFCM	Ionosphere-Free Combination Model
IGS	the International GNSS Service
IGSO	Inclined GeoSynchronous Orbit
IGU	IGS Ultra-rapid product (IGU)
IRNSS	Indian Regional Navigation Satellite System
ISB	Inter-System Bias
ISB_m	The Modeled ISB
ISB_o	Original ISB Series
ISB_p	Processed ISB Series

ISB_p	The Predicted ISB
ISB_s	Smoothed ISB Series
JPO	the Joint Project Office
LS	Least Squares
MDS	Model of Dependent System
MEO	MEdium Orbit
MGEX	Multi-GNSS Experiment
MGEX	The Multi-GNSS Experiment
MIS	Model of Independent System
NMF	Niell Mapping Function
PCO	Phase Center Offset
PCV	Phase Center Variation
PM	Phase Modulation
PPP	Precise Point Positioning
PWV	Precipitable Water Vapor
QZSS	Quasi-Zenith Satellite System
RHCP	Right Hand Circular Polarization
RMS	Root Mean Square
SBAS	Space-Based Augmentation Systems
SNR	Signal-To-Noise Ratio
STD	Slant Total Delay
STD	Standard Deviation
UCM	Un-Combined Model
VMF	Vienna Mapping Function
WUH	Wuhan University
WUM	MGEX Precise Product from WUH
ZHD	Zenith Hydrostatic Delay
ZTD	Zenith Total Delay
ZWD	Zenith Wet Delay

List of Figures

- Figure 3.1** The convergence time in two scheme MIS and MDS, the subgraph (a) GC means the convergence results for GPS and BDS processing, and the GPS and Galileo processing convergence time is presented in the sub-image (b) GE. 54
- Figure 3.2** The weekly mean RMS of positioning errors in the two scheme MIS and MDS with GPS and BDS observations, the bottom subgraph shows the distribution of stations, and the top two subgraphs from up to down are the enlarged details for the mean RMS in north, east and up component, respectively. 55
- Figure 3.3** The weekly mean RMS of positioning errors in two schemes MIS and MDS with GPS and Galileo observations. 58
- Figure 3.4** The ISB difference between GPS/BDS for two schemes (8 stations with two different types of receivers, the upper four stations are Trimble, and the under four are SEPT, due to space limitation, only 4 days are shown as an example, unit: ns). 59
- Figure 3.5** The ISB difference between GPS/Galileo for two schemes (6 stations with two different types of receivers, the upper four stations are Trimble, and the under two are SEPT, due to space limitation, only 4 days are shown as an example, unit: ns). 60
- Figure 3.6** The estimated ISB in GPS/BDS systems (8 stations with two different types of receivers, the upper four stations are Trimble, and the under four are SEPT, due to space limitation, the ISB from MIS in 4 days are shown as an example, unit: ns). 61
- Figure 3.7** The daily mean, weekly mean difference, and the weekly mean STD of ISB increment between two schemes, up subfigure (a) is the description of GPS and BDS systems, while the down sub-picture (b) is about GPS and Galileo systems. The weekly mean value is in a wine column, and the right vertical axis shows the weekly mean STD, unit: ns. 62
- Figure 4.1** Distribution of the selected stations. 69
- Figure 4.2** Ionospheric-free pseudorange observation residuals of GPS and BDS systems at STR1 station as an example on DOY 251, 2017, here is the results of the first 3h period with static PPP mode, left column is the GPS system, the right one denotes the BDS system, from top to bottom represents different schemes. 72
- Figure 4.3** Ionospheric-free pseudorange observation residuals of GPS and BDS systems at STR1 station as an example on DOY 251, 2017, it is the results for the first 3h period with kinematic PPP mode. 73

Figure 4.4 GPS/BDS combined static PPP convergence performance in five different schemes with <i>GBM</i> precise products, each scheme uses a different color, left side is the errors of 95% quantile, while the right side is the errors of 68% quantile.	75
Figure 4.5 GPS/BDS combined kinematic PPP convergence performance with five different schemes.	77
Figure 4.6 GPS/BDS combined kinematic PPP convergence performance in five different schemes using precise products from <i>WUM</i>	80
Figure 4.7 The estimated ISBs derived from the four different schemes with considering ISB using the <i>GBM</i> products. Different ISBs are shown in different colors. The top subfigure displays the results for the static mode, while the bottom on is the results for the kinematic mode.....	83
Figure 4.8 The estimated ISBs using the <i>WUM</i> products in the kinematic mode. Different ISBs derived from the different schemes with considering ISB are shown in different colors	84
Figure 5.1 Geographic distribution of GPS/BDS Stations, three stations with “TRIMBLE” receivers are in red, those installed with “LEICA” receivers are in blue, the rest three stations are shown in green with the receiver type of “SEPT”.....	87
Figure 5.2 Estimated ISB of stations CUT0, JFNG, SIN1, HKOH, HKSL, HKWS, MAJU, NAUR, and NNOR. The left bottom sub-figure is the enlarged view of ISB during the epochs 4800-6400, i.e., August 17-22, 2015.....	89
Figure 5.3 Satellite clock offsets of BDS in the time domain during August 2015, in the right part of each subfigure is the satellite ID, from C01 to C14 without C13, the vertical axis is colored in black and wine intervals for a clearer view.....	90
Figure 5.4 ISB differences and satellite clock residuals in adjacent days–pairs 17-18, 18-19, 19-20, 20-21, the left subfigure with wine color vertical axis is the ISB differences, and the right one with a blue color vertical axis is the satellite clock offset residual.....	93
Figure 5.5 Clock frequency data of BDS satellites during August 2015, the satellite ID is included in the top right corner of each panel, from C01 to C14 excluding C13, the vertical axis is colored in black and blue intervals for a clearer view.	97
Figure 5.6 Flow chart of satellite clock preprocessing	99
Figure 5.7 Clock frequency data extremum points caused by three different reasons, i.e., clock day boundary, switch of the reference clock, and small PM with diverse colors and symbols, during August 2015.....	101
Figure 5.8 Re-estimated ISB with the processed satellite clock product of stations CUT0, JFNG, SIN1, HKOH, HKSL, HKWS, MAJU, NAUR, and NNOR.	102

Figure 5.9 Subfigure (a) are the original ISB series of stations CUT0, JFNG, SIN1, HKOH, HKSL, HKWS, MAJU, NAUR, and NNOR; mean value and its standard deviation of stations CUT0, HKOH, MAJU from August 17 to 21 are shown in subfigure (b). 104

Figure 5.10 ISB series derived from the processed precise clock product of stations CUT0, JFNG, SIN1, HKOH, HKSL, HKWS, MAJU, NAUR, and NNOR are illustrated in subfigure (a); subfigure (b) is the mean value and its standard deviation of stations CUT0, HKOH, MAJU from August 17 to 21..... 105

Figure 5.11 Continuity factor in two schemes ((a) is scheme (a), (b) means scheme (b)) of stations CUT0, HKOH, MAJU with different symbols, and the orange line denotes the critical value of standard normal distribution with a significance level of 0.01. 106

Figure 6.1 Distribution of 26 stations in the MGEX network..... 111

Figure 6.2 The ISB series of station KRGG on Oct. 15, 2017, in the 5min interval as an example, the black curve is the ISB between GPS and BDS, and the blue one is the ISB between GPS and Galileo, in the red box is the convergence period of ISB..... 118

Figure 6.3 Weekly mean STD comparison of ISB between forward and combined filter, (a) is the consequence of GC case, while (b) is the GE case, the blue color column shows the STD of forward filter, and the STD of the combined filter is indicated as wine color column. 119

Figure 6.4 Original ISB series during GPS week 1971 in GC case, taking stations FTNA, KRGG, LAUT, MAJU, MAL2, and PTVL for example..... 121

Figure 6.5 Original ISB series during GPS week 1971 in GE case, with the use of stations CAS1, KRGG, MAJU, MAL2, POHN, and REUN as an example..... 121

Figure 6.6 Processed ISB series without day jumps during GPS week 1971 in GC case, taking stations FTNA, KRGG, LAUT, MAJU, MAL2, and PTVL for example..... 123

Figure 6.7 Processed ISB series without day jumps GPS week 1971 in GE case, with the use of stations CAS1, KRGG, MAJU, MAL2, POHN, and REUN as an example. 123

Figure 6.8 Comparison of processed ISB and smoothed ISB for GC case in GPS week 1971, ISB_p is shown in blue color, while the wine color denotes ISB_s. 124

Figure 6.9 Comparison of processed ISB and smoothed ISB for GE case in GPS week 1971, ISB_p is presented in blue color, while the wine color represents ISB_s. 125

Figure 6.10 Smoothed (ISB_s) and modeled (ISB_m) series during GPS week 1971 at stations FTNA, KRGG, LAUT, MAJU, MAL2, and PTVL for the 30 min sampling interval in GC case. 128

Figure 6.11 Smoothed (ISB_s) and modeled (ISB_m) series during GPS week 1971 at stations CAS1, KRGG, MAJU, MAL2, POHN, and REUN for the 30 min interval in GE case.	129
Figure 6.12 Distribution of the differences derived from modeled and smoothed ISB between GPS and BDS (GC) during GPS week 1971 at stations FTNA, KRGG, LAUT, MAJU, MAL2, PTVL.	130
Figure 6.13 Distribution of the differences derived from modeled and smoothed ISB between GPS and Galileo (GE) during GPS week 1971 at stations CAS1, KRGG, MAJU, MAL2, POHN, REUN.	130
Figure 6.14 The comparison between predicted ISB (ISB_p) and the smoothed ISB (ISB_s) during the period of GPS week 1972 in the stations of FTNA, KRGG, LAUT, MAJU, MAL2, and PTVL for GC case.	133
Figure 6.15 The comparison between predicted ISB (ISB_p) and the smoothed ISB (ISB_s) during the period of GPS week 1972 in the stations of CAS1, KRGG, MAJU, MAL2, POHN, and REUN for GE case.	134
Figure 6.16 Comparison of the convergence time with three schemes (“Normal” in wine color column is the scheme 1, “Cons.” in blue color indicates scheme 2, and “Fix” with orange color denotes scheme 3) in N, E, and U components at stations FTNA, KRGG, LAUT, MAJU, MAL2, and PTVL on Oct. 22, 2017 for GC case.	137
Figure 6.17 Comparison of the convergence time with three schemes (“Normal” in red color column indicates the scheme 1, “Cons.” in olive color denotes scheme 2, and “Fix” with violet color is a representation of scheme 3) in N, E, and U components at stations CAS1, KRGG, MAJU, MAL2, POHN and REUN on Oct. 22, 2017 for GE case.	138

List of Tables

Table 1.1 The current status of the GPS system (up to Dec. 31 st , 2018).	3
Table 1.2 The current status of the GLONASS system (up to Dec. 31 st , 2018).....	5
Table 1.3 The current status of the Galileo system (up to Dec. 31 st , 2018).....	6
Table 1.4 The current status of the BDS system (G means GEO, I is IGSO, M denotes MEO, up to Dec. 31 st , 2018)	8
Table 1.5 The current status of QZSS system (up to Dec. 31 st , 2018)	9
Table 1.6 The current status of IRNSS system (up to Dec. 31 st , 2018).....	10
Table 3.1 The details of eight stations used in the test.....	51
Table 3.2 The models and strategies for data processing.	52
Table 3.3 The positioning RMS in the north, east, up components in two schemes with GPS and BDS observations (unit: cm).	56
Table 3.4 The positioning RMS in North, East, Up components in two schemes with GPS and Galileo observations (unit: cm).	57
Table 4.1 The description of GPS/BDS ISB estimating schemes.....	68
Table 4.2 Details of 8 selected stations location and receiver types.	69
Table 4.3 Models and strategies for data processing	70
Table 4.4 Convergence times of GPS and BDS combined static and kinematic PPP in five different schemes (unit: min)	75
Table 4.5 Positioning accuracy of GPS/BDS combined static and kinematic PPP with five different schemes (unit: cm).	78
Table 4.6 Convergence time and positioning accuracy of GPS/BDS combined kinematic PPP with the <i>WUM</i> products in five different schemes.....	81
Table 4.7 Positioning accuracy of GPS/BDS combined kinematic PPP during the convergence period (8min and 16min) in five different schemes with <i>GBM</i> precise products (unit: cm).	81
Table 4.8 Positioning accuracy of GPS/BDS combined kinematic PPP during the convergence period (8min and 16min) in five different schemes with <i>WUM</i> precise products (unit: cm).	82

Table 5.1 Station ID, receiver types, firmware version, and location at 9 stations.....	88
Table 5.2 The time Statistics of data interrupt (DI) and phase modulation (PM) of BDS satellites in August 2015, in the table we only list the day in August without the month number to simplify the space, satellites C08, C09, C10, C14 have no DI and PM, so they are not listed in the table.....	90
Table 5.3 ISB differences statistics in 9 stations at the days-pairs of 17-18, 18-19, 19-20, 20-21 (unit: ns).....	94
Table 5.4 Satellite clock offset residuals statistics at the days-pairs of 17-18, 18-19, 19-20, 20-21 for BDS satellites (unit: ns).	94
Table 5.5 Correlation coefficients between ISB differences and satellite clock offset residuals, the values in the table are listed as the increments to 1, the smaller the value, the closer it is to 1 (unit: 10^{-5}).	95
Table 5.6 Time statistics of three different types of extremum points appeared in BDS clock frequency data. If the extremum point is detected at the time of first epoch of one day, only the day in Aug. 2015 is listed. The blank means there is no extremum point detected for this satellite.....	100
Table 5.7 Continuity statistics of ISB in different days-pairs (August 17-28, 18-19, 19-20, 20-21), two different continuity factors derived from two diverse schemes are listed. Here scheme (a) is the original ISB series without any processing, ISB series with clock product preprocessing is obtained in the scheme (b). The Continuity factors got from these two kinds of ISB are listed as follows.	107
Table 6.1 Observation models and data processing strategies for combined PPP.	115
Table 6.2 The details of 9 chosen stations, including locations, receiver types, and the clock type inside receiver.	117
Table 6.3 Statistics of daily and mean ISB from forward and combined filter in GC case, f means forward filter, while c is combined filter, unit: ns.	119
Table 6.4 Statistics of daily and mean ISB from forward and combined filter in GE case, f means forward filter, while c is combined filter, unit: ns.	120
Table 6.5 The coefficients estimated by LS for the polynomial and periodic functions in GC case, A , B , and C are quadratic, first-order, and constant terms of the polynomial; in addition, D_i and E_i denote the coefficients of the periodic functions, and P_i means the coefficients of the periods.	126
Table 6.6 The coefficients estimated by LS for the polynomial and periodic functions in GE case.	127

Table 6.7 The statistics of the fitting accuracy of the proposed model in the GC case at stations FTNA, KRGG, LAUT, MAJU, MAL2, PTVL (unit: ns).....	131
Table 6.8 The statistics of the fitting accuracy of the proposed model in the GE case at stations CAS1, KRGG, MAJU, MAL2, POHN, REUN (unit: ns).....	132
Table 6.9 Statistics of predictions for GC ISB from the first day to the seventh day in GPS week 1972 from Oct. 22 to 28 (from 1 st day to 7 th day), 2017 (unit: ns).....	135
Table 6.10 Statistics of predictions for GE ISB from the first day to the seventh day in GPS week 1972 from Oct. 22 to 28 (from 1 st day to 7 th day), 2017 (unit: ns).....	135
Table 6.11 Statistics of the accuracy of combined PPP for the GC case with different schemes in N, E, and U components (unit: cm).....	139
Table 6.12 Statistics of the accuracy of combined PPP for the GE case with different schemes in N, E, and U components (unit: cm).....	139

1 Introduction

Backed by over 20 years of development, precise point positioning (PPP) plays a growingly significant important role in the area of geodesy and other applications, for instance, GNSS meteorology and GNSS seismology. In early days, the normal PPP mode made use of data from a single system only, like GPS, or GLONASS. Nevertheless, during the past few decades, through the deployment of more satellite systems, for instance, BDS in China and Galileo in the EU, GNSS systems have undergone rapid growth. In addition to these global navigation systems, there are also some regional systems under development, for instance, QZSS from Japan and IRNSS from India. Owing to the fast-paced development of multiple GNSS systems, PPP technology has transitioned into using the multi-GNSS combined mode. Integrated multi-GNSS positioning has the capability to enhance performance. The key to combining data from different systems, together with resolving differences between the two systems, is the appropriate calibration of the inter-system bias (ISB) since the ISB between different system observations has different attributes. In this thesis, the features, estimation, modeling, and prediction of the ISB are going to be investigated and studied comprehensively. The background and motivations of this research, the main contributions, and a description of the contents of this thesis are put forward in this chapter.

1.1 Research background

1.1.1 Global navigation satellite systems

GNSS technology started back in the early 1970s with the launch of the primary system of GPS. Being a new space technology, GNSS not just plays a fundamental role in military defense but is also put to extensive uses in agriculture, forestry and animal husbandry, transportation, energy, electric power, geological exploration, disaster monitoring, environmental protection, and other sectors and fields. Following approximately 40 years,

GNSS has undergone extensive development and innovation in the methodology of process technology and data processing.

The modernization of GPS

The GPS project is subjected to the leadership of the U.S. Department of Defense, besides being built by the Joint Project Office (JPO). It is a navigation and positioning system that, at any time, is capable of determining the 3D position, speed, and timing of a signal. The system became fully operational on July 17, 1995. Owing to the advances in technology, coupled with consumer demand for precision, and the need for gaining a competitive advantage over other navigation positioning systems, the United States made an announcement of a modernization program for GPS on January 25, 1999, the program of GPS modernization, which is segregated into three stages:

First stage: Launch of Block IIR-m (Modernized Type) satellite. A second GPS civil signal L2C is broadcast for the purpose of improving the efficiency of commercial applications. Two new M code military signals are incorporated for the enhancement of the anti-blocking capability of military signals. The signal provides flexible transmission power for the army.

Second stage: Launch of Block IIF (Follow-on Type) satellite. A third civil signal L5C is provided for the transport security services. A satellite design life of 12 years is attained, besides implementing a higher precision atomic clock is implemented.

Third stage: Launch of Block III type satellite. A fourth GPS Civil signal L1C is broadcast for the international interoperability applications. The life of the newest satellite design is 15 years. The satellite serves as distress alerting satellite system for the search and rescue services. Inter-satellite links are applied for the achievement of faster command upload, in addition to lowering the data transmission period.

GPS is expected to have three carrier phase signals with different frequencies following the modernization, and the anti-interference performance is expected to become more robust

as well. Nowadays, there are 31 satellites residing the orbit of the GPS system, which include 12 Block IIR satellites, besides 7 Block IIR-M satellites, and 12 Block IIF satellites. The GPS status is presented in Table 1.1. The first Block III satellite (SVN74) was launched by SpaceX on 23 December 2018, which is currently under testing (<https://spaceflightnow.com/2018/12/23/spacex-closes-out-year-with-successful-gps-satellite-launch/>).

Table 1.1 The current status of the GPS system (up to Dec. 31st, 2018).

Launch time	Type	PRN	Launch time	Type	PRN	Launch time	Type	PRN
97-07-23	IIR	13	04-11-06	IIR	02	12-10-04	IIF	24
99-10-07	IIR	11	05-09-26	IIR-M	17	13-05-15	IIF	27
00-05-11	IIR	20	06-09-25	IIR-M	31	14-02-21	IIF	30
00-07-16	IIR	28	06-11-17	IIR-M	12	14-05-17	IIF	06
00-11-10	IIR	14	07-10-17	IIR-M	15	14-08-02	IIF	09
01-01-30	IIR	18	07-12-20	IIR-M	29	14-10-29	IIF	03
03-01-29	IIR	16	08-03-15	IIR-M	07	15-03-25	IIF	26
03-03-31	IIR	21	09-03-24	IIR-M	04*	15-07-15	IIF	08
03-12-21	IIR	22	09-08-17	IIR-M	05	15-10-31	IIF	10
04-03-20	IIR	19	10-05-28	IIF	25	16-02-05	IIF	32
04-06-23	IIR	23	11-07-16	IIF	01	18-12-23	IIIA	04

(* Satellite PRN 04 was out of service on May 6th, 2011)

The revitalization of GLONASS

GLONASS system is a global navigation satellite system developed by Russia that has similar functions as GPS. The first test satellite was launched into space on Oct 12, 1982. The full constellation of 24 satellites was completed on Jan 18, 1996. Nevertheless, for the economic decline of Russia that occurred between 1996 and 1998, the number of satellites in orbit is gradually declining; at the lowest period, only six GLONASS satellites had the capability to work, so there were no global navigation and positioning service capabilities at that time. As a

matter of luck, exploiting the development of the oil economy, the Russian government implemented a supplementary satellite plan as well as the modernization of the GLONASS system. Subsequent to that, the GLONASS system recovered gradually.

Early in the design of the GLONASS system, Russia showed more concerns with the anti-jamming capability of the system. Accordingly, the frequency division multiple access (FDMA) signal was adopted that augmented the complexity of the system, together with lowering the compatibility with other navigation systems. For the purpose of enhancing the competitiveness and compatibility of GLONASS, Russia has also started modernizing the GLONASS satellite, and the signal was switched to the code division multiple access (CDMA) like the GPS system. This effectively enhanced the compatibility of GLONASS, besides its navigating and positioning performance. One of the pivotal symbols of GLONASS modernization is the design of GLONASS-K satellites, which has CDMA signals-L1, L2, L3- at three different frequencies, in addition to still containing the currently existing FDMA signal. The initial plan involved launching the completely designed-from-scratch GLONASS-K2 satellites generation by the year 2014; nevertheless, the plan was adjusted, and the first launch was postponed to the year 2018. The GLONASS-K2 satellites are expected to have a 10-year design life, coupled with the clock stability of $\sim 5 \times 10^{-14} - 1 \times 10^{-14}$ s. Besides CDMA signals on L3, CDMA signals will also be transmitted on L1 and L2. The process of GNSS satellites modernization is demonstrated in Figure 1.1.

Currently, there are 24 satellites in the system, basically realizing the capability of global continuous navigation and positioning (https://en.wikipedia.org/wiki/List_of_GLONASS_satellites). Table 1.2 sheds light on the details of the satellites.

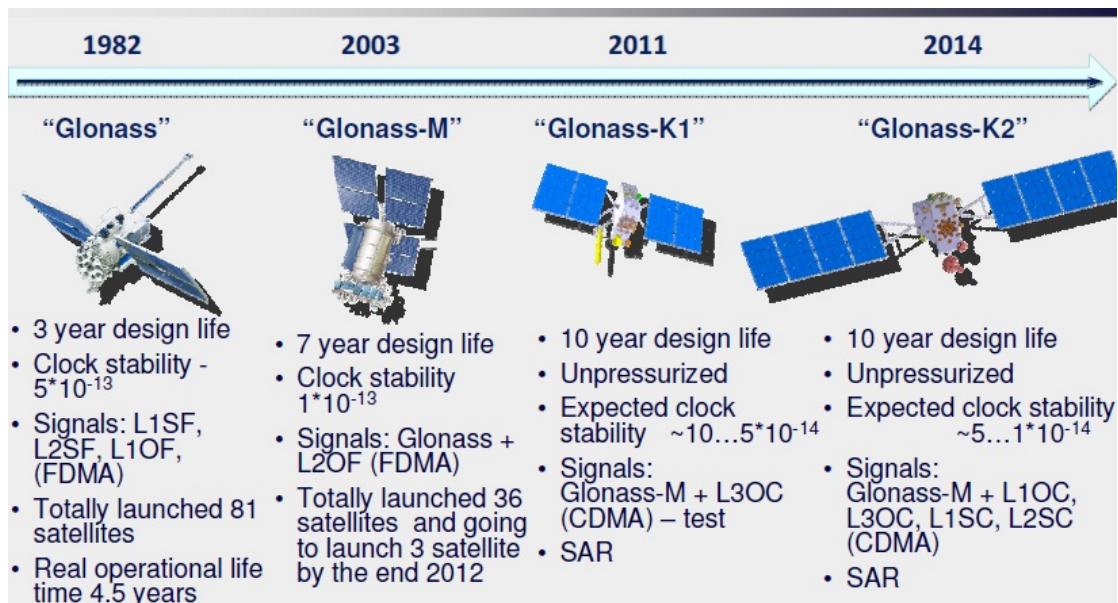


Figure 1.1 Process of GNSS satellites modernization.

Table 1.2 The current status of the GLONASS system (up to Dec. 31st, 2018).

Launch time	Type	PRN	Launch time	Type	PRN	Launch time	Type	PRN
06-12-25	M	10	10-03-01	M	23	14-03-23	M	18
07-10-26	M	20	10-03-01	M	24	14-06-14	M	21
07-10-26	M	19	10-09-02	M	16	14-11-30	K1	09
07-12-25	M	13	11-10-02	M	04	16-02-07	M	17
07-12-25	M	12	11-11-04	M	08	16-05-29	M	11
14-12-09	M	01	11-11-04	M	03	17-09-22	M	14
14-12-09	M	06	11-11-04	M	07	18-06-17	M	05
10-03-01	M	22	13-04-26	M	02	18-12-03	M	15

The development of Galileo

The European Union (EU) and the European Space Agency (ESA) launched the Galileo navigation satellite system project in March 2002, together with showing commitment to the establishment of Europe's own satellite navigation and positioning system. It could have full compatibility with the existing GPS and GLONASS systems, together with realizing

interoperability and combination positioning functions between different navigation systems (<http://www.satellite-navigation.eu/>). The Galileo system design constellation contains 30 satellites, with 27 of them working, besides three other satellites on standby. The entire constellation was originally scheduled to be completed between 2006 and 2010, with the service to be officially provided in the year 2010. Nonetheless, for the political and economic reasons, the building of the Galileo system was far less efficient as compared with the planned one, and the launching of satellites has undergone delays a number of times. Two in-orbit test satellites GIOVE-A and GIOVE-B (Galileo In-Orbit Validation Element, GIOVE) were launched on Dec 28, 2005, and Apr 12, 2008, correspondingly, aimed at capturing the frequency of the signal transmission and carrying out the satellite system testing. Thereafter, four in-orbit test satellites (Galileo-IOV) were launched on Oct 21, 2011, and Oct 12, 2012, for the purpose of carrying out the in-orbit verification of the system positioning and timing. Since the year 2014, a number of fully operational satellites (Galileo-FOC) have been launched. Till today, there are 18 satellites in orbit-14 satellites that are operational; 3 of them are Galileo-IOV, 11 of them are Galileo-FOC, and the other 4 satellites (Galileo-FOC) are under commission (https://en.wikipedia.org/wiki/List_of_Galileo_satellites). The current status of the Galileo system is presented in Table 1.3.

Table 1.3 The current status of the Galileo system (up to Dec. 31st, 2018)

Launch time	Type	PRN	Launch time	Type	PRN	Launch time	Type	PRN
11-10-21	IOV	11	16-05-24	FOC	01	17-12-12	FOC	27
11-10-21	IOV	12	16-05-24	FOC	02	17-12-12	FOC	31
12-10-12	IOV	19	16-11-17	FOC	07	18-07-25	FOC	36
15-03-27	FOC	26	16-11-17	FOC	03	18-07-25	FOC	13
15-09-11	FOC	24	16-11-17	FOC	04	18-07-25	FOC	15
15-09-11	FOC	30	16-11-17	FOC	05	18-07-25	FOC	33
15-12-17	FOC	08	17-12-12	FOC	21			
15-12-17	FOC	09	17-12-12	FOC	25			

The fast development of BDS

The Beidou satellite navigation system is a global satellite navigation system developed by China. The entire project construction plan is gradually realized in three stages, from the active positioning in China to the passive positioning in the Asia-Pacific region, and eventually, to the passive positioning across the globe. It is named the "three steps" development plan of the Beidou navigation system (<http://www.beidou.gov.cn>).

The first step is the Beidou test navigation satellite system. China started the Beidou satellite navigation test system in the year 1994. In 2000, two test Beidou satellites were successfully launched, indicating that the initial Beidou test system was completed. The third Beidou navigation test satellite was launched in 2003, further enhancing the performance of Beidou test system. The space constellation part of the Beidou test navigation satellite system contains 3 Geostationary Orbit (GEO) satellites, which are fixed at 80°E, 110.5°E and 140°E longitude (Yang 2010b).

The second step is the Beidou regional service navigation system. In the year 2004, China started building the second-generation Beidou navigation system, aiming at the navigation service capability of both China and the Asia-Pacific region. The Beidou second-generation system launched the first medium earth orbit satellite in 2007. Since the year 2009, several satellites have been launched continuously. Regional navigation and positioning service capabilities were realized in the Asia-Pacific region on December 27, 2012. The Beidou second-generation navigation satellite system counts on 5 GEO satellites, in addition to 5 Inclined Geosynchronous Orbit (IGSO) satellites, and 4 Medium Orbit (MEO) satellites. All of the satellites broadcast B1, B2, and B3 signals (Shi et al. 2012b; Yang et al. 2014). The GEO satellite is equipped with c-band communications as well as two-way satellite timing and frequency transfer equipment, which are capable of serving the users with short message communication and timely delivery service.

The third step is the global navigation system. The third-generation Beidou navigation system will be gradually established based on the second-generation and is expected to be accomplished by the end of 2020. The system constellation is expected to contain 5 GEO satellites, together with 3 IGSO satellites, and 27 MEO satellites, totaling 35 satellites, aimed at attaining the global navigation and positioning and timing service capability. BDS is the first system that makes use of GEO, IGSO, and MEO a mixed constellation of three different orbits, wherein the entire constellation broadcasts three frequency signals (Montenbruck et al. 2014).

Table 1.4 The current status of the BDS system (G means GEO, I is IGSO, M denotes MEO, up to Dec. 31st, 2018)

Launch time	Type	PRN	Launch time	Type	PRN
10-01-16	BDS-2-G1	C01	17-11-05	BDS-3 M1	C19
10-06-02	BDS-2-G3	C03	17-11-05	BDS-3 M2	C20
10-07-31	BDS-2-IGSO1	C06	18-01-11	BDS-3 M7	C27
10-10-31	BDS-2-G4	C04	18-01-11	BDS-3 M8	C28
10-12-17	BDS-2-IGSO2	C07	18-02-12	BDS-3 M3	C21
11-04-09	BDS-2-IGSO3	C08	18-02-12	BDS-3 M4	C22
11-07-26	BDS-2-IGSO4	C09	18-03-29	BDS-3 M9	C29
11-12-01	BDS-2-IGSO5	C10	18-03-29	BDS-3 M10	C30
12-02-24	BDS-2-G5	C05	18-07-29	BDS-3 M5	C23
12-04-29	BDS-2-M3	C11	18-07-29	BDS-3 M6	C24
12-04-29	BDS-2- M4	C12	18-08-24	BDS-3 M11	C25
12-09-18	BDS-2- M6	C14	18-08-24	BDS-3 M12	C26
12-10-25	BDS-2- G6	C02	18-09-19	BDS-3 M13	C32
15-03-30	BDS-3 I1-S	C31	18-09-19	BDS-3 M14	C33
15-07-25	BDS-3 M1-S	C33	18-10-15	BDS-3 M15	C34
15-07-25	BDS-3 M2-S	C34	18-10-15	BDS-3 M16	C35
15-09-29	BDS-3 I2-S	C32	18-11-18	BDS-3 M17	C36
16-02-01	BDS-3 M3-S	C35	18-11-18	BDS-3 M18	C37
16-03-29	BDS-2-IGSO6	C13			
16-06-12	BDS-2-G7	C17			

Five new-generation BeiDou-3 experimental satellites, termed as BeiDou-3e, which include 2 IGSO and 3 MEO satellites, have been launched since March 2015 (Zhao et al. 2017). At the end of 2017 and the beginning of 2018, four satellites from the newest generation BeiDou-3 (MEO) have been launched in a successful manner. All through the year 2018, 16 BeiDou-3 satellites were successfully launched as well (<http://www.beidou.gov.cn/>), accordingly totaling 18 Beidou-3 satellites in orbit. The current status of the BDS system is presented in Table 1.4.

The development of QZSS

The Quasi-Zenith Satellite System (QZSS) is a Japanese satellite positioning system that primarily comprises quasi-zenith-orbit satellites. In the year 2002, the Japanese government, by means of a comprehensive science and technology conference, took a formal decision for developing a national project for the satellite system, the QZSS (Ishijima et al. 2009). The plan of the QZSS involved launching 8 satellites, which guaranteed that at least one QZSS satellite is over Japan at any time. The QZSS system has the capability of effectively covering not only Japan but also the neighboring Asia-Pacific region, together with broadcasting GPS signal and enhanced information, equipped with navigation, positioning, and mobile communication functions that could effectively improve GPS navigation and positioning performance. Now, the QZSS system comprises three satellites in an inclined geosynchronous orbit, coupled with one satellite in geostationary orbit, which are presented in Table 1.5.

Table 1.5 The current status of QZSS system (up to Dec. 31st, 2018)

Launch time	Type	PRN	Common Name
10-09-11	IGSO	J01	QZS-1
17-06-01	IGSO	J02	QZS-2
17-08-19	GEO	J07	QZS-3
17-10-09	IGSO	J03	QZS-4

The development of IRNSS

In July 2006, the Indian space research institute made an announcement that it had the plan of establishing the Indian Regional Navigation Satellite System (IRNSS). It is an autonomous regional satellite navigation system, providing real-time positioning as well as timing services. It encompasses India, in addition to a region extending 1,500 km surrounding India, planned to expand further. The system currently comprises a constellation of 8 satellites, wherein three of them are in geostationary orbit (GEO), and five reside in an inclined geosynchronous orbit (IGSO). All satellites launched or proposed for the system are listed as hereunder:

Table 1.6 The current status of IRNSS system (up to Dec. 31st, 2018)

Launch time	Type	Satellite	Status
13-07-01	IGSO	IRNSS-1A	Failed in orbit
14-04-04	IGSO	IRNSS-1B	Operational
14-10-15	GEO	IRNSS-1C	Operational
15-03-28	IGSO	IRNSS-1D	Operational
16-01-20	IGSO	IRNSS-1E	Operational
16-03-10	GEO	IRNSS-1F	Operational
16-04-28	GEO	IRNSS-1G	Operational
17-08-31	IGSO	IRNSS-1H	Launch Failed
18-04-12	IGSO	IRNSS-1L	Operational

1.1.2 Multi-GNSS combined PPP and inter-system bias

In comparison with the single system PPP, the multi-system combined solution has the potential of increasing the number of observed satellites, optimizing the spatial geometry, and enhancing both the availability and continuity of positioning (Guo et al. 2017). Owing to the development and increased precision of satellite orbit and clock products for GPS (Dow et al. 2009), GLONASS (Weiss et al. 2010), BDS (Zhao et al. 2013), Galileo (Hackel et al. 2014), and QZSS (Steigenberger et al. 2013), coupled with the initiation of the Multi-GNSS Experiment (MGEX) in 2012 (Montenbruck et al. 2013), extensive investigations have been placing emphasis on the use of multi-GNSS integrated positioning for the purpose of

accelerating PPP convergence time and processing performance. In the early stages, some investigations were carried out into the processing of combined GPS and GLONASS observations in the PPP mode, the precision and convergence time can be substantially enhanced (Cai and Gao 2013; Li and Zhang 2014; Melgard et al. 2009). The analysis and assessments of GPS/BDS and GPS/Galileo combined positioning were also carried out (He et al. 2014; Paziewski and Wielgosz 2014). Besides these combination types, coupled with the development of multi-GNSS precise products, the fusion positioning with more systems (four systems) was carried out (Li et al. 2015c). As suggested by the findings, there were observed better reliability and less convergence time in comparison with the former two-system combined PPP. Benefitting from the fast development of multi-GNSS, integrated PPP was applied into a number of scientific research areas, for instance, marine applications (Bisnath et al. 2003; Geng et al. 2010b), tropospheric retrieving (Li et al. 2015d; Li et al. 2015e), airborne mapping (Gao et al. 2005), and precise time-transfer (Defraigne et al. 2007b).

Recently, GNSS has developed at a rapid pace with the modernization of GPS and GLONASS systems, and the launch of other global navigation systems, for instance, BDS and Galileo, besides the new frequency signal transmission, multi-system and multi-frequency combined positioning is going to emerge as one of the hot research directions for GNSS in the future (Gu et al. 2015a; Montenbruck et al. 2014; Odolinski et al. 2015a). The combination of PPP with multiple navigation satellite systems has the capability to enhance the accuracy, availability, and reliability of positioning (Chen et al. 2016; Choy et al. 2017; Lou et al. 2016; Zumberge et al. 1997). Nevertheless, in the integrated PPP, the differences existing between different systems require full consideration; if a combined PPP is created without calibrating these differences, an unfortunate result is expected to take place, which is, at times, even worse as compared with the single-system PPP. Accordingly, the inter-system bias (ISB) was introduced in a bid to encompass these differences between multi-systems (Chen et al. 2016; Jiang et al. 2017; Li et al. 2015c). It primarily comprised of three parts: system time deviation, reference frame deviation, and hardware delay bias (Torre and Caporali 2015). Montenbruck

et al. (2011) shed light on the fact that the ISB was associated with the signal delay within the receiver. The ISB between GPS and other systems, for instance, GLONASS, Galileo, and BDS, was relevant to the receiver types. The biases in the receiver hardware between GPS and GLONASS in precise positioning are specific to the receiver model (Leick et al. 1998; Raby and Daly 1993). The difference in the GPS/BDS ISB between different types of receivers can be over 100 ns (Tegedor et al. 2014). The characteristic of the ISB difference between GPS and Galileo was analyzed by Paziewski and Wielgosz (2015). They investigated the stability of ISB derived from the double-difference positioning. As the findings suggested, the ISB was stable in the long term, together with being associated with the types of receivers. The short-term ISB was effectively modeled and predicted with the methodology of spectral analysis and least squares (LS) estimation (Jiang et al. 2017). The ISB of code observations manifested significant stability in terms of standard deviation and intra-day variation, suggesting that the ISB was ordinarily stable over adjacent days (Zeng et al. 2017). It requires observation that the ISB derived from relative positioning is necessarily not the same as that from PPP in the definition.

1.2 Motivation

Till today, over 100 navigation satellites are already within the view and transmitting signals. In comparison with just the GPS system decades ago, PPP has recently entered the phase of the multi-systems integration. Besides the growth of the satellite constellations, more and more issues about compatibility and interoperability between the different types of systems have appeared, for instance, the time frame difference, difference in the coordinate frames, different error correction models, and so on. If these issues cannot be efficiently solved, a number of visible satellites are expected to only be rendered “observable”, rather than being “usable”. In this manner, we require introducing an extra parameter in order to cover the differences between systems. Accordingly, all of the satellites can be processed together, with the use of the real and valid integrated positioning. Typically, this extra parameter is named

the inter-system bias (ISB). It is expected to help improve the precision and processing time in combined PPP if the ISB can be fully calibrated. An initial calibration study dealing with the GPS/BDS ISB was carried out by Nadarajah et al. (2013) for the integer ambiguity resolution. Torre and Caporali (2014) put forward an analysis on ISB in GPS/BDS/GLONASS/Galileo/QZSS systems with various receivers. Also, ISB was applied to the GPS/BDS single-frequency short-baseline RTK (Odolinski et al. 2015a; Zhao et al. 2014) as well as long-baseline relative positioning (Odolinski et al. 2015b; Wang et al. 2015). Nadarajah et al. (2014) carried out investigations on the instantaneous attitude determination with GPS/BDS data through the estimation of the ISB. In the case of multi-GNSS PPP and ZTD/PWV retrieval (Li et al. 2015a; Li et al. 2015b; Liu et al. 2017; Lu et al. 2015), the ISB also required consideration.

Nevertheless, the research works highlighted above only referred to the ISB calibration way of estimation, together with its applications, wherein no one had involvement in the calibration way of ISB modeling. In comparison with the estimation, modeling has the advantages in lowering the number of estimated parameters, which is expected to help shorten the convergence time. Even in some special cases, for instance, in valleys, cities, or forests, most likely where perhaps there are insufficient observations, the way of modeling also has the potential of avoiding the matrix rank deficiency, together with maintaining the output of results. Accordingly, in this thesis, the motivation primarily places emphasis on ISB modeling and prediction; we are putting efforts for the establishment of a model, in addition to using the predictions from this model as an a priori information, aimed at bringing benefits to the integrated PPP. Prior to the modeling, the high-precision and continuous estimated ISB series require achievement. For the achievement of this target, two different function models impacting the accuracy of the ISB estimation are investigated, and their equivalence is figured out as well. Thereafter, we investigate the impacts of stochastic models on the ISB. Eventually, the preprocessing methodology of the precise clock product for the elimination of the ISB jumps is also carefully analyzed as well. All of these three steps aimed at obtaining high

accuracy and a continuous and smooth ISB series, which constitutes the basis of modeling. This thesis can be regarded as a coherent, systematic study from the function model, the stochastic model, the removal of ISB jumps, and, eventually, to the ISB modeling.

1.3 Main contributions

The key contributions of this thesis can be summarized as hereunder:

- The equivalence of two different function models (MIS and MDS) was proved theoretically. Subsequent to that, a numerical verification was also carried out to support the theoretical proof. Accordingly, the equivalence was creatively certified not only theoretically but also numerically.
- The impacts of the four different stochastic models of ISB processing were innovatively assessed and investigated comprehensively, and their impacts on the combined PPP were analyzed as well. An optimized selection strategy on ISB stochastic models was proposed; it is associated with choosing precise products from the two main MGEX analysis centers (GFZ and WUH). With the use of *GBM* precise products from GFZ, using the ISB-RW or ISB-WN model is recommended; with regard to the *WUM* products, the ISB-PW or ISB-AD model is selected.
- The positive correlation existing between the ISB difference and the residuals of satellite clock offsets in adjacent days was revealed, suggesting that the successful detection and repair of ISB jumps primarily rely on the precise clock product preprocessing.
- The actual reason leading to the ISB jumps was determined to be the extreme points (maximum or minimum points) of the satellite clock data in the frequency domain. On the basis of this, all extreme points were classified into three types; moreover, with regard to each of the types, we applied a different preprocessing methodology. The ISB jumps can

be eliminated with the help of different preprocessing strategies enacted on the precise clock product.

- On the basis of all the above stated research works, a precise and effective ISB model was proposed. The predicted ISB derived from this model can be applied as an a priori information in the integrated PPP. Owing to the high prediction accuracy, we even fixed the predicted ISB as a known parameter in the processing. Combined PPP with an a priori ISB constraint or a fixed ISB can achieve the same precision as normal PPP with an estimated ISB, but with a faster convergence speed primarily in the Up component.

1.4 Overview of the dissertation

The seven chapters of this thesis are organized as below:

Chapter 1 introduces the background, innovation and main contribution of this work, as well as the outlines of this thesis.

Chapter 2 gives a brief introduction on the different types of GNSS observations, error sources, models of PPP, and the estimation methods in GNSS data processing.

Chapter 3 presents the equivalence proof of two different function models for ISB estimation both in theory and numerical.

Chapter 4 assesses four different stochastic models for ISB. Afterward, the suggestion that PPP users should apply the same ISB estimation strategy as that in the period of precise products generation by the ACs is proposed.

Chapter 5 proposes a new methodology on the preprocessing of precise clock products, together with utilizing this methodology to detect, eliminate, and repair the ISB jumps. Following the preprocessing, a smoothed and continuous ISB series can be attained, that is the basis of ISB modeling in chapter 6.

Chapter 6 investigates the characteristics of ISB, besides the ISB series is modeled as a form of a polynomial plus several periodic functions. PPP mode with the prediction ISB as an a priori constraint, or fixed can achieve the same accuracy as the normal PPP with ISB estimation and have a faster rate of convergence mainly in the Up component.

Eventually, chapter 7 summarizes the conclusions of the thesis and puts forward outlooks for future work.

2 Multi-GNSS data models and processing

2.1 Introduction

The basic GNSS observations primarily include code pseudorange and carrier phase measurements. The target of the GNSS data processing is the use of these observations for the achievement of the needed results, for instance, user coordinates, receiver clock, and zenith total delay. All through this procedure, aimed at getting higher and more stable results, all potential errors require removal or mitigation, more appropriate and stable precise point positioning (PPP) model including the function model and the stochastic model should be applied; in addition, a better and efficient parameter estimation methodology is deemed as essential to be chosen.

This chapter aims at introducing GNSS observations, in addition to key errors, the PPP model, and the parameter estimation methodology in the data processing. Furthermore, different GNSS observations are presented in section 2.2, and key error sources are presented in section 2.3, followed by the precise point positioning model; besides that, the parameter estimation in GNSS data processing is presented in section 2.4 and 2.5.

2.2 GNSS observations

The fundamental measurements recorded by the GNSS receiver constitute the differences in time or phase between the signals transmitted from the GNSS satellites to the reference signals that are produced inside the receiver. The receiver is capable of primarily recording two kinds of signals, which include pseudorange and carrier phase.

2.2.1 Code pseudorange

The basic GNSS observable is the traveling time ΔT of the signal for the propagation from the phase center of the satellite antenna (at the emission time) to the phase center of the receiver (at the reception time). This value, multiplied by the speed of light, indicates the apparent range $D = c \cdot \Delta T$ between them. Typically, a quartz oscillator is put to use in the receiver for the management of the timing. In general, the accuracy of quartz clocks is worse than one part in a million; this indicates that if the clock has not been corrected for a period of one week, the distance error is expected to be massive. However, in a GPS receiver, the clock time is put to use for the measurement of the ranges to different satellites at almost the same time, which indicates that all the measured ranges carry the same error. Accordingly, if the satellite orbital parameters are known, the receiver position can be calculated along with the time error.

The measurement $D = c \cdot \Delta T$ highlighted earlier is termed as the pseudorange, which is an "apparent range" between the satellite and the receiver, besides not matching its geometric distance. For the purpose of considering the possible synchronism errors between these clocks, the traveling time between transmission and reception is attained as the difference in the times measured in two different clocks or timescales, which include the satellite t^s and the receiver t_r . Accordingly, considering a reference time scale T , the pseudorange measurement for satellite s and receiver r can be expressed as hereunder:

$$P(t) = c[t_r(T_2) - t^s(T_1)] \quad (2.1)$$

where c indicates the speed of light, $t_r(T_2)$ denotes the time of signal reception, which is measured in the time scale given by the clock of the receiver r , and $t^s(T_1)$ suggests the time of signal transmission, which is measured in the time scale provided by the satellite clock s .

The pseudorange $P(t)$ measurement attained by the receiver that makes use of this procedure includes the geometric range ρ between the receiver and the satellite and clock synchronism errors, other terms due to signal propagation through the atmosphere (ionosphere and troposphere), relativistic effects, instrumental delays (of satellite and receiver), multipath, and observation noise. In a case where all of these terms are taken into consideration, the previous equation can be rewritten as follows, where $P_{r,j}^s$ represents the GNSS code measurement at a frequency j (Teunissen 1996; Xu 2002):

$$P_{r,j}^s = \rho_r^s + c(dt_r - dt^s) + k_{p,r} - k_p^s + I_{r,j}^s + T_r^s + R_r^s + S_r^s + M_r^s + \varepsilon_r^s \quad (2.2)$$

where ρ_r^s indicates the geometric distance from the receiver r to the satellite s , which includes the phase center offset and variations; dt_r and dt^s represent the receiver and satellite clock offsets from the GNSS timescale, correspondingly; $k_{p,r}$ and k_p^s are the receiver and satellite hardware delays, correspondingly that are dependent on the code and frequency; $I_{r,j}^s = a_j STEC$ is the ionospheric delay on the signal path at frequency j ; $a_j STEC$ implies a frequency-dependent ionospheric delay term, where a_j is the conversion factor between the integrated electron density along the ray path $STEC$; T_r^s denotes the tropospheric delay on the signal path; R_r^s is the impact of the relativity; S_r^s indicates the Sagnac effect, which can be corrected as the relativistic effect by means of equation (2.5); M_r^s denotes the multipath effects on the code pseudorange measurement; and ε_r^s represents the impact of observation noise and other non-modeled error sources, which are considered as white noise.

2.2.2 Carrier phase

The carrier phase observable is a measure of the range between a satellite and receiver expressed in units of cycles of the carrier frequency. This measurement can be made with quite a high precision (on the order of millimeters). From the moment a receiver locks onto a satellite to the end of the observation, the carrier phase observable can be segregated into three parts, wherein two of them do not change all through the session, and one of them is likely to vary.

$$\varphi = \alpha + \beta + N \quad (2.3)$$

The initial fractional phase is established at the first instant of the lock-on. As the receiver starts tracking the satellite, it is highly unlikely that the satellite signal is going to be attained precisely at the commencement of the wavelength phase cycle. It is expected to grab on at some fractional part of a phase, and this fractional phase is going to remain unchanged for the duration of the observation. It is termed as the initial fractional phase, in addition to being symbolized in the equation above by α .

The symbol β indicates the count of the number of full-phase cycles coming in all through the observation. Apparently, the count grows from the moment of lock-on until the end of the observation. In other words, β is the receiver's record of the consecutive variety in full-phase cycles, 1, 2, 3, and 4, between the receiver and the satellite as the satellite moves over. If the observation proceeds without the cycle slip, the observed cycle count is the only one of the three numbers, which are likely to change.

The integer cycle ambiguity N represents the number of full-phase cycles between the receiver and the satellite at the first instant of the receiver's lock-on. It can also be labeled as the carrier phase ambiguity or the cycle count at lock-on. It does not change from the moment of locking to the end of the observation unless the loss of the lock. Nevertheless, when there is a cycle slip, and by the time the receiver reacquires the signal, the normally constant integer ambiguity has changed.

If the similar errors are considered as the code pseudorange, the carrier phase equation (2.3) can be expanded as follows, where $\varphi_{r,j}^s$ represents the GNSS carrier phase measurement at a frequency j (Hofmann-Wellenhof et al. 2008; Teunissen 1996). With the movement of the satellite along its orbit, the GNSS receiver observes the cycle count. In other words, it is capable of counting the number of full wavelengths β , since its lock-on, and how much they have changed as the satellite moves from one place to another in its orbit. Accordingly, if we make use of the precise orbit product, β is going to be absorbed by it, suggesting that β is no longer existent in the carrier phase equation.

$$\begin{aligned} \lambda_j^s \varphi_{r,j}^s = & \rho_r^s + c(dt_r - dt^s) + \lambda_j^s (N_j^s + K_{L,r} - K_L^s) \\ & - I_{r,j}^s + T_r^s + R_r^s + S_r^s + m_r^s + \zeta_r^s \end{aligned} \quad (2.4)$$

where λ_j^s indicates the carrier wavelength of the satellite s at frequency j ; $K_{L,r}$ and K_L^s denote the receiver and satellite hardware delays in phase, respectively; N_j^s is the integer phase ambiguity; m_r^s denotes multipath effects in phase; ζ_r^s refers to the un-modeled effects and measurement noise for carrier phase observations.

2.3 GNSS error sources

The mechanism of GNSS navigation and positioning is expected to be impacted by a variety of errors that are divisible into three key categories: the errors associated with navigation satellite, the errors associated with the receiver and station, and the errors associated with signal propagation. Approximately, all of the error sources in GNSS processing are summarized in Table 2.1.

Table 2.1 All kinds of error sources in GNSS processing.

Categories of error	GNSS error sources	Solution strategies
Errors associated with the satellite	Satellite orbit error	Eliminate with precise orbit product
	Satellite clock error	Eliminate with precise clock product
	Satellite antenna phase center offset and variation	PCO, PCV model correction
	Relativity effect	Model correction
	Phase wind up	Model correction
Errors associated with the receiver	Receiver clock error	Parameter estimation
	Receiver antenna phase center offset and variation	PCO, PCV model correction
	Effect of earth rotation	Model correction
	Solid earth tide	Model correction
	Ocean tide loading	Model correction
Errors related to signal propagation	Tropospheric delay	Model correction and parameter estimation
	Ionospheric delay	Observation combination, or parameter estimation, or model correction
	Multipath	Extremely avoid

Owing to the fact that the pseudorange and carrier phase observations of the non-station difference or inter-satellite difference are put to use in PPP, the measurement errors are not possible to be eliminated in a differential manner. It is deemed as quite essential to consider the impact of these errors in the course of making precise processing. In accordance with Table 2.1, there are primarily two approaches to handling these errors (Hofmann-Wellenhof et al. 2008; Leick et al. 2015; Xu and Xu 2016):

The first one deals with making use of a precise theoretical error model to correct. This is considered as appropriate for those errors, which can be modeled precisely, or instance, antenna phase center offsets and variations, earth tide and ocean tide loading, and narrow sense and general relativity effects.

The second one involves the introduction of unknown parameters in the observation equation for the estimation or combination of the observations for eliminating the errors. This methodology is good for those errors that cannot be modeled precisely. For instance, a random walk model can be employed for the purpose of estimating the tropospheric delay, and the ionospheric delay can be eliminated through the combination of two-frequency observations.

2.3.1 Errors associated with the satellite

Satellite orbit and clock error

The orbit error of the GNSS satellite refers to the difference that exists between the orbit described by the satellite ephemeris and its real orbit (Montenbruck et al. 2005; Wei and Ge 1998). This difference is a reflection of the accuracy of the orbit, which is provided by the ephemeris. The navigation satellite is termed as a known reference station (orbit) in the majority of GNSS data processing; accordingly, the satellite orbit error is expected to directly impact the effects of the subsequent data processing. In addition, the impact of orbit error on positioning accuracy is different in three directions. The biggest impact emerges in the radial direction that can be absorbed by the clock product in the process of clock estimation. The impact of the error in the tangential and normal directions on positioning precision has a correlation between the orbital planes of the satellite; the maximum time can reach 50% of the error in the respective directions.

All navigation satellites carry the high-precision atomic clocks for the purpose of providing a time reference for signals. Owing to the satellite space environment, coupled with the atomic

clock aging, and other reasons, the time of the navigation satellite is still different from the true time, which is termed as the satellite clock error. In the non-differential data processing, the satellite clock error is expected to lead both the satellite position and geometric distance to deviate from the correct value, which would lower the solution accuracy. Accordingly, it is deemed as quite essential to rectify the clock error of the satellite through the use of the clock error correction.

The satellite orbit and the clock both are considered as two pivotal products in the GNSS data processing. The broadcast ephemeris is directly encoded in the navigation message of the satellite. Its orbit and clock accuracy are approximately 1 m and 5 ns, correspondingly, which are capable of just supporting the navigation level applications with a precision of several meters. Aimed at supporting the higher precision application, IGS and its subordinate analysis center (AC) both estimated the high-precision satellite orbits and clock products on the basis of the global GNSS permanent tracking stations, together with providing users by the Internet. The details of the accuracy and delay period of different IGS orbit and clock products are listed in Table 2.2. Apparently, the precision of the final products is extremely high, which caters to the requirements of the high-precision post positioning. The accuracy of the ultra-rapid orbit product (IGU) has a similar level as the final product (IGS); it has the capability to satisfy the real-time precision application. Nonetheless, the predicted part of the IGU clock only has a precision level of 1.5 ns, which is merely slightly better than the broadcast product, which is not applicable in the real-time positioning. In this manner, it is quite essential to estimate the clock product in real-time processing on the basis of the real-time data from the reference stations. With regard to the real-time precision positioning applications, for the purpose of obtaining a higher solution accuracy, IGU orbit and real-time clock products are still required for the correction of the orbit and clock error.

Table 2.2 Accuracy and delay period of different orbits and clocks products.

Type		Accuracy	Latency	Updates	Interval	
GPS	Broadcast	Orbits	~100cm	Real time	--	daily
		Sat. clocks	~5ns RMS ~2.5ns SDev			
	Ultra-Rapid (predicted half)	Orbits	~5cm	Real time	At 03, 09, 15, 21 UTC	15min
		Sat. clocks	~3ns RMS ~1.5ns SDev			
	Ultra-Rapid (observed half)	Orbits	~3cm	3-9 hours	At 03, 09, 15, 21 UTC	15min
		Sat. clocks	~150ps RMS ~50ps SDev			
	Rapid	Orbits	~2.5cm	17-41	At 17 UTC	15min
		Sat. & Stn. Clocks	~75ps RMS ~25ps SDev	hours	daily	5min
		Final	Orbits	~2.5cm	12-18	Every
	Final	Sat. & Stn. Clocks	~75ps RMS ~20ps SDev	days	Thursday	Sat.: 30s Stn.: 5min
		GLONASS Final	Orbits	~3cm	12-18 days	Every Thursday

Satellite antenna phase center offset and variation

The satellite antenna phase center deviation refers to the deviation between the quality of the satellite antenna and the phase. The precise satellite orbit product offers the coordinates of the satellite mass center; nevertheless, the GNSS observation point is the satellite antenna phase center. The difference between the satellite mass center and phase center is termed

as the satellite antenna phase center deviation, which can be normally segregated into two parts:

- (1) The deviation of antenna reference point and average antenna phase center, which is antenna phase center offset (PCO).
- (2) The deviation between the antenna instantaneous phase center and the mean phase center, which is the antenna phase center variation.

The antex files provided by IGS contain both the PCO and PCV corrections of varying frequencies of GPS and GLONASS satellites. Since GPS week 1400 (November 5, 2006), IGS has adopted a new absolute antenna phase center correction model, igs05.atx, for the replacement of the original igs_01 relative antenna phase center correction model. In addition, following GPS week 1632 (April 17, 2011), the new model igs08.atx takes the place of igs05.atx. From GPS week 1854, IGS starts providing the igs08.atx with the PCO and PCV correction for satellites of BDS, Galileo, QZSS and IRNSS systems (Montenbruck et al. 2015). The IGS recently adopted a new reference frame, termed as IGS14, on 29 January 2017 (GPS Week 1934). At the same time, an updated correction file for the satellite and ground station antenna calibrations, igs14.atx, was implemented as well (Rebischung and Schmid 2016). The switch from IGS08/igs08.atx to IGS14/igs14.atx was carried out since the GPS week 1934 (29 January 2017). In the PPP data processing, it is deemed as essential to maintain consistency with the precision products for the use of the corresponding satellite PCO and PCV corrections and strategy.

Relativistic effect

The relativistic effect deals with the state of the location of the satellite and receiver, which is the relative clock error between the satellite clock and the receiver clock due to the difference between the speed of motion and the gravitational potential. The average speed of a GPS satellite is about 3.8 km/s; in addition, both the satellite and ground users are expected to have

a nontrivial gravitational potential difference. In accordance with the relativistic effect, the GPS satellite clock runs faster as compared with the ground clock, which gives rise to a difference of approximately 0.45 ns/s. For the maintenance of the signal frequency received by the ground was consistent with the signal frequency designed for the GPS system, and the adjustment for the standard frequency of the GPS satellite clock was carried out before launching of the satellite. Nevertheless, owing to the fact that orbits of GPS satellites are not circular, and the impact of the earth's gravitational field at different locations is not the same; also, the relativistic effect on the satellite clock frequency does not have constancy. There is still a residual after the above frequency adjustment; accordingly, this part of the influence can be rectified in accordance with the following equation (Kouba and Héroux 2001):

$$\rho = -\frac{2}{c} r \cdot \dot{r} \quad (2.5)$$

where r and \dot{r} represent the position vector and the velocity vector of the satellite in the ECEF coordinate system. When the eccentricity of the satellite orbit is 0.01, the range error, as a result of the relativistic effect, has the potential to reach up to 6.864 m; that is why, with regard to PPP, the above periodic item requires mandatory consideration. Besides periodic corrections, the relativistic effect also includes gravitational delays due to the earth's gravitational field, which can be stated as hereunder:

$$\Delta D_g = \frac{2\mu}{c^2} \ln \frac{r + R + \rho}{r + R - \rho} \quad (2.6)$$

where, μ is an indication of the product of the gravitation constant G with the total mass of the earth M ; c represents the speed of light in a vacuum; r denotes the distance from the satellite to the center of the earth; R is the distance from the station to the center of the earth; and ρ is the geometric distance from the station to the satellite. When the satellite is close to the Earth's surface, the maximum value of delay is approximately 19 mm.

Effect of phase wind up

GNSS satellites adopt the right-hand circular polarization (RHCP) electromagnetic wave for the navigation signal. The satellite signal transmitting antenna, coupled with the receiver antenna will be carried in the relative rotation owing to their own motion, which causes a variation in the phase observation. This impact is termed as the antenna phase wind up effect (Wu et al. 1992). The antenna phase wind up error is associated with the relative position between the satellite transmitting antenna and the receiver antenna, which can theoretically be up to one cycle owing to the fact that, if the satellite-to-receiver distance remains fixed, meanwhile the satellite turning around 360° , the distance measured over phase is expected to vary a wavelength, that would be approximately 20 centimeters for the GPS L1 carrier phase measurement.

The phase wind up error generated by the rotation of the satellite transmitting antenna is constituted by two parts, which are integer part and decimal part. The integer part is typically rectified by the cumulative count of the epoch, and the decimal part is calculated in accordance with the equation presented as hereunder:

$$\begin{aligned} \delta\phi &= \text{sign}(\zeta) \cdot \arccos\left(\frac{D' \cdot D}{|D'| \cdot |D|}\right) \\ \zeta &= k \cdot (D' \cdot D) \\ D' &= x' + k \cdot (k \cdot x') - k \times y' \\ D &= x - k \cdot (k \cdot x) + k \times y \end{aligned} \tag{2.7}$$

where k is a representation of the unit vector of the satellite to the receiver. D' and D correspondingly denote the effective dipole vector of satellite and receiver antennas, which can be determined by the unit vector under a satellite-fixed coordinate system as well as the unit vector of the earth-fixed coordinate system.

Since the motion characteristics of the receiver antenna are quite tough to model, the phase wind up error, which is generated by the receiver antenna rotation, can be absorbed by the receiver clock error; accordingly, in general, in the GNSS precision data processing, only

the phase wind up error caused by the satellite antenna rotation is taken into account (Kouba 2002).

The correction of earth rotation

Owing to the fact that the earth-fixed coordinate system is a non-inertial coordinate system, it has the potential to vary with earth rotation, so the earth-fixed system, which corresponds to the receiving time of receiver and the satellite signal launch moment, is considered as different. That is why this effect requires mandatory consideration while calculating the geometric distance of the satellite to the receiver is calculated in the earth-fixed coordinate system.

As an assumption that the station coordinates are (x_r, y_r, z_r) , the satellite coordinates are (x^s, y^s, z^s) , ω an indication of the earth's rotation speed, and c is the speed of light, the distance correction, as a result of the earth rotation, can be indicated as (Petit et al. 2010):

$$\Delta\rho = \frac{\omega}{c} \left[(x^s - x_r) \cdot y^s - (y^s - y_r) \cdot x^s \right] \quad (2.8)$$

2.3.2 Errors associated with the receiver

Receiver clock error

The GNSS receiver clock error implies the difference existing between the clock of receiver and the GPS standard time. The receiver clock error primarily impacts the distance calculation of the satellite position as well as the station. For instance, 1 μs receiver clock error can cause the error of satellite position of 4 mm. As long as the receiver clock error correction precision is better than 1 μs , it has the capability of fulfilling the precision requirement of PPP.

In general, the receiver is installed with a quartz clock, with its quality way worse than the atomic clock. The variation of the quartz clock is large, fast, and weak stability, and a specific mathematical model is unable to model it. In this manner, in PPP, the receiver clock of each observation epoch is generally considered as white noise to estimate.

Receiver antenna phase center offset and variation

The observations of GNSS receiver are typically measured to the point of antenna phase center, while the antenna height is generally referred to the antenna reference point; these two points are not overlapped in general. This deviation is termed as the receiver antenna phase center offset (PCO), and the antenna phase center of L1 and L2 also show deviation from each other. It requires mandatory consideration in PPP. Similar to the satellite antenna, following the replacement of the IGS05 antenna model of the igs_01 model, the antenna phase center correction of the receiver is switched from the relative mode to the absolute mode, also leading to an extensive change in the correction of receiver antenna phase center in the receiver fixed coordinate system (NEU system).

The phase center of the receiver antenna is not fixed. The instantaneous phase center undergoes a change with the elevating angle, azimuth angle, and signal strength. That is why we call the difference between the instantaneous phase center and the average phase center of the receiver antenna the antenna phase center variation (PCV). In the same manner as the satellite antenna phase center variation, IGS offers PCV corrections of various receivers in the same antenna file (igs08_week.atx) that has a gradient of 5° in altitude and 5° in azimuth, which ranges from $0-90^\circ$ in altitude and $0-360^\circ$ in azimuth.

Earth Tides

The gravitational impacts of the moon, sun, and other perturbation objects are expected to result into periodic fluctuations on the surface of the earth, termed as earth tides. Its impact on the station position primarily includes a long-period term associated with the latitude and a short-period term, which comprises diurnal tide as well as semidiurnal tide. Among them, diurnal and semidiurnal items can be smoothed by an entire day of static observation data, but the long-term item is harder to eliminate. It is still expected to impact the accuracy of GNSS data processing. In the mid-latitudes, the impact of the long-period term on the earth's solid tide in the radial distance measurement has the potential to reach 12.5 cm, which results into

a positioning system error of 5 cm in the North direction (Héroux et al. 2001). The earth tide has a close association with the geographical location of the station. With regard to the relative positioning of the short baseline, owing to the robust spatial correlation, it is possible to eliminate the earth tide in accordance with the differential methodology; on the other hand, with regard to the long-baseline relative positioning or PPP, the earth tide cannot be eliminated by the difference, accordingly requiring mandatory correction by the model.

In the GNSS precise data processing, the following approximate equation can be put to use for the correction of the earth tide (Petit et al. 2010):

$$\Delta r = \sum_{j=2}^3 \frac{GM_j}{GM} \frac{r^4}{R_j^3} \{ [3l_2(\hat{R}_j \cdot \hat{r})]\hat{R}_j, [3(\frac{h_2}{2} - l_2)(\hat{R}_j \cdot \hat{r})^2 - \frac{h_2}{2}]\hat{r} \} + [-0.025 \sin \phi \cos \phi \sin(\theta_g + \lambda)] \cdot \hat{r} \quad (2.9)$$

where Δr indicates the station coordinate displacement caused by earth tide; GM represents the gravitational coefficient of the earth; GM_j is an indication of the gravitational constants of the Moon ($j=2$) and the Sun ($j=3$); r and R_j are the geocentric state vectors of the station, the Moon and the Sun with the corresponding unit vectors \hat{r} and \hat{R}_j , correspondingly; l_2 and h_2 correspondingly indicate the nominal second degree Love and Shida dimensionless numbers (about 0.608, 0.085); ϕ and λ imply the site latitude and longitude, correspondingly and θ_g is Greenwich Mean Sidereal Time (Kouba and Héroux 2001).

Ocean tide loading

Ocean tide loading is termed as the periodic fluctuation of the crustal surface, which is a result of ocean tides, and the impact is an order of magnitude below the earth tide. With regard to the dynamic positioning of centimeter-level precision, and for the stations, having the observation time is less than 24 hours, besides being situated in the coastal area, the effect

of ocean tide loading requires correction. The station displacement caused by the ocean tide loading is divided by tidal waves. The tidal wave chart and green function are employed for the purpose of calculating the amplitude of the tidal wave radial, south-east and north-south direction and the phase lag relative to the Greenwich meridian (H eroux et al. 2001). The final correction is the superposition of each tidal wave. Accordingly, the ocean tide correction model is (Petit et al. 2010):

$$\Delta R_{ocean} = \sum_{i=1}^N \begin{bmatrix} A_i^r \cos(\omega_i t + \phi_i - \delta_i^r) \\ A_i^{EW} \cos(\omega_i t + \phi_i - \delta_i^{EW}) \\ A_i^{NS} \cos(\omega_i t + \phi_i - \delta_i^{NS}) \end{bmatrix} \quad (2.10)$$

where t is the epoch time; ω_i and ϕ_i correspondingly represent the frequency of each tidal wave and the astronomical angle of the epoch; N denotes the number of tidal waves, which normally is 11; it can be converted into the terrestrial reference system as well:

$$\Delta R = R_z(-\lambda)R_y(\varphi)\Delta R_{ocean} \quad (2.11)$$

2.3.3 Errors related to signal propagation

Tropospheric Effects

When the navigation signal passes through the neutral atmosphere below 50 km from the ground, the signal refracts owing to the inhomogeneity of the atmosphere, which is going to give rise to a delay in the code, coupled with an advance in the carrier phase, termed as the tropospheric delay. The tropospheric delay of the GNSS observation in the zenith direction is approximately 2.3 m, while the delay of the observation under 10-degree elevation angle has the capability to reach 20 m.

In atmospheric science, the troposphere is generally segregated into two parts, which include the hydrostatic (i.e., dry) part and the wet part. The hydrostatic component caused by the dry atmosphere and takes up about 90% of the total tropospheric delay. The hydrostatic component can be modeled conveniently (Abdel-Salam 2005; Sch uler 2001). The wet

component is primarily caused by the water vapor in the lower level of the troposphere. The wet component results into 10% of the total tropospheric delay (Abdel-Salam 2005; Xu and Xu 2016). Owing to the fast-paced variation of the water vapor, the wet component of tropospheric delay is quite difficult to model.

In PPP, the tropospheric delay in the slant path of the different satellite is transferred to the zenith direction in accordance with the mapping function. The mapping function has key association with the elevation angle. As indicated by the above paragraph, the zenith total delay (ZTD) can be segregated into the hydrostatic delay component (about 90%) caused by dry gas in the atmosphere and the wet delay component (about 10%), which is caused by water vapor. Accordingly, the slant total delay (STD) correction can be expressed as hereunder:

$$STD = M_h ZHD + M_w ZWD \quad (2.12)$$

where ZHD and ZWD indicate the zenith tropospheric dry/wet component delays; M_h and M_w correspondingly denote the dry/wet component mapping function. The dry component delay is usually corrected by the model, while the wet component delay is typically estimated as an unknown parameter. The commonly employed tropospheric correction model on the basis of the meteorological data is the Saastamoinen model (Saastamoinen 1972), the Hopfield model (Hopfield 1969); on the other hand, primarily applied mapping functions include Niell mapping function(NMF) (Niell 1996), in addition to Isobaric mapping function(Niell 2001), the Vienna mapping function(VMF) (Böhm and Schuh 2004), Global Mapping Function(GMF) (Böhm et al. 2006), and so on.

Ionospheric Effects

The ionosphere is the atmospheric area of the earth's surface between 50 km and 1000 km. Electromagnetic waves are impacted by free electrons in the ionosphere while passing through the ionosphere; accordingly, its speed and direction of transmission are expected to

change, termed as the ionospheric delay. The magnitude of the delay is primarily associated with the electron density, and signal frequency; moreover, the impact of this delay on the zenith direction in GNSS processing has the potential to reach up to 10 meters, which can exceed 50 meters at an elevation angle of 5 degrees (Xu and Xu 2016). That is why the ionospheric delay constitutes the most important error source in the GNSS data processing and mandatory requires careful consideration.

For the purpose of eliminating or weakening the impact of the ionospheric delay, the single-frequency users typically adopt the ionospheric model, for instance, the Klobuchar model (Klobuchar 1987) and the ionospheric grid model. Dual-frequency users can make use of the dispersion effect of the ionosphere for the elimination of the first order of ionospheric delay by forming a linear combination of observations. Subsequent to the elimination of the first-order impact of the ionosphere, the residual high-order impact is quite small, which can be ignored or corrected with the help of the model (Marques et al. 2011). Besides that, in the PPP model, which is based on the original observations, the slant path ionospheric delay can be estimated as a parameter (Liu et al. 2017; Zhou et al. 2017).

Multipath effect

The multipath effect refers to the interference between the reflected satellite signals received by a receiver antenna and direct satellite signals, causing the observations to deviate from the real ones, coupled with the decline in the signal strength. A serious multipath effect is likely to lead to the loss of the satellite signal. In theory, the maximum value of the multipath error is about half of the approximate code length. With regard to pseudorange, the maximum error can be up to 15 m. On the other hand, with regard to the carrier phase, the impact of the multipath error is not more than the one-quarter of the wavelength (Xu and Xu 2016).

Currently, there is no effective solution for dealing with the multipath effect, but, in general, the following methodologies can be adopted for weakening the effect: the selection of an open site in the course of measurement, with the use of an antenna with an indentation plate or a

choke ring; the extension of observation time; and parametric modeling and estimation, and so on. When the elevation angle of the satellite is low, it is more likely to have a heavier multipath error. Aimed at lowering the impact in the data processing, the methodologies having a larger cut-off elevation and a longer time smoothed observation data can be used. Conversely, the accuracy of phase observation is much higher than that of pseudorange, and the impact of the multipath effect is substantially smaller. Accordingly, in the data processing, the weight of the phase observation can be augmented. In the meantime, the weight of the pseudorange observation should be decreased, which is expected to fully reflect the advantage of the phase observation for lowering the multipath effect.

2.4 Models of precise point positioning

The premise of getting an optimal solution in the GNSS precise point positioning deals with the establishment of the correct and rational function model and stochastic model. The function model describes the function relation between the observations and estimated parameters, and the stochastic model is in the form of the statistics reflecting the relationship between all of the observations.

2.4.1 PPP function model

In GNSS PPP, the observations of pseudorange and carrier phase are typically put to use. Furthermore, their observation equations are listed above in the Equation (2.2) and Equation (2.4) presented above. There are different handling strategies for the ionospheric delay error in non-differential precision data processing; nevertheless, usually, the two methodologies of non-ionosphere observations combination and parameter estimation are applied. That is why, in accordance with different combination (or un-combination) modes, two PPP models can be developed: ionosphere-free combination model (IFCM) and un-combined model on the basis of raw observations (UCM). In this study, our PPP program is developed with the use of the IFCM, so the function models of PPP in the following parts are all making use of the IFCM.

Ionosphere-free combination model

The IFCM is termed as the most frequently employ function model in PPP. Through the formation of the non-ionospheric combined observations, the first-order ionosphere delay in the pseudorange and carrier phase measurement is eliminated. On the basis of Equation (2.2) and Equation (2.4), the observation equation of the combined observations can be developed as (Kouba and Héroux 2001; Zumberge et al. 1997):

$$\begin{aligned}
 P_{r,IF}^s &= \rho_r^s + c(dt_r - dt^s) + k_{IF,r} - k_{IF}^s + T_r^s + \varepsilon_{IF,r}^s \\
 \lambda_{IF}^s \phi_{r,IF}^s &= \rho_r^s + c(dt_r - dt^s) \\
 &+ \lambda_{IF}^s (N_{IF}^s + K_{IF,r} - K_{IF}^s) + T_r^s + \zeta_{IF,r}^s
 \end{aligned} \tag{2.13}$$

where:

$$\begin{aligned}
 k_{IF,r} &= (f_1^2 k_{1,r} - f_2^2 k_{2,r}) / (f_1^2 - f_2^2) \\
 k_{IF}^s &= (f_1^2 k_1^s - f_2^2 k_2^s) / (f_1^2 - f_2^2) \\
 N_{IF}^s &= c(f_1 N_1^s - f_2 N_2^s) / (f_1^2 - f_2^2) / \lambda_{IF}^s \\
 K_{IF,r} &= c(f_1 K_{1,r} - f_2 K_{2,r}) / (f_1^2 - f_2^2) / \lambda_{IF}^s \\
 K_{IF}^s &= c(f_1 K_1^s - f_2 K_2^s) / (f_1^2 - f_2^2) / \lambda_{IF}^s
 \end{aligned} \tag{2.14}$$

Other errors in observation equations, for instance, PCO and PCV, phase wind up, relativistic effect, earth rotation correction, earth tide, and ocean tide loading, can be eliminated with the applications of the precise models. In this way, these errors are going to appear in the observation equations no more (similarly hereinafter).

This model eliminates the impacts of the first order ionospheric delay by the two-frequency linear combination. The tropospheric delay is segregated into two parts, which include dry component and wet component; in addition, the Saastamoinen model is employed for the correction of the dry component delay (Saastamoinen 1972), and the zenith wet component delay is termed as an additional parameter for the purpose of estimation. The GMF mapping function is employed for projecting the zenith troposphere to the slant path (Böhm et al. 2006). The single system receiver clock error is typically estimated each epoch, while in

the combined PPP, one approach involves estimating one receiver clock error in each system individually; the other one still involves estimating the receiver clock error of the reference system each epoch, in addition to an extra ISB for the rest system. These two different function models for the ISB estimation are going to be comprehensively discussed in chapter 3. In the floating PPP, the hardware delay is absorbed by the ambiguity parameter, so the ambiguity is estimated as a float. With regard to the ambiguity fixed PPP, the ionosphere-free combined ambiguity is typically decomposed into wide-lane and narrow-lane ambiguities and try to fix in order.

Un-combined model based on raw observations

The ionosphere-free combination eliminates the impact of the first-order ionospheric term, meanwhile also bringing some deficiencies, for instance, the observation noise being magnified 3 times, besides halving the number of observations. In the meantime, the ionosphere-free combination is equivalent to treating the ionospheric delay as a time-varying parameter, meanwhile disregarding the contribution of the stability of the ionosphere delay to the PPP in a short time (Zhang et al. 2011). Furthermore, with the increase in the multi-frequency data, the traditional ionosphere-free combination model is more and more difficult for the application in the unified processing of multi-frequency data. For the purpose of avoiding these adverse impacts, in recent years, a number of scholars have started investigating the UCM (Gu et al. 2015b; Lou et al. 2016; Odijk et al. 2016; Shi et al. 2012a; Zhang et al. 2012). The observation equations of UCM are directly established on the raw observations, so any frequency observation equation of each GNSS system can be established in accordance with this model, which is a unified data processing model.

In Equation (2.2) and Equation (2.4), there is observed a strong correlation between system bias, pseudorange and phase hardware delays, ionospheric delay, and ambiguity parameters. Normal equations are not possible to be directly solved owing to the rank deficiency. That is how it is deemed as quite essential to introduce additional reference or

constraints for the separation of each parameter. Nonetheless, in the actual data processing, the pseudorange hardware delay is unlikely to be an interesting parameter to the user. Accordingly, we are able to make use of the receiver clock, ionosphere delay, and ambiguity for the absorbance of some pseudorange hardware delays; subsequent to that, other required parameters, for instance, slant path ionospheric delay, can be attained.

2.4.2 Stochastic model of PPP

The stochastic model between observations and parameters constitutes another basis for the GNSS data processing. The least squares adjustment requires determining the weights between each of the observations on the basis of the variance of the observations, and the state prediction in real-time filtering is mandatorily required to be based on the stochastic characteristics of the parameters. The stochastic model commonly put to use in PPP is based on satellite elevation or signal-to-noise ratio (SNR).

Stochastic model based on satellite elevation

Stochastic model, which is based on satellite elevation is a function between measurement noise σ and satellite elevation E .

$$\sigma^2 = f(E) \tag{2.15}$$

Different stochastic model has different forms of elevation function, two of the most widely used are the exponential function model and the sine-cosine function model. For example, the exponential function model proposed by Barnes (2000):

$$\sigma^2 = \sigma_0^2 (1 + ae^{-E/E_0})^2 \tag{2.16}$$

where σ_0 is a representation of the standard deviation of the observation in the near zenith direction; E_0 indicates the reference elevation (degree); and, a is amplification factor. Together with that, renowned geodetic data processing software Bernese adopts the Cosine function model (Dach and Walser 2015):

$$\sigma^2 = a^2 + b^2 \cos^2 E \quad (2.17)$$

and sine function model is applied in GAMIT (Herring et al. 2010):

$$\sigma^2 = a^2 + b^2 / \sin^2 E \quad (2.18)$$

Stochastic model based on SNR

SNR is associated with the residual of atmospheric delay error, multipath effect, antenna gain, and receiver internal circuit. It has the capability to partly reflect the data quality of the observations, besides being possible to be utilized for the measurement of the noise level of the observations. Brunner et al. (1999) made use of SNR information to establish a stochastic model of carrier phase observations (SIGMA- Δ model):

$$\sigma^2 = C_i \cdot 10^{-\frac{S}{10}} = B_i \left(\frac{\lambda_i}{2\pi} \right)^2 \cdot 10^{-\frac{S}{10}} \quad (2.19)$$

where S indicates measured SNR; B_i is the phase tracking loop bandwidth(HZ); λ_i denotes the wavelength of carrier phase; and normally $C_1 = 0.00224m^2HZ$, $C_2 = 0.00077m^2HZ$.

2.5 Parameter estimation

The theoretical basis of the GNSS data processing is the Gaussian least squares. Kalman filter introduces the state equations of parameters on the basis of the least squares that are considered to be suitable for real-time data processing.

2.5.1 Least squares

The principle of least squares (LS) applies to linear systems (or equations). Moreover, the GNSS observation equations are generally nonlinear, and LS can be utilized only after linearization. The linearized equation can be written as (Bierman 2006; Ghilani 2017; Koch 2013):

$$L = AX + e \quad (2.20)$$

where, assuming the number of observations is n , m indicates the number of unknown parameters; L is the observation vector of dimension $n \times 1$; A denotes the design matrix with dimension $n \times m$; X represents the unknown parameter vector of dimension $m \times 1$; e is the measurement error with zero mean and covariance matrix Σ , with $\Sigma = \sigma_0^2 P^{-1}$, where σ_0^2 suggests the variance of unit weight and P refers to the weight matrix of the observations.

The error equation at epoch i can be derived from Equation (2.20),

$$V_i = A_i \hat{X}_i - L_i \quad (2.21)$$

where V_i is the residual vector; \hat{X}_i denotes the estimations of the unknown parameters (least square solution).

In accordance with the least squares principle, the least-squares solution mandatorily require satisfying the condition that the sum of squares of the residual error is minimum (Koch 2013; Mikhail and Ackermann 1976),

$$V_i^T P_i V_i = \min \quad (2.22)$$

Accordingly, in accordance with this criterion, the solution of Equation (2.21) is:

$$\begin{aligned} \hat{X}_i &= (A_i^T P_i A_i)^{-1} A_i^T P_i L_i \\ Q_{\hat{X}_i} &= (A_i^T P_i A_i)^{-1} \end{aligned} \quad (2.23)$$

where $Q_{\hat{X}_i}$ indicates the cofactor matrix. In addition, the covariance matrix can be written as:

$$\Sigma_{\hat{X}_i} = \hat{\sigma}_0^2 Q_{\hat{X}_i} \quad (2.24)$$

with the posteriori variance of the unit weight $\hat{\sigma}_0^2$ that can be calculated as hereunder:

$$\hat{\sigma}_0^2 = \frac{V_i^T P_i V_i}{n - m} \quad (2.25)$$

2.5.2 Kalman filter

Kalman filter is a kind of the minimum variance estimation methodology in the optimal estimation theory (Kalman 1960). It makes use of a recursive algorithm for the purpose of updating the state parameters from the a priori information of the parameters (which include the estimations, together with its variance-covariance) and the new measurement data. With Kalman filter, only the state parameter of the previous epoch and its variance-covariance information are required to be stored, and it is not considered as essential to store all the historical observation information simultaneously, which is expected to have a higher calculation efficiency.

Kalman filtering is based on a set of observation sequences $L_i, i = 1, 2, 3, \dots, n$ and system dynamics model for the solution of the estimation of the state vector. The standard Kalman filter comprises state equation as well as observation equation. The state equation is a model that describes the state dynamic variation rule, besides providing the association of state transition and change at the adjacent epochs. The observation equation describes the mathematical relationship that exists between the observation vector and the state vector. The observation vectors usually contain observation noise; in addition, only a part of state variables can be observed typically.

The state equation and observation equation of GNSS positioning, which make use of Kalman filter, are typically stated as follows (Koch and Yang 1998; Schwarz 1989; Xu and Xu 2016; Yang 2010a):

$$\begin{aligned} X_i &= \Phi_{i,i-1} X_{i-1} + w_i \\ L_i &= A_i X_i + v_i \end{aligned} \quad (2.26)$$

where, X_i and X_{i-1} are the corresponding indications of the state vectors at epoch i and $i-1$; $\Phi_{i,i-1}$ denotes transition matrix from state X_{i-1} to X_i ; w_i denotes the system noise

vector; L_i is the observation vector at epoch i ; A_i implies the coefficient matrix of observation equation; and v_i refers to observation noise. The Kalman filter makes an assumption that each observation is independent, whereas the system noise and the observation noise are not associated with each other, which is termed as the zero-mean Gaussian white noise. Accordingly, the corresponding stochastic model can be stated as hereunder:

$$\begin{aligned}
E(w_i) &= 0, Cov\{w_i, w_j\} = E[w_i w_j^T] = Q_i \delta_{ij} \\
E(v_i) &= 0, Cov\{v_i, v_j\} = E[v_i v_j^T] = R_i \delta_{ij} \\
Cov\{w_i, v_j\} &= E[w_i v_j^T] = 0 \\
\delta_{ij} &= \begin{cases} 1, (i = j) \\ 0, (i \neq j) \end{cases}
\end{aligned} \tag{2.27}$$

where, Q_i and R_i indicate the variance matrix of system noise sequence (symmetric non-negative definite matrix) and variance matrix of observation noise (Symmetric positive definite matrix), respectively; δ_{ij} is Kronecker function.

The state parameters, which normally require estimation in PPP, are receiver position, receiver clock error, ZWD, and the ionosphere-free combined ambiguities of the observed GNSS satellites. Suppose the initial state value is $X_0 = \hat{X}_0$, the variance is Σ_{X_0} , so the state estimation \hat{X}_i at epoch i can be attained recursively by Kalman filter:

(1) One-step state prediction

$$X_{i,i-1} = \Phi_{i,i-1} \hat{X}_{i-1} \tag{2.28}$$

(2) One-step prediction of covariance

$$\Sigma_{X_{i,i-1}} = \Phi_{i,i-1} \Sigma_{X_{i-1}} \Phi_{i,i-1}^T + Q_i \tag{2.29}$$

(3) Filtering gain

$$K_i = \Sigma_{X_{i,i-1}} A_i^T (A_i \Sigma_{X_{i,i-1}} A_i^T + R_i)^{-1} \quad (2.30)$$

(4) Status update

$$\hat{X}_i = X_{i,i-1} + K_i (L_i - A_i X_{i,i-1}) \quad (2.31)$$

(5) State covariance update

$$\Sigma_{X_i} = (I - K_i A_i) \Sigma_{X_{i,i-1}} \quad (2.32)$$

where, $X_{i,i-1}$ and $\Sigma_{X_{i,i-1}}$ indicate one-step prediction value and its variance-covariance matrix, respectively; besides that, K_i indicates gain matrix; \hat{X}_i and Σ_{X_i} represent filtering estimation and its variance-covariance matrix, respectively; and, I denotes unit matrix.

As evident from the above recursion formulas that Kalman filtering is a mechanism of constantly predicting and updating, through the integration of the current observation information as well as the past system information for the determination of the optimal filter estimations.

3 Two different function models for ISB estimation and equivalence proof

3.1 Introduction

The strict function model of multi-GNSS fusion PPP requires considering the differences between each satellite system, and usually, two different models can be used. One is to regard the GPS, BDS, and Galileo as an individual system, estimating the receiver clock error separately, which is termed as Model of Independent System (MIS). The other is to combine all systems observations, estimating only one common receiver clock error, and an extra parameter inter system bias (ISB) between GPS and Galileo, or BDS, which is called Model of Dependent System (MDS), which currently is widely applied in many studies (Chen et al. 2016; Jiang et al. 2017; Li et al. 2015c). Nevertheless, Thus far, the comparison and assessment of the difference between these two models have not yet been carried out comprehensively. Herein, we will investigate the equivalence of these two models, and evaluate the positioning accuracy and convergence time. Then the results show these two models are not only equivalent in theory, but also real numerical verification.

This chapter begins with the introduction of the ISB function models of the independent system and dependent system, besides the equivalence between the two models is proved based on the theoretical derivation in Section 3.2. Afterward, Section 3.3 presents the discussion of these two function models and the results of the numerical comparison. Eventually, the summary and conclusions of this study are made in Section 3.4.

3.2 Methodology and equivalence proof

Here the principles of Function Model of Independent System, and Function Model of Dependent System will be demonstrated, respectively. Besides, the theoretical equivalence will be proved and shown at the end of this part.

3.2.1 Function model of independent system

Normally, the main differences between two satellite systems, such as GPS and BDS, have a relation with the satellite constellation, the signals broadcast, and time and coordinate frame convention (Gioia and Borio 2016). The differences between the two systems can be regarded as ISB, and the most significant component correlates with the time reference difference. As for the combined PPP, we can estimate two separate receiver clocks for each system, and the ISB is considered as the increment value derived from the combination pair of GPS and another system, which here is termed as MIS. The ionosphere-free (IF) pseudorange and phase observation functions between a receiver and a GPS satellite G can be written as:

$$\begin{aligned} P^G &= \rho^G + c \cdot (dt_G - dt^G) + m^G \cdot ZTD + (b_G - b^G) + \zeta^G \\ L^G &= \rho^G + c \cdot (dt_G - dt^G) + m^G \cdot ZTD + N^G + (B_G - B^G) + \varepsilon^G \end{aligned} \quad (3.1)$$

where P^G , L^G denote pseudorange and carrier phase IF observations, respectively; ρ^G is the range between the receiver and the GPS satellite; c represents the light speed; dt_G is the receiver clock error and dt^G is the GPS satellite clock error; m^G and ZTD demonstrate mapping function and zenith tropospheric delay; the first order of ionospheric delay error is eliminated by ionosphere-free combination; b_G , b^G and B_G , B^G are the IF combined pseudorange and carrier phase hardware delay bias for receivers and satellites, respectively; N^G indicates ambiguity in meters; ζ^G and ε^G are all other errors including measurement noise.

For the GPS observations, the pseudorange hardware delay biases b_G , b^G are absorbed by the clock errors $c \cdot (dt_G - dt^G)$ in accordance with the IGS analysis convention. The carrier

phase hardware delay biases B_G , b_G are not existent in most GPS data processing anymore, because the carrier phase hardware delay biases are satellite dependent and stable over time. Hence it can be combined into ambiguity (Dach et al. 2010; Geng et al. 2010a). After applying the precise satellite orbit and clock products, Equation (3.1) can be rewritten as hereunder:

$$\begin{aligned} P^G &= \rho^G + c \cdot d\tilde{t}_G + m^G \cdot ZTD + \zeta^G \\ L^G &= \rho^G + c \cdot d\tilde{t}_G + m^G \cdot ZTD + \tilde{N}^G + \varepsilon^G \end{aligned} \quad (3.2)$$

where $d\tilde{t}_G$ and \tilde{N}^G denote the redefined receiver clock error and ambiguity:

$$\begin{aligned} c \cdot d\tilde{t}_G &= c \cdot dt_G + b_G \\ \tilde{N}^G &= N^G + B_G - b_G \end{aligned} \quad (3.3)$$

The satellite hardware delays are assimilated by the precise satellite clock and can be made a removal at the user side when applying the precise products in equation (3.2) (Defraigne and Bruyninx 2007). As evident from the equation (3.3), the ambiguity term does not remain in an integer property anymore, since it contains the bias term. The term $B_G - b_G$ is called the un-calibrated phase delay (Ge et al. 2008). Similarly, equations (3.2) and (3.3) can be applied to other GNSS systems like Galileo and BDS, which transmit Code Division Multiple Access (CDMA) signals.

In the notation of the receiver clock error, satellite clock error and some other parameters, we use the superscript "G" as the GPS system, to distinguish them from the parameters in other systems, the superscript "O" is applied here. Accordingly, similar to the GPS, the IF pseudorange and phase observation functions for the other satellite system (Galileo or BDS) can be expressed as hereunder:

$$\begin{aligned} P^O &= \rho^O + c \cdot d\tilde{t}_O + m^O \cdot ZTD + \zeta^O \\ L^O &= \rho^O + c \cdot d\tilde{t}_O + m^O \cdot ZTD + \tilde{N}^O + \varepsilon^O \end{aligned} \quad (3.4)$$

where $d\tilde{t}_O$ and \tilde{N}^O represent the reformed receiver clock error and ambiguity in the other systems, and can be shown as:

$$\begin{aligned} c \cdot d\tilde{t}_O &= c \cdot dt_O + b_O \\ \tilde{N}^O &= N^O + B_O - b_O \end{aligned} \quad (3.5)$$

Same as the GPS equation (3.2), the pseudorange hardware delay is absorbed by the receiver clock parameter, besides the difference between pseudorange and phase hardware delay is assimilated by the ambiguity parameter.

The ionosphere-free (IF) pseudorange and phase observations for the combined PPP can be formed as hereunder:

$$\begin{aligned} P^G &= \rho^G + c \cdot d\tilde{t}_G + m^G \cdot ZTD + \zeta^G \\ L^G &= \rho^G + c \cdot d\tilde{t}_G + m^G \cdot ZTD + \tilde{N}^G + \varepsilon^G \\ P^O &= \rho^O + c \cdot d\tilde{t}_O + m^O \cdot ZTD + \zeta^O \\ L^O &= \rho^O + c \cdot d\tilde{t}_O + m^O \cdot ZTD + \tilde{N}^O + \varepsilon^O \end{aligned} \quad (3.6)$$

and the corresponding estimated parameters are listed as follows,

$$X = [\Delta r, c \cdot \Delta d\tilde{t}_G, c \cdot \Delta d\tilde{t}_O, ZTD, \tilde{N}^G, \tilde{N}^O]^T \quad (3.7)$$

where Δr denotes the vector of the receiver position increment, $c \cdot \Delta d\tilde{t}_G$ and $c \cdot \Delta d\tilde{t}_O$ are the receiver clock error in GPS and another system. From (3.6) and (3.7), we can see that the receiver clock of GPS $c \cdot d\tilde{t}_G$ and other system $c \cdot d\tilde{t}_O$ are estimated as two separate parameters.

3.2.2 Function model of dependent system

Different from the MIS with estimating two individual receiver clock error parameters, MDS uses the parameterization strategy with the estimation of a common receiver clock error parameter and an extra ISB between two systems. To maintain consistency of comparison, the receiver clock and ISB in both models are estimated epoch by epoch. In comparison with

the single system or MIS PPP, the critical point in MDS PPP is the processing of ISB. Typically, station-dependent inter system bias mainly includes three components, one is the difference between time system (GPS time and BDS time, or Galileo time), together with one is from the difference of coordinate system, and the other comes from the receiver instrument hardware delay between tracking channels for different systems. For most geodetic receivers and antennas, the instrument hardware delay is not calibrated; however, for the single system or MIS PPP, it can be assimilated by the receiver clock (Chen et al. 2016). Nevertheless, since the difference of the hardware delay cannot be entirely absorbed by receiver clock and varies with the types of receivers, the ISB in MDS PPP shows in the characteristic of station-dependent. Usually, the deviation of coordination frames between two satellite systems is small (can be neglected). In this manner, the extra ISB is mainly the description of the combined increment of time system and hardware delay difference between the two systems. Transferred from the equation (3.6) of MIS, we attain the equation of MDS as hereunder:

$$\begin{aligned}
P^G &= \rho^G + c \cdot d\tilde{t}_G + m^G \cdot ZTD + \zeta^G \\
L^G &= \rho^G + c \cdot d\tilde{t}_G + m^G \cdot ZTD + \tilde{N}^G + \varepsilon^G \\
P^O &= \rho^O + c \cdot d\tilde{t}_G + ISB + m^O \cdot ZTD + \zeta^O \\
L^O &= \rho^O + c \cdot d\tilde{t}_G + ISB + m^O \cdot ZTD + \tilde{N}^O + \varepsilon^O
\end{aligned} \tag{3.8}$$

As compared with MIS, one of the estimated parameters in MDS switches from $c \cdot d\tilde{t}_O$ to ISB ,

$$X = [\Delta r, c \cdot \Delta d\tilde{t}_G, ISB, ZTD, \tilde{N}^G, \tilde{N}^O]^T \tag{3.9}$$

As evident from equation (3.8) and equation (3.9), the receiver clock of GPS $c \cdot d\tilde{t}_G$ can be estimated using both two systems observations and the extra ISB is only estimated based on the observations of the other system, there is no $c \cdot d\tilde{t}_O$ anymore.

3.2.3 Equivalence of two models

There are shared unknown parameters in the two models above, like coordinates Δr , receiver clock error of the GPS system $c \cdot \Delta \tilde{t}_G$, zenith total delay of the troposphere ZTD , and ambiguities of GPS \tilde{N}^G and ambiguities of the other system \tilde{N}^O . Nevertheless, each model has its respective parameters need to be estimated, for instance, the clock error in the other system $c \cdot \Delta \tilde{t}_O$, and inter-system bias ISB . After linearization, the conventional model can be rewritten as hereunder:

$$V = AX + BY - L, \quad P \quad (3.10)$$

where V is the vector of observation residuals; Y contains the respective parameters, such as the receiver clock error of GPS system, and clock error of the other system or ISB; X denotes the unknown station coordinate and the other remaining common parameters. L represents the observation vector; P is the weight matrix of the observations; A indicates the design matrix containing the receiver-satellite unit direction vectors and coefficients of other elements in X , which is same in two models, and will be used as notation briefly without showing each element in details. B suggests the design matrix of Y with elements of zero and one, which is different in two models, and will be discussed comprehensively as follows.

In MIS, the design matrix B and Y vector with the subscript 1 are:

$$B_1 = \begin{bmatrix} B_m & 0 \\ 0 & B_n \end{bmatrix} \quad (3.11)$$

$$Y_1 = \begin{bmatrix} (c \cdot \tilde{t}_G)_m & 0 \\ 0 & (c \cdot \tilde{t}_O)_n \end{bmatrix}$$

where m and n denote the number of observations in GPS and the other system, respectively; B_m and B_n are block matrixes filled with 1 in the number of m and n , both of them can be shown as hereunder:

$$B_m = [1 \quad 1 \quad \dots \quad 1]_m \quad (3.12)$$

$$B_n = [1 \quad 1 \quad \dots \quad 1]_n$$

$(c \cdot \tilde{d}t_G)_m$, and $(c \cdot \tilde{d}t_O)_n$ are also partitioned matrixes filled with the receiver clocks $c \cdot \tilde{d}t_G$, and $c \cdot \tilde{d}t_O$ with the dimension of m and n , which can be written as:

$$\begin{aligned} (c \cdot \tilde{d}t_G)_m &= [c \cdot \tilde{d}t_G \ c \cdot \tilde{d}t_G \ \dots \ c \cdot \tilde{d}t_G]_m^T \\ (c \cdot \tilde{d}t_O)_n &= [c \cdot \tilde{d}t_O \ c \cdot \tilde{d}t_O \ \dots \ c \cdot \tilde{d}t_O]_n^T \end{aligned} \quad (3.13)$$

Meanwhile, in MDS, the design matrix B and Y vectors with the subscript of 2 can be stated as:

$$\begin{aligned} B_2 &= \begin{bmatrix} B_m & 0 \\ B_n & B_n \end{bmatrix} \\ Y_2 &= \begin{bmatrix} (c \cdot \tilde{d}t_G)_m & (c \cdot \tilde{d}t_G)_n \\ 0 & (ISB)_n \end{bmatrix} \end{aligned} \quad (3.14)$$

where $(ISB)_n$ can be indicated as follows:

$$(ISB)_n = [ISB \ ISB \ \dots \ ISB]_n^T \quad (3.15)$$

As mentioned above, the ISB is mainly caused by the differences of time frame, coordinate frame, hardware delays between different satellite systems. Herein, we assume the ISB in the form of receiver clock error increment between two systems. Hence, the equation can be represented as:

$$ISB \approx c \cdot \tilde{d}t_O - c \cdot \tilde{d}t_G \quad (3.16)$$

Substituted equation (3.16) into the equation (3.14), the new matrix can be rewritten as:

$$\begin{aligned} B_2 &= \begin{bmatrix} B_m & 0 \\ B_n & B_n \end{bmatrix} \\ Y_2 &= \begin{bmatrix} (c \cdot \tilde{d}t_G)_m & (c \cdot \tilde{d}t_G)_n \\ 0 & (c \cdot \tilde{d}t_O - c \cdot \tilde{d}t_G)_n \end{bmatrix} \end{aligned} \quad (3.17)$$

Compared the dot product of the equation (3.11) with the equation (3.17),

$$\begin{aligned}
B_2 Y_2 &= \begin{bmatrix} B_m & 0 \\ B_n & B_n \end{bmatrix} \begin{bmatrix} (c \cdot d\tilde{t}_G)_m & (c \cdot d\tilde{t}_G)_n \\ 0 & (c \cdot d\tilde{t}_O - c \cdot d\tilde{t}_G)_n \end{bmatrix} \\
&= B_m (c \cdot d\tilde{t}_G)_m + B_n (c \cdot d\tilde{t}_G)_n + B_n (c \cdot d\tilde{t}_O - c \cdot d\tilde{t}_G)_n \\
&= B_m (c \cdot d\tilde{t}_G)_m + B_n (c \cdot d\tilde{t}_G)_n + B_n (c \cdot d\tilde{t}_O)_n - B_n (c \cdot d\tilde{t}_G)_n \\
&= B_m (c \cdot d\tilde{t}_G)_m + B_n (c \cdot d\tilde{t}_O)_n = \begin{bmatrix} B_m & 0 \\ 0 & B_n \end{bmatrix} \begin{bmatrix} (c \cdot d\tilde{t}_G)_m & 0 \\ 0 & (c \cdot d\tilde{t}_O)_n \end{bmatrix} \\
&= B_1 Y_1
\end{aligned} \tag{3.18}$$

we can reach a conclusion that from the equation (3.18), in theory, MIS is equivalent to MDS.

3.3 Experiment and analysis of results

Based on the equal between ISB and the increment of other system clock error and GPS clock error (i.e., equation (3.16)), the equivalence of these two models has been proved theoretically in the previous section. To further verify the numerical equivalence, the experiment will be performed in this section to check the numerical difference between the two models. If the results show no or tiny distinction, we will realize the extension of equivalence proof from theory to numerical verification.

Table 3.1 The details of eight stations used in the test.

Station ID	Location			Receiver type	Receiver clock type
	Lat.	Long.	Height		
CUT0	-32.0039	115.8948	24.000	TRIMBLE NETR9	INTERNAL
KARR	-20.9814	117.0972	109.247	TRIMBLE NETR9	INTERNAL
MRO1	-26.6966	116.6375	354.069	TRIMBLE NETR9	INTERNAL
PERT	-31.8019	115.8852	12.920	TRIMBLE NETR9	INTERNAL
MOBS	-37.8294	144.9753	40.578	SEPT POLARX4TR	INTERNAL
NNOR	-31.0487	116.1927	234.984	SEPT POLARX4	EXTERNAL SLAVED CRYSTAL
STR1	-35.3155	149.0109	800.032	SEPT POLARX5	EXTERNAL CESIUM
YAR2	-29.0466	115.3470	241.291	SEPT POLARX4TR	EXTERNAL H-MASER

Observations from 8 MGEX stations (CUT0, KARR, MRO1, PERT, MOBS, NNOR, STR1, YAR2) will be tested in this section. In accordance with the receiver type, these stations can be segregated into two groups (TRIMBLE and SEPT), which is useful for the validation of the characteristic of ISB for different type receivers. The details of the stations are listed in Table 3.1.

Herein, corresponding with the two different ISB function models (MIS and MDS), two schemes are designed for the comparison. The data of GPS and BDS, GPS and Galileo in GPS week 1965 (from Sept. 03 to 09, 2017, DOY from 246 to 252) are both utilized in this study. Details of the models and strategies related to data processing are shown in Table 3.2.

Table 3.2 The models and strategies for data processing.

Item	Models/Strategies
Data	GPS+BDS/GPS+Galileo, 8 stations
Observations	Undifferenced ionospheric-free code and phase combination
Singal selection	GPS:L1&L2 BDS:B1&B2 GAL:E1&E5a
Estimator	Kalman filter
Elevation cut off	7°
Interval rate	30 s
Satellite orbit and clock	Fixed to MGEX (<i>GBM</i>) products
Zenith tropospheric delay	Saastamoinen model & random walk process; GMF is used
Ionospheric delay	First order effect eliminated by ionospheric-free linear combination
Receiver phase center	PCO and PCV for GPS from igs14.atx are used; Corrections of BDS and GAL are applied the same with GPS
Satellite phase center	PCO and PCV are used with igs14.atx
Windup effect	Corrected
Tidal effects	Corrected with solid tides, ocean loading, and polar tides
Receiver clock/ISB	Model MIS: all receiver clock estimated as a white noise Model MDS: GPS receiver clock and ISB estimated as a white noise
Phase ambiguities	Estimated as constant for each arc

3.3.1 Comparison of positioning accuracy and convergence time

To further compare the difference between Scheme MIS and MDS, and verify the equivalence, both positioning errors and convergence time will be analyzed. Up to now, there has been no clear definition for the criterion of convergence time. In this study, the positioning error is derived from the difference between positioning results and the true values (the IGS solution results). Then, if the epoch is the first time that the positioning error reaches 0.1 m, and meanwhile each error of the following 20 epochs is below 0.1 m, we define the time of this epoch as the moment of convergence. With this criterion, the convergence time in North, East, and Up components can be attained, correspondingly. The maximum of three directions is regarded as the final convergence time. Typically, the root-mean-square (RMS) statistics of positioning results is made without the period of convergence; Accordingly, at first, the convergence time of PPP processing in these two schemes should be detected and compared. Figure 3.1 shows the convergence time of schemes MIS and MDS from DOY 246 to 252, 2017.

246_MIS 246_MDS 247_MIS 247_MDS 248_MIS 248_MDS 249_MIS
 249_MDS 250_MIS 250_MDS 251_MIS 251_MDS 252_MIS 252_MDS

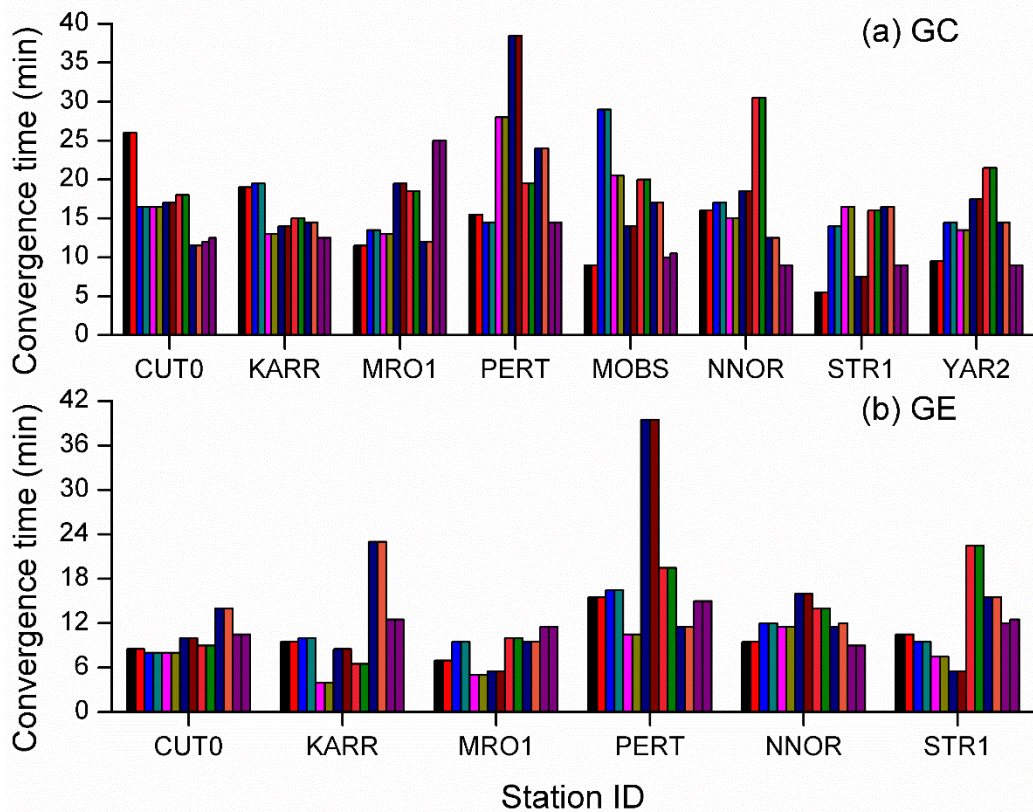


Figure 3.1 The convergence time in two scheme MIS and MDS, the subgraph (a) GC means the convergence results for GPS and BDS processing, and the GPS and Galileo processing convergence time is presented in the sub-image (b) GE.

It is noted that the convergence time of scheme MIS is nearly the same as that of scheme MDS, indicating that the two different ISB function models have equal processing time, which can be considered as a preliminary proof of equivalence for two schemes. To further analyze the difference between the two schemes, moreover, the difference of PPP processing results is compared.

Figure 3.2 displays the weekly mean RMS derived from daily positioning results from DOY 246 to 252, 2017 for the system pair of GPS/BDS in three different components. From the figure in each component (N, E, and U), we use two different color columns to represent the

solutions for the different schemes. The corresponding statistics of the RMS are listed in Table 3.3. Because of the length limit, the RMS of station CUT0 and STR1 are shown as an example.

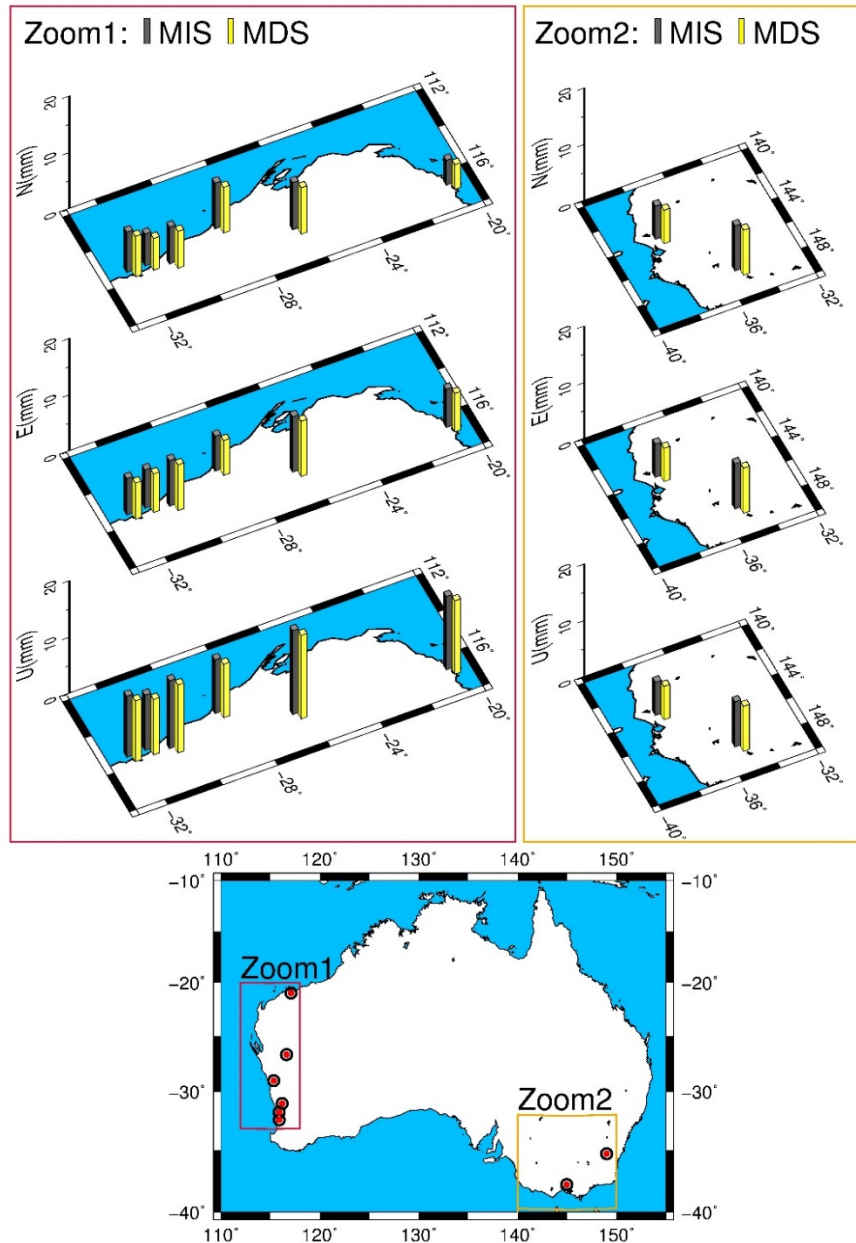


Figure 3.2 The weekly mean RMS of positioning errors in the two scheme MIS and MDS with GPS and BDS observations, the bottom subgraph shows the distribution of stations, and the top two subgraphs from up to down are the enlarged details for the mean RMS in north, east and up component, respectively.

Table 3.3 The positioning RMS in the north, east, up components in two schemes with GPS and BDS observations (unit: cm).

Station ID	CUT0						STR1					
	MIS			MDS			MIS			MDS		
	N	E	U	N	E	U	N	E	U	N	E	U
246	0.44	0.54	0.87	0.44	0.54	0.86	0.74	1.10	1.18	0.74	1.10	1.19
247	1.00	0.74	0.81	1.00	0.74	0.81	1.09	0.83	0.85	1.09	0.83	0.86
248	0.89	0.73	1.07	0.89	0.73	1.06	1.50	0.82	1.19	1.50	0.81	1.18
249	1.00	1.03	1.78	1.00	1.03	1.78	0.90	0.69	1.06	0.90	0.69	1.05
250	0.71	0.73	1.08	0.71	0.73	1.08	0.92	1.31	0.98	0.92	1.30	0.99
251	0.83	0.91	1.43	0.83	0.91	1.42	0.56	1.20	0.80	0.56	1.20	0.81
252	0.83	0.52	1.22	0.83	0.49	1.21	0.57	1.46	0.90	0.57	1.45	0.90
Mean	0.81	0.74	1.18	0.81	0.74	1.17	0.90	1.06	0.99	0.90	1.05	0.99

As evident from Figure 3.2 and Table 3.3, RMS is nearly the same on all days in the entire week the daily. In addition, the weekly mean RMS is close to equal between the two schemes. Besides the processing analysis of GPS/BDS, a similar test using GPS/Galileo observations are made as well. The mean RMS results for the GPS/Galileo are presented in Figure 3.3, with the statistics listed in Table 3.4, where also shows the RMS of stations CUT0 and STR1 as an instance. Different from the processing of GPS and BDS systems, the estimated ISB between Galileo and GPS in the stations MOBS and YAR2 exists a lot of outliers. The probable reason is that at many epochs these two stations can only observe one Galileo satellite or even no Galileo satellite. Consequently, the results of these two stations are not demonstrated in the following anymore.

Table 3.4 The positioning RMS in North, East, Up components in two schemes with GPS and Galileo observations (unit: cm).

Station ID	CUT0						STR1					
	MIS			MDS			MIS			MDS		
	N	E	U	N	E	U	N	E	U	N	E	U
246	0.52	0.59	0.64	0.52	0.58	0.64	0.75	1.10	1.15	0.75	1.10	1.16
247	0.89	0.57	0.79	0.89	0.57	0.79	1.10	1.29	1.15	1.51	1.30	1.16
248	0.82	0.60	0.69	0.82	0.60	0.69	1.46	0.86	1.37	1.46	0.86	1.37
249	0.98	1.00	0.87	0.98	1.00	0.87	0.86	0.82	1.49	0.86	0.82	1.49
250	0.69	0.70	0.83	0.69	0.70	0.83	0.98	1.00	0.81	0.98	1.00	0.82
251	0.65	0.91	0.95	0.65	0.91	0.95	0.55	0.88	0.71	0.55	0.88	0.71
252	0.66	0.62	0.89	0.66	0.62	0.89	0.60	1.15	0.86	0.60	1.15	0.85
Mean	0.75	0.71	0.81	0.74	0.71	0.81	0.90	1.01	1.08	0.96	1.02	1.08

It can be seen from Figure 3.3 and Table 3.4 that the daily RMS is close to the same and the weekly mean RMS is nearly equal between two schemes, which has a similar phenomenon as GPS and BDS processing. In other words, the results of processing in GPS and BDS data, together with the consequence in GPS and Galileo system support the proof of equivalence between two ISB function models.

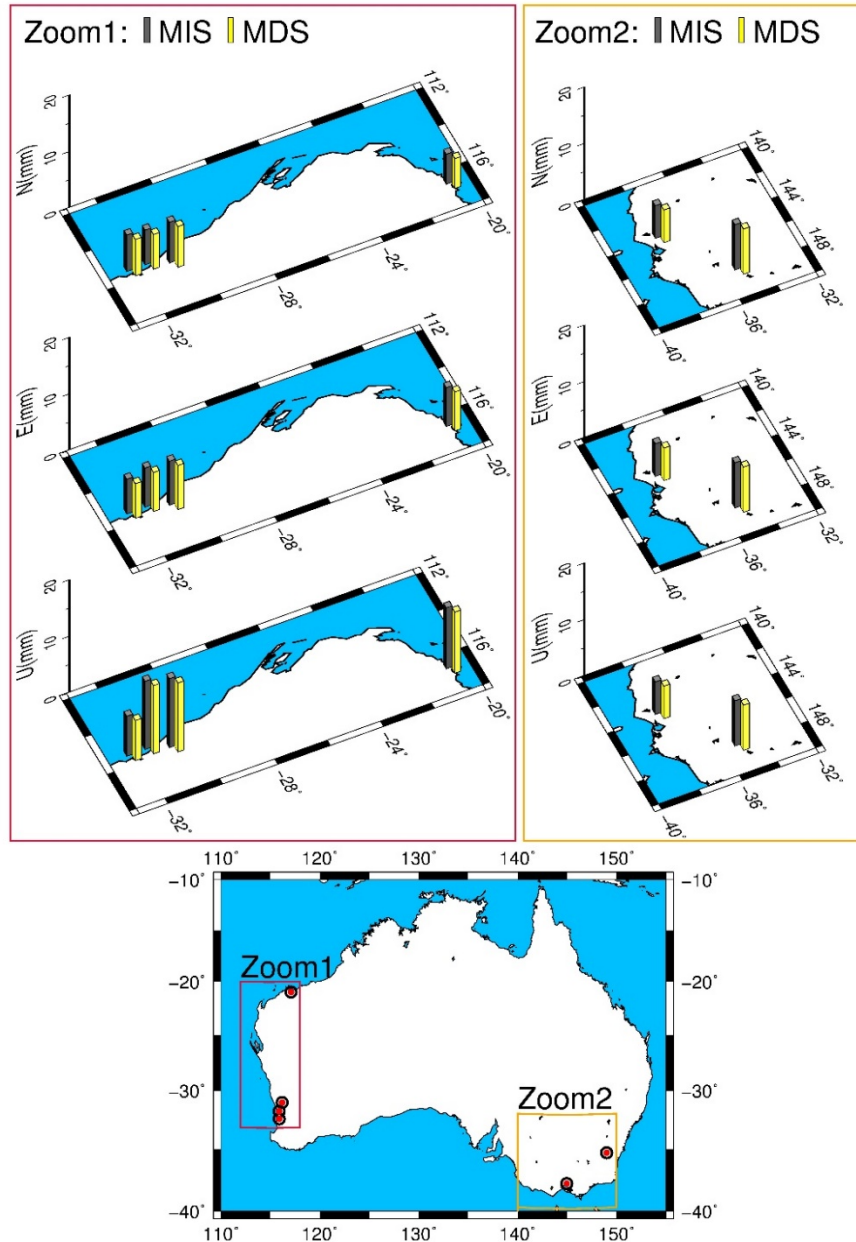


Figure 3.3 The weekly mean RMS of positioning errors in two schemes MIS and MDS with GPS and Galileo observations.

3.3.2 Comparison of different estimated ISB

From the previous analysis on GPS/BDS, and GPS/Galileo positioning RMS, it is clear that two schemes MIS and MDS are equivalent. To deeply analyze the difference between these two schemes, both the estimated ISB of GPS/BDS and GPS/Galileo are compared. The ISB

of scheme MIS is derived from the increment between receiver clocks of BDS or Galileo and GPS, while the ISB in scheme MDS is directly from the estimation processing. Figure 3.4 and Figure 3.5 show the ISB difference of two schemes between GPS/BDS and GPS/Galileo systems, respectively.

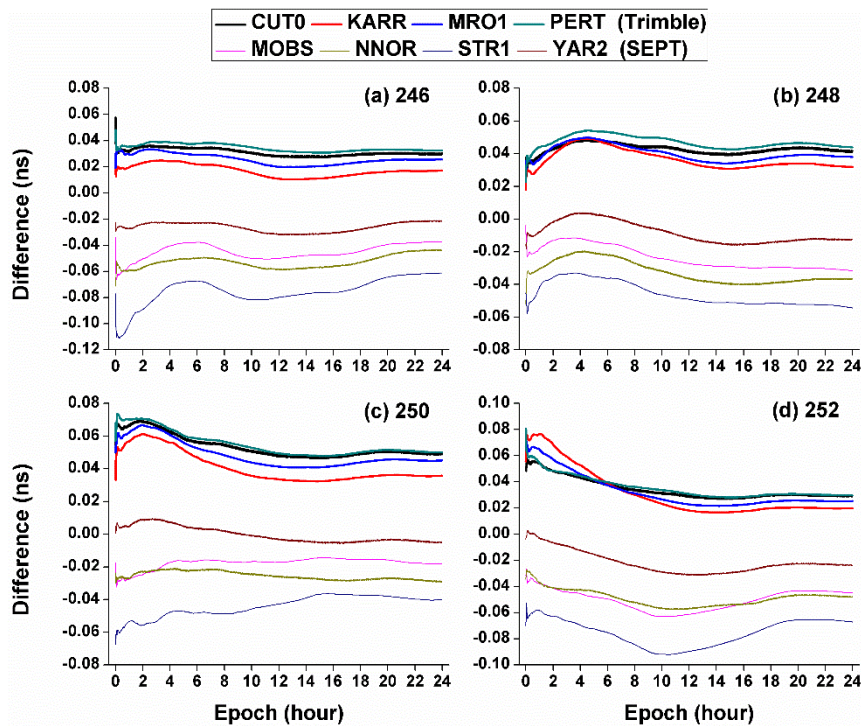


Figure 3.4 The ISB difference between GPS/BDS for two schemes (8 stations with two different types of receivers, the upper four stations are Trimble, and the under four are SEPT, due to space limitation, only 4 days are shown as an example, unit: ns).

From Figure 3.4 and Figure 3.5, we can see that different receiver type has different signs of ISB increment (positive or negative) between two schemes. Besides, the four stations of receiver group Trimble have a very similar trend line with approximate values, while those of the SEPT group although having similar trend lines, but with different values. The possible reason may be caused by the different types of receiver clock, all stations in the Trimble group use the internal receiver clock, and for the SEPT group, four stations install four different kinds of receiver clock. Three of them are installed with an extra precise atomic clock, suggesting that the estimated receiver clock will have a well-behaved physical property, i.e., a strong

constraint. Therefore, the diversities between the different stations will go into the ISBs. The formal estimated ISB is shown in Figure 3.6, where we take the ISB from MIS as an example. From the figure, we can see that the estimated ISB has the same phenomenon as the difference of ISB between two schemes, which is the ISB difference in the same receiver type has different values is caused by the estimated ISB with different values.

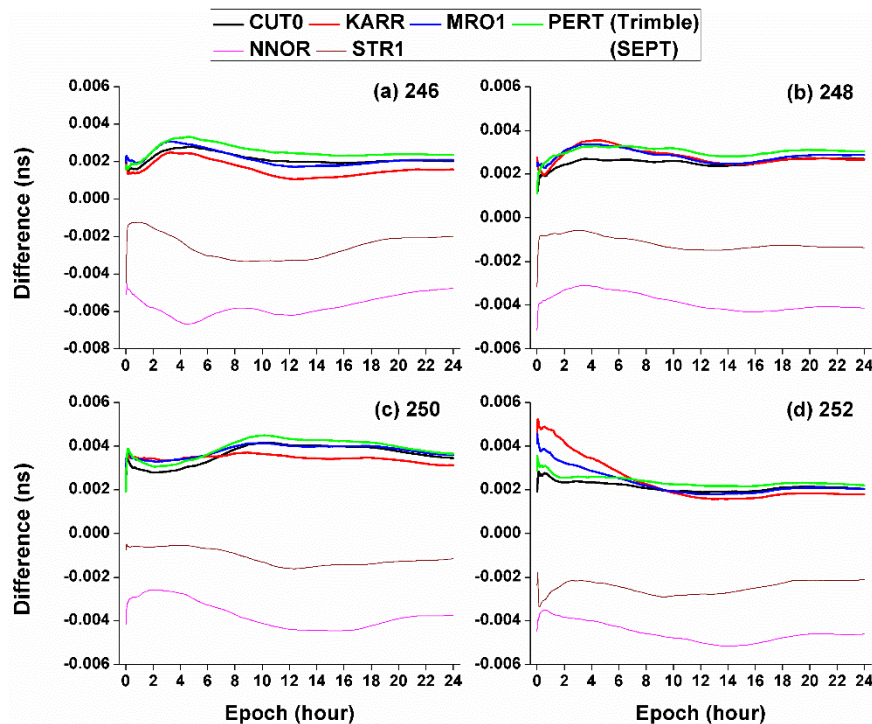


Figure 3.5 The ISB difference between GPS/Galileo for two schemes (6 stations with two different types of receivers, the upper four stations are Trimble, and the under two are SEPT, due to space limitation, only 4 days are shown as an example, unit: ns).

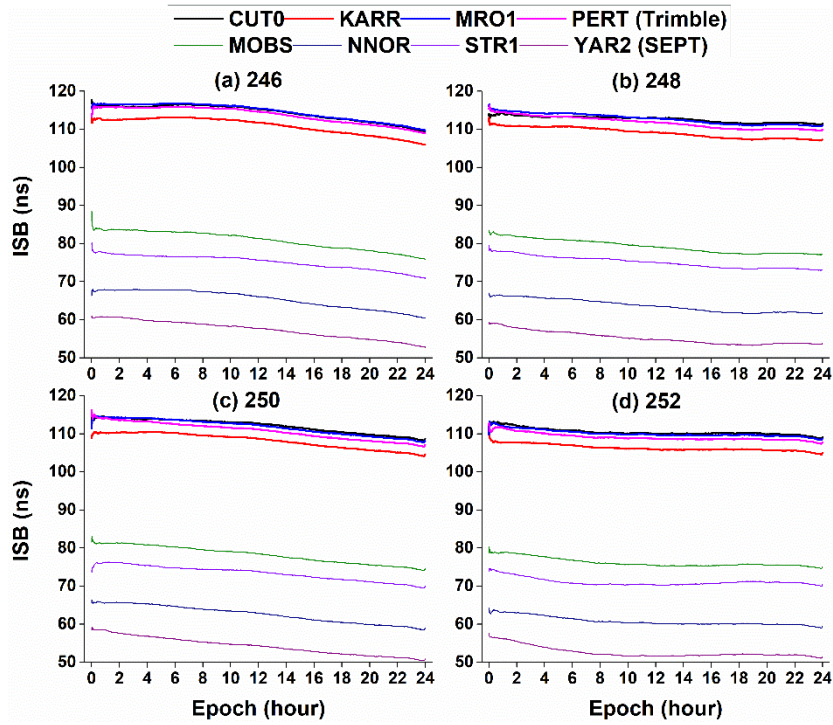


Figure 3.6 The estimated ISB in GPS/BDS systems (8 stations with two different types of receivers, the upper four stations are Trimble, and the under four are SEPT, due to space limitation, the ISB from MIS in 4 days are shown as an example, unit: ns).

To show the ISB difference level more clearly, the statistics of daily mean difference, weekly mean difference, and weekly mean STD, together with the mean value of two receiver group without the results of the convergence period are illustrated in Figure 3.7.

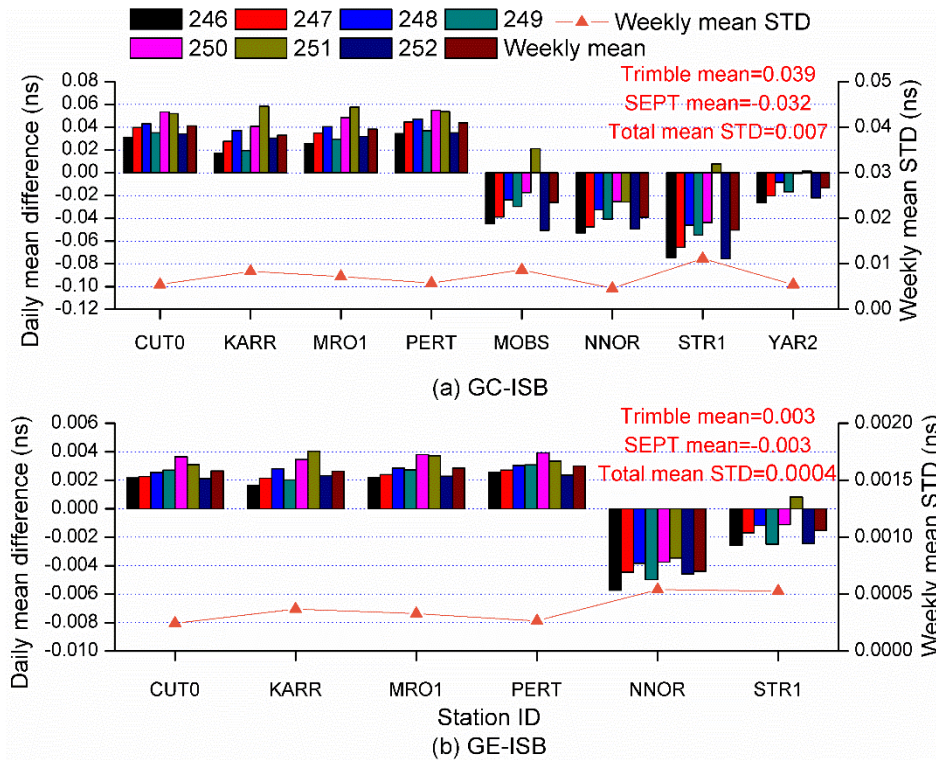


Figure 3.7 The daily mean, weekly mean difference, and the weekly mean STD of ISB increment between two schemes, up subfigure (a) is the description of GPS and BDS systems, while the down sub-picture (b) is about GPS and Galileo systems. The weekly mean value is in a wine column, and the right vertical axis shows the weekly mean STD, unit: ns.

From Figure 3.7, it is clear that in GC system, the mean ISB difference between two schemes using Trimble and SEPT receivers is 0.039 ns and -0.032 ns (about 1.1 cm and 9.6 mm on the distance), respectively. It may depend on the accuracy level of BDS precise clock products, and the measurement noise. However, this level of ISB difference can be ignored in the following positioning from the comparison of positioning RMS in Figure 3.2; wherein there is nearly no difference between the two schemes. Concerning the total weekly mean STD, it is 0.007 ns (about 2.1 mm on the distance), which means the ISB difference between the two schemes is stable and negligible. While for the GE system, the mean value of ISB difference in Trimble and SEPT group can reach 0.003 ns and -0.003 ns (both about 0.9 mm), respectively, in addition, the total weekly mean STD achieves 0.0004 ns (about 0.1 mm). The

result for GE system is an order of magnitude higher than that of GC system, which may be caused by the higher accuracy of Galileo satellite clock products, and the closing time system and coordinate system to GPS. From the comparison of ISB between two schemes, the equivalence of two different ISB function models (MIS and MDS) is further proved.

3.4 Summary

In this chapter, the equivalence of two different ISB function models (MIS and MDS) is firstly proved with the theoretical approach. To deeply investigate the proof of the equivalence in the numerical examples, we apply the data from eight stations in MGEX network with the GPS, BDS, and Galileo during the GPS week 1965 (DOY 246 to 252, 2017). We processed not only the comparison of positioning results and convergence time, but also the comparison of the ISB derived from the two different models.

At first, the RMS of positioning results and convergence time from two schemes using the GPS/BDS and GPS/Galileo data are investigated, which shows in both data pairs, the convergence time of scheme MIS is well equal with that of scheme MDS, suggesting that the two different ISB function models have the same convergence rate. To further prove the equivalence between two schemes, besides, the PPP processing results are compared. From the RMS results of two schemes, the daily RMS in the entire week is nearly the same between two schemes, as well as the weekly mean RMS. Therefore, the conclusions can be made that both in the GPS/BDS case and the GPS/Galileo case, the fundings entirely support the theoretical proof of equivalence between two ISB function models.

After that, we analyzed the characteristic of ISB derived from the two different models. According to the types of receiver, the same receiver group has the same trend, but sometimes different values, which may be caused by the different types of the clock inside the receiver. In this study, different receiver type shows different signs of ISB increment between two schemes. As evident from the statistics of daily, weekly mean values, and receiver group total

mean of ISB difference derived from the two function models, the estimated ISBs from the different models are close to consistent, the difference between two ISBs is about 1cm on distance with GPS/BDS data, which can be neglected in PPP processing. For the GPS/Galileo, it can reach to 0.9 mm, which means two kinds of ISB can be regarded as identical. With the analysis of ISB between two schemes, the equivalence of two different ISB function models (MIS and MDS) has been further proved. Accordingly, both the theoretical proof and numerical verification have been successfully proved, which denotes the equivalence of the two different ISB models (MIS and MDS). Ultimately, we choose the MDS as the candidate of the function model to apply in the following PPP processing.

4 Assessment of different stochastic models for ISB

4.1 Introduction

Because the different time systems, reference frames, and hardware delays within receivers were used in different systems (Montenbruck et al. 2011; Torre and Caporali 2015). If we blindly make use of the observations from all systems without any calibration of these differences, it will lead to a poor accuracy result, and in some cases even having a worse result as compared with the single system PPP. Therefore, the differences between each system need to be carefully considered and calibrated, which is a necessary procedure for the multi-systems integrated positioning. Usually, ISB is introduced to cover all these differences between two different systems (Chen et al. 2016; Jiang et al. 2017; Li et al. 2015c). It is usually estimated together with other unknown items, like coordination, receiver clock, tropospheric delay, and so on. Concerning the stochastic models of ISB estimation, often, a strategy of considering ISB as an arc-dependent constant is applied in Paziewski and Wielgosz (2014), Li et al. (2015e), Guo et al. (2016), and Lou et al. (2016). Jiang et al. (2017) regard ISB as a piece-wise parameter, which can increase the sample size and is useful for ISB modeling and prediction. Besides these two strategies, another two stochastic models can be utilized as well that are considering ISB as white noise or random walk. Nevertheless, until now no specific analysis has been made to assess the difference between these stochastic models and its impact on the ISB estimation. Accordingly, in this chapter, we will evaluate and compare the impact of different stochastic models on ISB, positioning accuracy, and processing time.

This chapter starts with the descriptions of four different ISB stochastic models and five designed schemes in Section 4.2. Then, the experimental data and processing strategies are declared in Section 4.3. The results and analysis are shown in Section 4.4, wherein pseudorange observation residuals, convergence time and positioning accuracy with *GBM*

and *WUM* precise products, and accuracy improvement during the convergence time are discussed and compared with five different strategies. Eventually, the summary of this chapter is made in Section 4.5.

4.2 Descriptions of ISB stochastic models

Generally, in our multi-GNSS combined processing model, we introduce an extra ISB parameter to cover the effect of the difference between the two systems, here we will take GPS and BDS systems as an example. To not only verify the role of this additional parameter but also compare the impact of different ISB estimation stochastic models for the positioning, five different schemes are designed in this study. The differences between the five schemes mainly focus on the configurations on the ISB. Here, we will take one 3-h processing-arc-window containing 360 observation epochs as an example.

- Neglecting inter-system bias between GPS and BDS is named ISB-OFF, which means the positioning model of BDS and GPS is separated, and the two systems are processed without any relation. The BDS observations are processed the same as GPS ones. However, the ISB between GPS and BDS will remain in the BDS processing model and will be reflected in the pseudorange residuals. The configuration equation can be expressed as:

$$ISB_{OFF} = [NULL_1 \quad NULL_2 \quad \cdots \quad NULL_{359} \quad NULL_{360}]^T \quad (4.1)$$

where ISB_{OFF} is the ISB in the scheme ISB-OFF. $NULL_1$ to $NULL_{360}$ is an empty matrix which means without considering ISB.

- Estimating the ISB as a piece-wise constant every 30 min (ISB-PW). ISB parameter is initialized at the first epoch, then re-initialized, and updated every 30 min (Jiang et al. 2017). The configuration equation can be written as:

$$\begin{aligned}
ISB_{PW} &= [ISBP_1 \quad ISBP_2 \quad ISBP_3 \quad ISBP_4 \quad ISBP_5 \quad ISBP_6]^T \\
ISBP_i &= \left[\overbrace{ISB_i \quad ISB_i \quad \cdots \quad ISB_i \quad ISB_i}^{60} \right], \quad i = 1, 2, 3, 4, 5, 6
\end{aligned} \tag{4.2}$$

where ISB_{PW} means the ISB in the scheme ISB-PW. The ISB in one 3-h processing-arc window can be divided into six parts according to the size of piece-wise (every 30 min), which are denoted as $ISBP_1$ to $ISBP_6$. $ISBP_i$ is one piece-wise ISB, and i is from 1 to 6.

- Estimating the ISB as random-walk processing (ISB-RW). With this scheme, ISB is initialized at the first epoch, and then with a time-related spectral density of $0.001 \text{ m} / \sqrt{s}$. The configuration equation can be formed as:

$$\begin{aligned}
ISB_{RW} &= [ISBR_1 \quad ISBR_2 \quad \cdots \quad ISBR_{359} \quad ISBR_{360}]^T \\
ISBR_i &= ISBR_1 + sd \times 30 \times (i - 1), \quad i = 1, 2, \dots, 359, 360
\end{aligned} \tag{4.3}$$

where ISB_{RW} is the ISB in the scheme ISB-RW. $ISBR_i$ is the ISB for one epoch, with i from 1 to 360. sd means the time-related spectral density.

- Estimating the ISB as a processing-arc-dependent constant (ISB-AD). During the whole processing-arc period, ISB is only initialized at the first epoch. If the processing-arc window is one day, this means the ISB is estimated as a constant each day. In this paper, we make the period of our processing tests as 3 h, so the ISB is considered to be a 3-hour arc-dependent constant. The configuration equation can be indicated as:

$$ISB_{AD} = \left[\overbrace{ISB \quad ISB \quad \cdots \quad ISB \quad ISB}^{360} \right]^T \tag{4.4}$$

where ISB_{AD} means the ISB in the scheme ISB-AD, which is estimated as a constant during the 3-h processing-arc window.

- Estimating the ISB as white noise (ISB-WN). In this way, the ISB is initialized for each epoch, which is the same as the normal processing mode as the receiver clock error. The configuration equation can be shown as:

$$ISB_{WN} = [ISB_1 \quad ISB_2 \quad \dots \quad ISB_{359} \quad ISB_{360}]^T \quad (4.5)$$

where ISB_{WN} means the ISB in the scheme ISB-WN. The ISB will be initialized and estimated in each epoch.

For convenience, the five schemes mentioned above marked as ISB-OFF, ISB-PW, ISB-RW, ISB-AD, and ISB-WN, correspondingly, are summarized in Table 4.1.

Table 4.1 The description of GPS/BDS ISB estimating schemes.

Schemes	Descriptions
ISB-OFF	Neglecting inter system bias
ISB-PW	Estimating the ISB as piece-wise constant
ISB-RW	Estimating the ISB as a random walk processing
ISB-AD	Estimating the ISB as a processing arc-dependent constant
ISB-WN	Estimating the ISB as white noise

4.3 Experimental data and processing strategies

In order to investigate the different proposed ISB estimation stochastic models and the impact of the additional ISB on PPP performance, observations from 8 stations in the MGEX network, named as CUT0, KARR, MRO1, PERT, MOBS, NNOR, STR1, and YAR2, were chosen, covering a one-week period that is GPS week 1965 with the DOY (day of year) from 246-252, 2017. These eight stations are all located in Australia, where they can usually observe more than 7 BDS satellites (Yang et al. 2014). The distribution and the receiver types equipped in the stations are displayed in Figure 4.1 and Table 4.2.

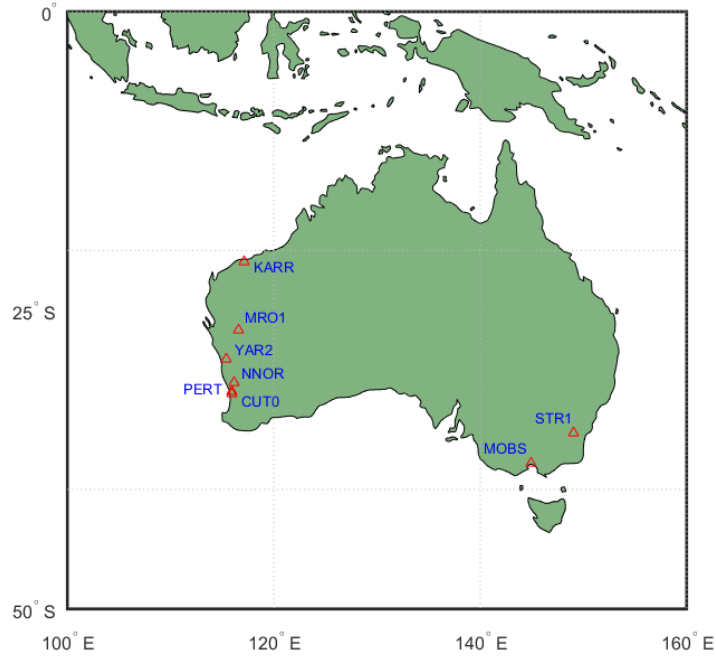


Figure 4.1 Distribution of the selected stations.

Table 4.2 Details of 8 selected stations location and receiver types.

Station ID	Location			Receiver type
	Lat.	Long.	Height	
CUT0	-32.0039	115.8948	24.000	TRIMBLE NETR9
KARR	-20.9814	117.0972	109.247	TRIMBLE NETR9
MRO1	-26.6966	116.6375	354.069	TRIMBLE NETR9
PERT	-31.8019	115.8852	12.920	TRIMBLE NETR9
MOBS	-37.8294	144.9753	40.578	SEPT POLARX4TR
NNOR	-31.0487	116.1927	234.984	SEPT POLARX4
STR1	-35.3155	149.0109	800.032	SEPT POLARX5
YAR2	-29.0466	115.3470	241.291	SEPT POLARX4TR

In this experiment, data from the selected stations are processed by a Kalman filter with a sliding window of 3 hours one station by one station, which means the 24-h observation data for each station will be segregated into eight processing sessions. GPS and BDS combined

PPP in static and simulated kinematic modes are applied in our study. In static PPP mode, the solution strategy for position coordinates is to treat as contents, while for the kinematic PPP mode, they are estimated as white noise in each epoch. The MGEX precise products from analysis centers (ACs) GFZ (*GBM*) and Wuhan University (*WUM*) are used to fix the satellite orbit and clock. The details of models and strategies related to the data processing are listed in Table 4.3.

Table 4.3 Models and strategies for data processing

Item	Models/Strategies
Data	GPS+BDS, 8 stations
Processing arc-window	3 hour, 8 stations in one week period totally have 448 tests
Singal selection	GPS:L1&L2 BDS:B1&B2
Estimator	Kalman filter
Elevation cut off	7°
Interval rate	30 s
Satellite orbit and clock	Fixed to MGEX (<i>GBM</i> or <i>WUM</i>) products
Zenith tropospheric delay	Saastamoinen model & random walk process; GMF is used
Ionospheric delay	First order effect eliminated by the ionospheric-free linear combination
Receiver phase center	PCO and PCV for GPS from igs14.atx are used; Corrections of BDS is applied the same with GPS
Satellite phase center	PCO and PCV are used with igs14.atx
ISB	Schemes ISB-OFF, ISB-PW, ISB-RW, ISB-AD, ISB-WN
Phase ambiguities	Estimated as constant for each arc

4.4 Results and discussion

This section presents the results and analysis performed to assess the differences between diverse ISB stochastic models and their impacts on positioning accuracy and convergence time. As advocated before, when the processing is re-initialized, which is considered as a cold start. Therefore, there will be eight times per day to evaluate the influence on convergence

time. A time slide window of 3 hours is chosen to ensure enough time for converging into a certain accuracy in almost all the cases and offer enough test samples. With the integration of the entire experiments over all stations, it contains 448 cold starts (8 stations \times 7 days \times 8 initializations).

The statistical analysis of positioning errors with respect to the station coordinates from the IGS weekly solutions are utilized with the 68% and 95% quantiles. These two statistical parameters are chosen instead of mean and standard deviation due to the possible remaining biases that might cause results do not follow a normal distribution (Jr et al. 2017). The convergence time is defined as when the positioning error is lower than 0.2 m (95%) and 0.1 m (68%) in the North, East, and UP components (Lou et al. 2016). This statistical approach is also applied in Bree and Tiberius (2012), Jr et al. (2017), and Zhou et al. (2018).

Since different MGEX analysis center (*GBM*, or *WUM*) has its own strategy to attain precise multi-systems orbit and clock products, as well as the ISB stochastic models during the products generation. In this study, we will introduce the precise products from *GBM* and *WUM* to validate the differences between these two kinds of products and analyze the potential impact on the different ISB estimation strategies utilized in different ACs on the positioning and convergence time.

4.4.1 Pseudorange observation residuals

As known, the remaining measurement noises and other unmodeled errors will be assimilated by the observation residual, which is an effective indicator to assess the accuracy of the positioning model.

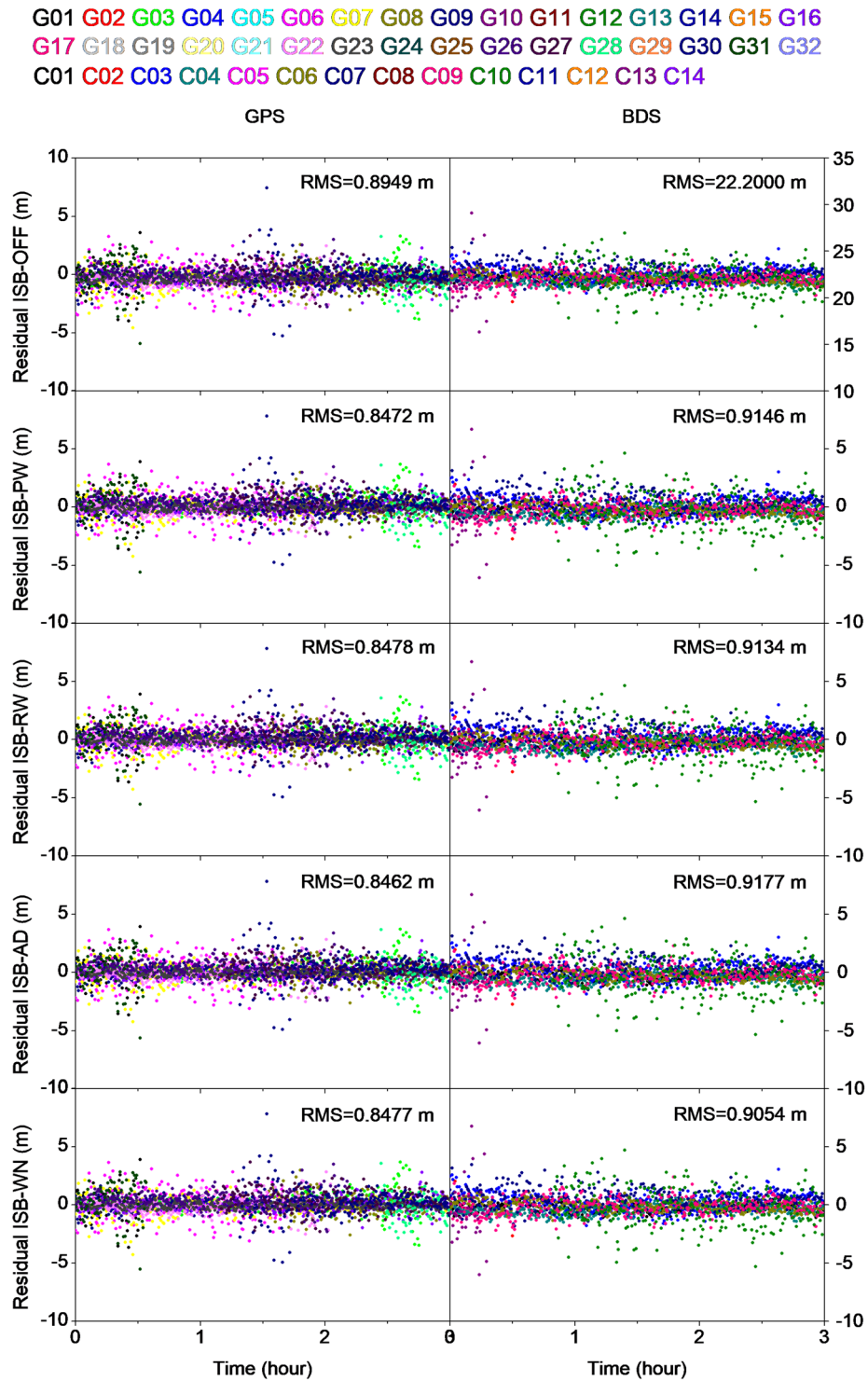


Figure 4.2 Ionospheric-free pseudorange observation residuals of GPS and BDS systems at STR1 station as an example on DOY 251, 2017, here is the results of the first 3h period with static PPP mode, left column is the GPS system, the right one denotes the BDS system, from top to bottom represents different schemes.

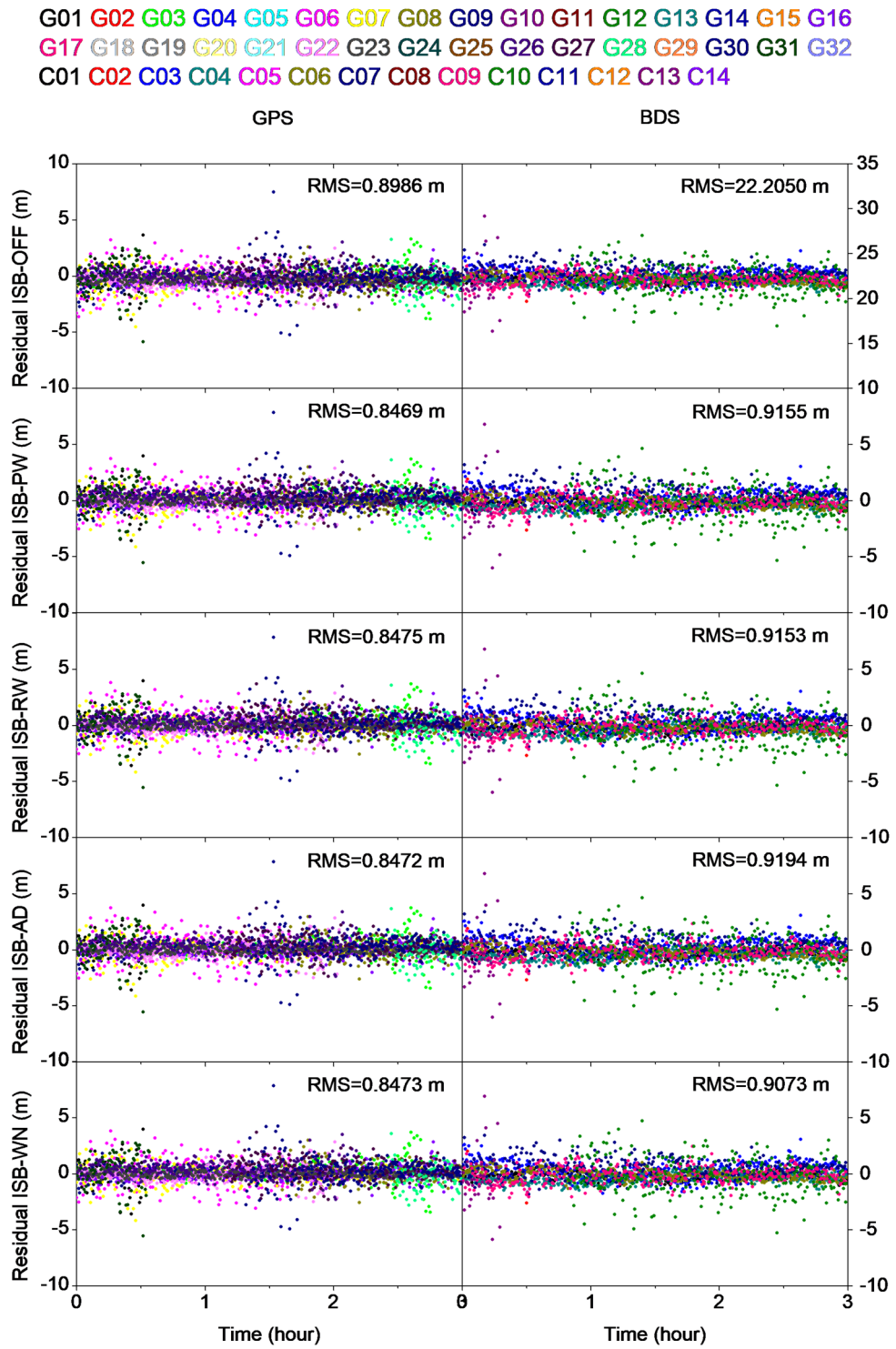


Figure 4.3 Ionospheric-free pseudorange observation residuals of GPS and BDS systems at STR1 station as an example on DOY 251, 2017, it is the results for the first 3h period with kinematic PPP mode.

The pseudorange residuals at the station STR1 (with the *GBM* products as an example) of each satellite with different colors in GPS and BDS are shown in Figure 4.2 and Figure 4.3. Figure 4.2 is the result of static mode, while Figure 4.3 is that of kinematic mode. As evident from the figures, both in the static and kinematic mode, as compared with considering ISB, neglecting ISB (ISB-OFF) will lead to a higher pseudorange residual. Following the introduction of the ISB parameter (ISB-PW, ISB-RW, ISB-AD, and ISB-WN), the ionospheric-free pseudorange (PC) residuals in GPS will averagely improve 4.8 cm (i.e., 5.4%) in static mode, and 5.1 cm (i.e., 5.7%) in kinematic mode. The improvement is not apparent, which is in accordance with the ISB processing strategy that considering the GPS receiver clock as the reference clock, together with ISB covering the difference between BDS and GPS. As for the BDS system, the PC residual of ISB-OFF is most considerable, because ISB does not absorb the remaining errors and difference, which go into the residual. The statistical results of other four schemes are similar, and as compared with ISB-OFF, the PC residual RMS of ISB-PW, ISB-RW, ISB-AD, and ISB-WN can reduce by 21.3 m (95.9%) both for static mode and kinematic mode. Accordingly, it is necessary to consider the ISB parameter in multi-GNSS combined positioning.

4.4.2 Convergence time and positioning accuracy

Positioning accuracy is evaluated by the comparison of the coordinates with true external values, which are attained from the final IGS weekly solution. Concerning the convergence time, we take the statistical methodology of 68% and 95% quantiles as mentioned above. In the 68% quantile case, we make the convergence time as the first epoch time whose error is lower than 0.1 m. As for the 95% quantile, the criterion is lower than 0.2 m.

The case with *GBM* precise products

Figure 4.4 presents the errors in North (N), East (E), and UP (U) components of GPS/BDS combined static PPP in different schemes. Meanwhile, Table 4.4 shows the convergence time in the N, E and U components, based on the statistics over all the tests.

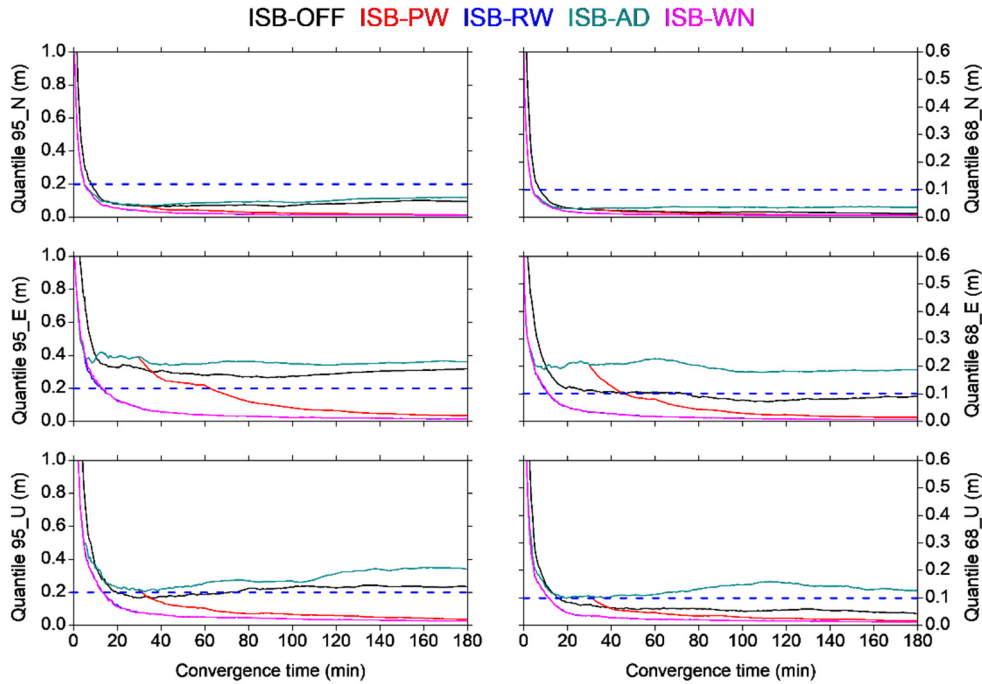


Figure 4.4 GPS/BDS combined static PPP convergence performance in five different schemes with *GBM* precise products, each scheme uses a different color, left side is the errors of 95% quantile, while the right side is the errors of 68% quantile.

Table 4.4 Convergence times of GPS and BDS combined static and kinematic PPP in five different schemes (unit: min)

	Static (95%)			Static (68%)			Kinematic (95%)			Kinematic (68%)		
	N	E	U	N	E	U	N	E	U	N	E	U
OFF	8.5	-	20.0	7.5	74.5	16.0	14.5	-	-	11.5	-	25.0
PW	5.0	63.0	31.0	4.5	45.5	31.0	7.5	72.5	34.5	6.0	63.5	25.5
RW	5.0	13.0	13.5	4.0	11.5	12.0	7.0	20.5	18.0	5.5	16.0	14.0
AD	5.0	-	-	4.5	-	-	7.5	-	-	6.0	-	25.5
WN	5.0	13.5	14.0	4.5	11.5	12.0	7.5	19.5	17.5	5.5	17.5	13.5

As evident from Figure 4.4 and Table 4.4, PPP performance at some component in ISB-OFF, and ISB-AD schemes cannot converge during the processing arc-windows. It also can be seen that using the *GBM* products, the convergence time of ISB-OFF is 8.5 min and 20.0

min in N, and U components at 95% quantile. It takes 7.5 min, 74.5 min, and 16.0 min to converge into the 68% quantile in three components. As for the N component, the convergence time of four schemes with ISB, ISB-PW, ISB-RW, ISB-AD, and ISB-WN, is averagely improved by 41.2% from 8.5 min to 5.0 min, and 41.7% from 7.5 min to 4.4 min at 95% and 68% quantile, respectively. That means after considering the ISB, the convergence rate is fasted as compared with ISB-OFF. The convergence time of ISB-PW at the U component is longer than ISB-OFF, which may be caused by the stochastic model of ISB-PW here is not consistent with the model of ISB estimation applied by GFZ for precise products generation, which is not declared in any reference, but we have confirmed it with the colleague in GFZ. We conclude that this inconsistency will slow down the ISB convergence rate, and the PPP performance time will be increased correspondingly. At E component, ISB-PW performs faster than ISB-OFF. It also can be seen that ISB-RW and ISB-WN have similar results and the best performance among the proposed schemes. ISB-PW performs better than ISB-AD, and at the end of the 3h period, its accuracy can reach closer to ISB-RW, and ISB-WN. It is quite incredible that as compared with ISB-OFF, ISB-AD has a weaker result. In other words, GPS/BDS combined PPP considering the ISB with *GBM* products performs worse than neglecting the ISB, which is primarily due to the inconsistency of ISB stochastic model during PPP processing and precise products generation. Accordingly, we recommend PPP users to adopt the same stochastic model of ISB estimation as the analysis center.

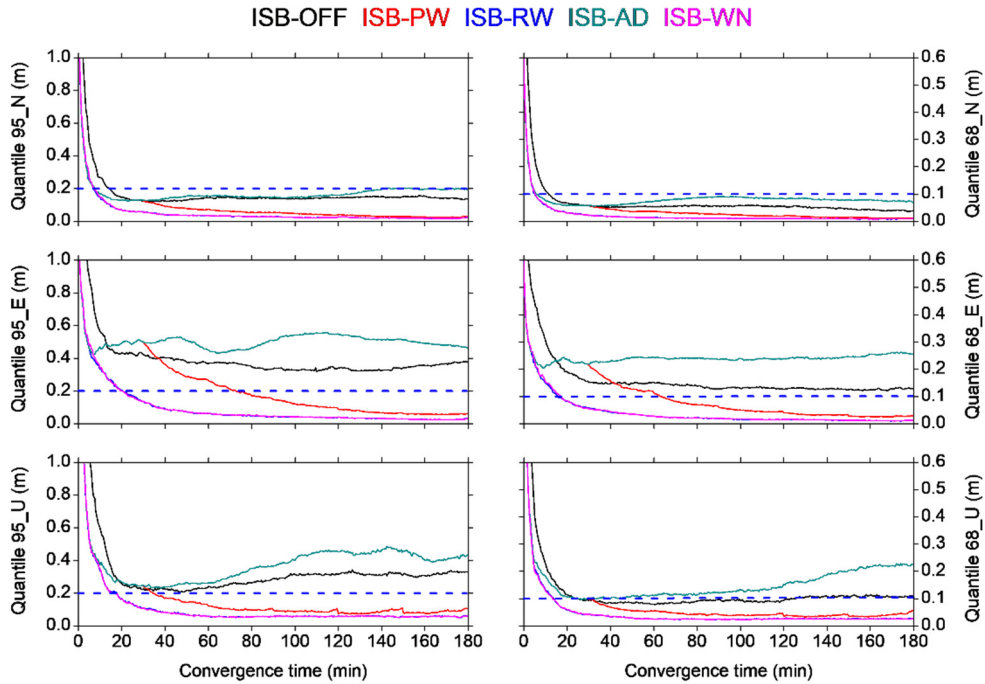


Figure 4.5 GPS/BDS combined kinematic PPP convergence performance with five different schemes.

Figure 4.5 indicates the errors in N, E, and U components of kinematic PPP with different schemes, and Table 4.4 shows the convergence time of kinematic PPP at the 95% and 68% quantile in three distinct components. It can be seen that the convergence times of all schemes in kinematic mode are longer than the static mode, because of different coordinate estimation strategies. However, similar to the static PPP, both at 95% and 68% quantile, ISB-AD has the worst performance in the convergence time; on the other hand, ISB-RW and ISB-WN perform best. PPP performance cannot be converged in E, and U components for ISB-OFF, and ISB-AD at 95% quantile. As for the 68% quantile, there are no convergence time values in E component. Compared with ISB-PW, the convergence time of ISB-RW at 95% quantile can be improved by 71.7% from 72.5 min to 20.5 min in E component, and 47.8% from 34.5 min to 18.0 min in U component, respectively. With respect to the 68% quantile, the improvement can reach 74.8% from 63.5 min to 16.0 min in E component, and 45.1% from 25.5 min to 14.0 min. ISB-WN performs similarly as ISB-RW. It can also be noted that the convergence time in the U component is shorter than that in E component in ISB-PW, ISB-RW, and ISB-WN. The

first reason may be the phase ambiguities are more correlative with the E component than U component, the convergence time of E component can be enlarged because of their correlation with phase ambiguities (Blewitt 1989). The second reason may be caused by the GPS and BDS satellites with north-south ground tracking in the earth-fixed reference frame (Melbourne 1985).

Table 4.5 Positioning accuracy of GPS/BDS combined static and kinematic PPP with five different schemes (unit: cm).

	Static (95%)			Static (68%)			Kinematic (95%)			Kinematic (68%)		
	N	E	U	N	E	U	N	E	U	N	E	U
OFF	9.5	31.9	23.6	1.3	9.3	4.3	14.6	34.6	31.8	4.6	12.7	10.7
PW	1.4	3.6	3.9	0.7	1.6	1.8	2.9	6.7	8.6	1.4	3.0	3.8
RW	1.2	1.6	2.7	0.7	0.7	1.3	2.0	3.0	5.8	0.8	1.3	2.6
AD	12.0	36.3	34.3	3.6	18.9	12.8	19.1	50.6	43.8	7.9	24.8	19.8
WN	1.2	1.6	2.8	0.7	0.7	1.3	2.0	3.0	5.8	0.8	1.3	2.6

GPS/BDS combined positioning accuracy in static and kinematic modes for five different schemes is listed in Table 4.5. In static PPP, we make the statistics using the result at the last epoch. As for the kinematic mode, since PPP performance cannot converge in some schemes, we make statistics with the same processing period, herein, using two hours later for each test. We can see from the table that ISB-RW and ISB-WN have a similar processing accuracy, and perform best, differently, ISB-AD makes the worst performance. AS compared with ISB-AD, in static PPP at 95% quantile, the accuracy of ISB-RW and ISB-WN are improved by 90% from 12.0 cm to 1.2 cm, 95.6% from 36.3 cm to 1.6 cm, and 91.8% from 34.3 cm to 2.8 cm in N, E, and U components, correspondingly. At 68% quantile, the remarkable improvement can also be achieved with 80.6%, 96.3%, and 89.8% in three components. For kinematic mode at 95% quantile, the accuracy improvements are 89.5% from 19.1 cm to 2.0 cm, 94.1% from 50.6 cm to 3.0 cm, and 86.8% from 43.8 cm to 5.8 cm in N, E, and U components, respectively. While at 68% quantile, 89.9%, 94.8%, and 86.9% accuracy increment in three components

can be attained. As compared to ISB-OFF, schemes with the ISB parameter (i.e., ISB-PW, ISB-RW, and ISB-WN) can obtain an obvious accuracy improvement, which indicates the importance of considering ISB. Accordingly, we conclude that from the validation of convergence time and performance accuracy using the *GBM* precise products, it is essential to introduce the ISB parameter, and estimate it as a random walk processing, or white noise, if you want to get a higher processing precision in a short time period (e.g., 3 hours in this study). The method of ISB estimated as an arc-dependent constant (ISB-AD) is not recommended, because the estimation strategy applied in ISB-AD is most remarkably different from that of the *GBM* products, which will cause the longest convergence time and worst positioning accuracy.

The case with WUM precise products

The convergence performance of GPS/BDS combined kinematic PPP in five different schemes using *WUM* precise products is demonstrated in Figure 4.6. Correspondingly, Table 4.6 presents the statistics of convergence time and positioning accuracy. The ISB stochastic model applied in AC Wuhan University is treated as an arc-dependent constant (Guo et al. 2016). As evident from the figure and the table, fully different from the tests with the *GBM* products, the performances using the *WUM* products have similar accuracy level whether considering the ISB parameter or not. The reason may be because, after convergence, the phase observation plays a major role in positioning; together with the ISB estimation strategy utilized in *WUM* products is the same as the ambiguity processing strategy, i.e., both are estimated as a constant in each arc-window; In addition, the ISB is highly correlative with the ambiguity, so in that case if the ISB is not introduced, the impact of its error will be absorbed by ambiguity. As for the convergence time, in N component the improvements are small (6.7% from 7.5 min to 7.0 min) at 95% quantile, and at 68% quantile, it is averagely 19.2%, from 6.5 min to 5.25 min. For the E component, the schemes ISB-PW and ISB-AD perform better than ISB-OFF, and ISB-RW is worse than ISB-OFF, while ISB-WN has the worst performance. As

compared with ISB-WN, the convergence time of ISB-PW and ISB-AD can be improved by 40.4% from 23.5 min to 14.0 min, and 34.2% from 19.0 min to 12.5 min at 95% quantile and 68% quantile, respectively. Similar to N component, the improvements in the U component by considering ISB are slight, which can averagely reach 16.2%, and 5.8% at 95% quantile, and 68% quantile, respectively.

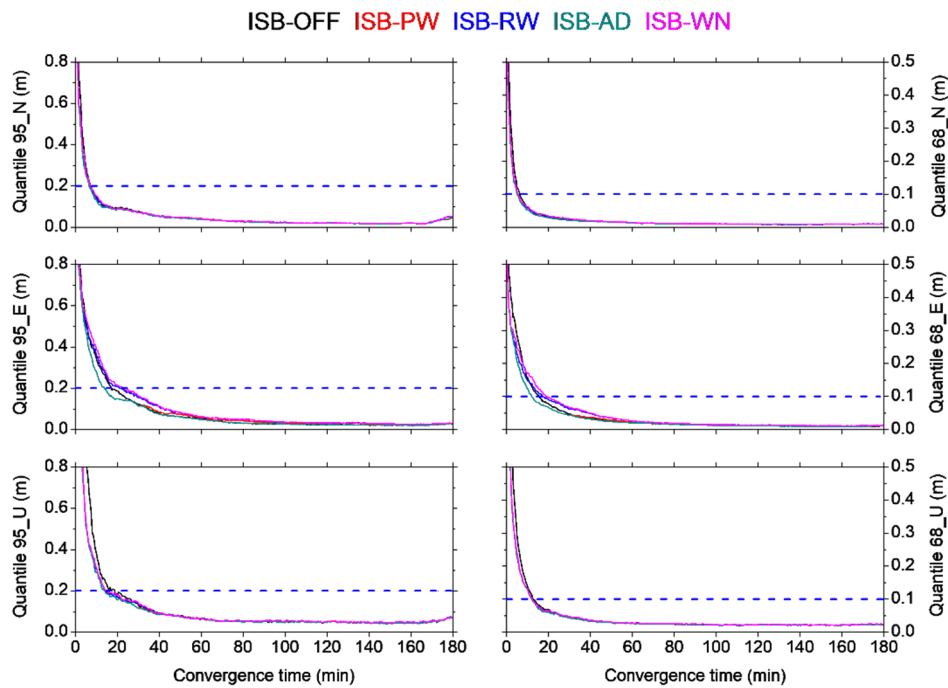


Figure 4.6 GPS/BDS combined kinematic PPP convergence performance in five different schemes using precise products from *WUM*.

From these two cases with *GBM* and *WUM* precise products, we can conclude that GPS/BDS combined PPP processing with orbit and clock products from different ACs can get a completely different result. The main reason is that during the multi-GNSS orbit and satellite clock estimation, different ISB resolution strategies (stochastic model) is applied in different ACs, and if the users utilize the same ISB strategies as the ACs (*GBM* and *WUM*) during the PPP performance, a better result can be attained. Accordingly, based on the tests in this study, we recommend users to consider the ISB parameter as a random walk processing, or a white

noise if the *GBM* products are applied; otherwise, when the *WUM* products are applied, it is better to consider the ISB as a piece-wise constant, or an arc-dependent constant.

Table 4.6 Convergence time and positioning accuracy of GPS/BDS combined kinematic PPP with the *WUM* products in five different schemes.

	Convergence time (95%/min)			Convergence time (68%/min)			Accuracy (95%/cm)			Accuracy (68%/cm)		
	N	E	U	N	E	U	N	E	U	N	E	U
OFF	7.5	17.5	17.0	6.5	15.5	13.0	4.9	6.1	7.6	2.0	2.7	3.2
PW	7.0	14.0	14.0	5.0	12.5	12.0	4.8	6.6	7.6	2.0	2.9	3.2
RW	7.0	21.0	14.5	5.5	17.5	12.5	5.0	7.0	7.8	2.1	3.3	3.3
AD	7.0	14.0	14.0	5.0	12.5	12.0	4.8	6.2	7.4	2.0	2.7	3.1
WN	7.0	23.5	14.5	5.5	19.0	12.5	5.2	6.8	8.0	2.2	3.3	3.3

4.4.3 Accuracy improvement during the convergence period

Since during the convergence period, the accuracy of GPS/GLONASS combined PPP can be improved with the consideration of the inter-frequency biases (IFB) (Shi et al. 2013). Therefore, the analysis of accuracy improvement in GPS/BDS fusion PPP during the initialization phase is performed as well.

Table 4.7 Positioning accuracy of GPS/BDS combined kinematic PPP during the convergence period (8min and 16min) in five different schemes with *GBM* precise products (unit: cm).

	8min (95%)			16min (95%)			8min (68%)			16min (68%)		
	N	E	U	N	E	U	N	E	U	N	E	U
OFF	71.4	78.4	191.8	76.1	94.7	178.7	49.3	57.9	106.1	35.6	45.5	76.4
PW	58.2	69.3	135.6	43.3	58.8	100.0	24.6	31.4	58.1	18.1	27.1	42.7
RW	58.7	71.2	135.9	42.9	53.1	99.0	24.3	30.6	57.4	17.6	23.7	41.5
AD	58.2	69.3	135.6	43.4	58.8	100.0	24.6	31.4	58.1	18.1	27.1	42.7
WN	60.5	69.9	137.1	43.8	54.3	99.2	24.6	31.1	57.5	17.8	24.3	41.5

Table 4.7 and Table 4.8 shows the statistics of the positioning accuracy during the convergence period. It can be seen from the tables that no matter which products applied if ignoring ISB, the accuracy in N, E, and U components is lower than other schemes considering the ISB during 8 min and 16 min convergence period both at 95% and 68% quantile. Accordingly, we can conclude that considering ISB also has a significant improvement in the PPP positioning accuracy during the convergence period. With *GBM* precise products, the average improved rate can reach to 40.1%, 35.4%, and 41.0% in N, E, and U components, respectively. While, for the *WUM* products, this rate can be achieved by 25.4%, 22.3%, and 33.4% in three components, respectively.

Table 4.8 Positioning accuracy of GPS/BDS combined kinematic PPP during the convergence period (8min and 16min) in five different schemes with *WUM* precise products (unit: cm).

	8min (95%)			16min (95%)			8min (68%)			16min (68%)		
	N	E	U	N	E	U	N	E	U	N	E	U
OFF	104.8	122.8	247.2	51.3	59.7	137.7	32.1	38.7	82.0	23.0	29.1	58.6
PW	59.2	68.7	136.9	42.0	52.0	97.6	25.3	30.5	57.0	18.2	22.9	41.0
RW	59.3	68.2	136.8	42.5	55.5	98.0	25.4	31.4	57.0	18.4	24.3	41.1
AD	59.2	68.7	136.9	42.0	52.0	97.6	25.3	30.5	57.0	18.2	22.9	41.0
WN	59.6	73.4	137.0	43.2	57.6	98.8	25.7	32.5	57.6	18.6	25.6	41.5

4.4.4 Comparison of estimated ISBs

The estimated ISB is the most direct factor to reflect which stochastic model is the optimal one for the PPP performance and how to select an ideal stochastic model for different precise products. Thus, the comparisons of the estimated ISBs from the schemes ISB-PW, ISB-RW, ISB-AD, and ISB-WN using *GBM* and *WUM* precise products are made. Figure 4.7 shows the estimated ISBs using the *GBM* products in static and kinematic modes. The first 3-hour ISB results on DOY 251, 2017 in the station STR1 are taken as an example.

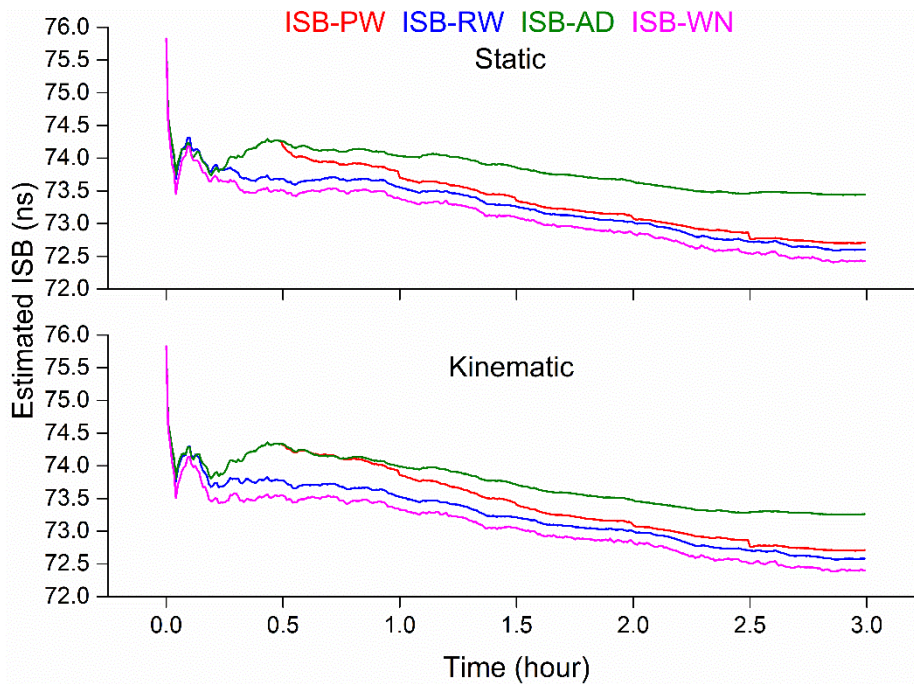


Figure 4.7 The estimated ISBs derived from the four different schemes with considering ISB using the *GBM* products. Different ISBs are shown in different colors. The top subfigure displays the results for the static mode, while the bottom on is the results for the kinematic mode

From Figure 4.7, we can see that the four estimated ISBs from the PPP performance with different stochastic models using *GBM* products have entirely different results. The ISBs in ISB-AD have the most significant values. The ISBs in ISB-PW are coincident with those in ISB-AD in the first 30 min, but they show different values in the following periods because ISB in ISB-PW was initialized every 30 min. The ISBs in ISB-RW and ISB-WN demonstrate the consistent trend but with a systematic difference, which will be absorbed by the ambiguity in the PPP solution. To deeply show the feature ISBs with different precise products, the PPP performance using the *WUM* products is also made. The estimated ISBs with the *WUM* product is shown in Figure 4.8.

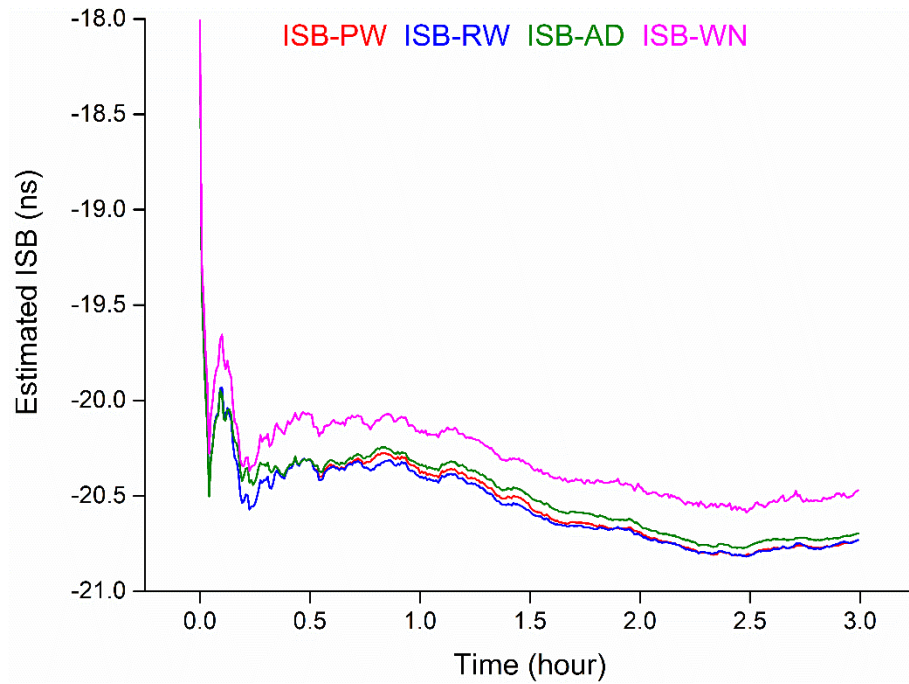


Figure 4.8 The estimated ISBs using the *WUM* products in the kinematic mode. Different ISBs derived from the different schemes with considering ISB are shown in different colors

It can be noticed from Figure 4.8 that fully different from the results in Figure 4.7, the ISBs in ISB-PW, ISB-RW, and ISB-AD have the same trend and very close values. A consistent trend is displayed between the ISB in ISB-WN and the other three ISBs, but the ISB in ISB-WN is rougher than others.

4.5 Summary

In order to study the effect of stochastic models for the ISB estimation and the ISB characteristic, five different ISB processing strategies are proposed. From the comparison of pseudorange observation residuals between five strategies, it can be seen that the ISB-OFF strategy has the most significant residuals, the other four schemes are similar. As compared with ISB-OFF, the PC residual RMS of ISB-PW, ISB-RW, ISB-AD, and ISB-WN can reduce by 21.3 m (95.9%) both in static mode and kinematic mode. In other words, it is quite mandatory to consider the impact of ISB parameter in multi-GNSS combined positioning.

Concerning the convergence time and positioning accuracy analysis, the cases with *GBM* and *WUM* precise products are carried out, respectively, to reveal the potential impact on ISB caused by the different solution strategies of analysis centers. The result of the *GBM* case shows that ISB-RW and ISB-WN strategies have similar processing accuracy and the best performance. While ISB-AD performs worst, even worse than the ISB-OFF, which is against the conclusion of pseudorange observation residuals results, the most probable reason may be the ISB during *GBM* precise product generation is not estimated as an arc-dependent constant. The consequence of *WUM* case is opposite, the schemes ISB-PW and ISB-AD perform best, and ISB-RW is worse than ISB-OFF, while ISB-WN has the worst performance, which indicates that the ISB processing strategies of *GBM* and *WUM* products are absolutely different. Therefore, it is recommended that regarding the ISB parameter as a random walk, or white noise if the *GBM* products are used, otherwise, when the *WUM* products are applied, it is better to consider the ISB as a piece-wise constant, or an arc-dependent constant. Accordingly, in the latter PPP processing, we will select the appropriate stochastic model according to the precise products from different ACs.

The test of accuracy improvement during the convergence period is performed as well. From the results, the conclusion can be attained that the same as after converged time, considering ISB or not also has a substantial impact on the PPP positioning accuracy during the convergence period.

5 Preprocessing of satellite clock product for ISB jumps detecting and repairing

5.1 Introduction

Through the precise modeling of ISB, the convergence time and accuracy of PPP with multiple systems can be improved by the a priori constraint of ISB prediction value (Jiang et al. 2017). Generally, the ISB is considered as stable and continuity day by day. However, in this study, we find that ISB difference has a strong correlation with the satellite clock offsets in adjacent days. Besides, the jumps existed in the precise clock product will destroy the ISB continuity. Nevertheless, a smooth and continuous ISB series is required before ISB modeling, since the ISB jumps will significantly impact the fitting accuracy of the model. Therefore, a preprocessing method for detecting and repairing jumps in the satellite clock products will be utilized to improve the ISB continuity. With the clock product preprocessing, the ISB jumps can be effectively repaired, and its continuity will be improved remarkably, which means preprocessing of the precise clock is an appropriate way to detect and repair the ISB jumps.

In this chapter, we mainly focus on the detecting and repairing of ISB jumps with the preprocessing of precise clock product. It starts with the introduction of experimental data and processing strategies in Section 5.2. Then, Section 5.3 analyzes and studies the relationship between ISB and satellite clock, and clock preprocessing for ISB jumps detecting and repairing. Ultimately, the summary and conclusions of this chapter are made in Section 5.4.

5.2 Experimental data and processing strategies

Herein, GPS and BDS observations from 9 IGS MGEX stations (CUT0, JFNG, SIN1, HKOH, HKSL, HKWS, MAJU, NAUR, NNOR) during August 2015 are processed in PPP mode for ISB estimation. The 14 BDS-2 satellites and signals of B1 and B2 are used in this experiment. The

distribution of the stations is shown in Figure 5.1. These nine stations are chosen based on the report of the current distribution of the constellation of Beidou satellites (Yang et al. 2014). All these nine stations can simultaneously observe more than four BDS satellites, and three different types of receivers are installed among these stations. The details regarding the receivers at these stations are listed in Table 5.1.

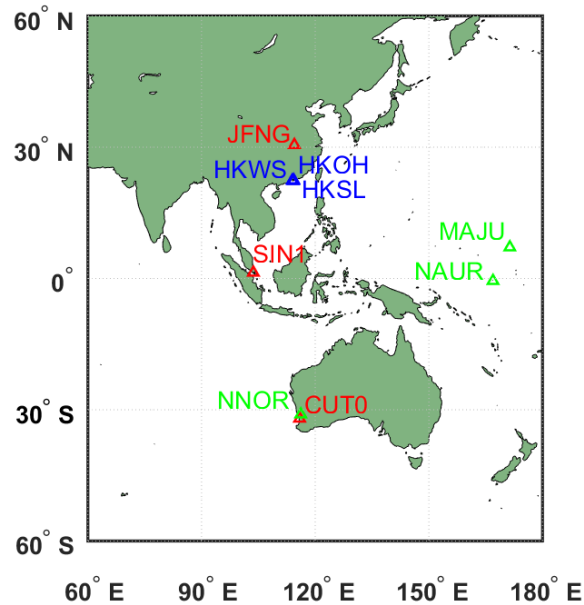


Figure 5.1 Geographic distribution of GPS/BDS Stations, three stations with “TRIMBLE” receivers are in red, those installed with “LEICA” receivers are in blue, the rest three stations are shown in green with the receiver type of “SEPT”.

To analyze the characteristics of ISB between GPS and BDS systems, we process these nine stations from the MGEX network with the mode of PPP, and the MGEX precise orbit and clock products from GFZ (*GBM*) were used. The ISB between GPS and BDS was estimated as a piece-wise parameter (5 min interval) together with other unknowns, for instance, coordinates and receiver clock offset. The ionosphere-free combined observations are applied in data processing. The elevation cutoff angle is set to 7°. The zenith wet delays are estimated as a random walk noise.

Table 5.1 Station ID, receiver types, firmware version, and location at 9 stations.

Station ID	Receiver type/firmware version	Location
CUT0	TRIMBLE NETR9/5.03	32.004S, 115.895E
JFNG	TRIMBLE NETR9/5.01	30.516N, 114.491E
SIN1	TRIMBLE NETR9/5.01	1.343N, 103.679E
HKOH	LEICA GRX1200+GNSS/6.404	22.248N, 114.229E
HKSL	LEICA GRX1200+GNSS/6.404	22.372N, 113.928E
HKWS	LEICA GRX1200+GNSS/6.404	22.434N, 114.335E
MAJU	SEPT PolaRx4TR/2.9.0Patch1	7.119N, 171.365E
NAUR	SEPT PolaRx4TR/2.9.0Patch1	0.552S, 166.926E
NNOR	SEPT PolaRx4/2.9.0	31.049S, 116.193E

5.3 The relationship between ISB and satellite clock and clock preprocessing

Figure 5.2 shows the estimated GPS/BDS ISB series for the nine stations. Three stations are equipped with the receiver type of “TRIMBLE NETR9” (CUT0, JFNG, SIN1), three are installed with the type of “LEICA GRX1200+GNSS” (HKOH, HKSL, HKWS), and the residual three are equipped with the type of “SEPT PolaRx4/4TR” (MAJU, NAUR, NNOR). They are displayed with different colors and symbols in Figure 5.2. As evident from the figure, the ISB series for the same type of receiver are similar, indicating that the stations with the same kind of receiver have similar ISBs. The main reason for this phenomenon is that the major component of ISB between two satellite systems comes from the hardware delay, which is theoretically similar for the same receiver type. Moreover, in the red box from epoch 4800 to 6400, two jumps can be observed, and they are more evident in the enlarged view. These two gaps, which appear at the border between the day-pairs August 17-18 and 19-20, are caused mainly by the irregular variations in the satellite clock, including satellite clock phase modulation (PM) which can be regarded as the deviation between the true phase and the initial phase, frequency modulation (FM), switch of the reference clock, and outliers. For the PPP processing herein,

we substitute the satellite clock as a known into the processing equation, thus, if the satellite clock experiences a jump, the estimated ISB will vary correspondingly because of the linear dependence between them.

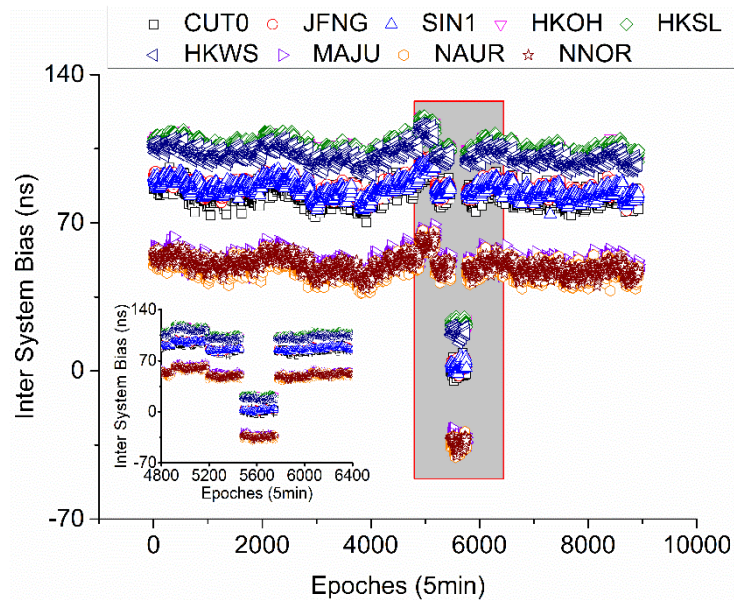


Figure 5.2 Estimated ISB of stations CUT0, JFNG, SIN1, HKOH, HKSL, HKWS, MAJU, NAUR, and NNOR. The left bottom sub-figure is the enlarged view of ISB during the epochs 4800-6400, i.e., August 17-22, 2015

5.3.1 The correlation verification between ISB and satellite clock in the time domain

To verify the linear dependence between the ISB and satellite clock offsets, we will make an analysis on the correlation coefficients between them in the time domain. In this study, we employ BDS precise clock products from MGEX analysis center GFZ (*GBM* products) during August 2015.

Figure 5.3 presents the time series of the satellite clock offsets from *GBM* products for BDS satellite C01 through C14, excluding C13. As displayed in the figure, the clock offsets of BDS satellite frequently appear data interrupt (DI) and large data jumps, which can be detected easily in the time domain. Here, large clock jumps are termed as phase modulation

(PM), which occur more frequently in geostationary orbit (GEO) satellites (C01-C05). The possible reason for this may be that GEO satellites perform more orbital maneuvers. Since the magnitude of the variation of the PM in the satellite clock is large, it can be detected and marked with ease. The corresponding times of DI and PM occurrence are summarized in c.

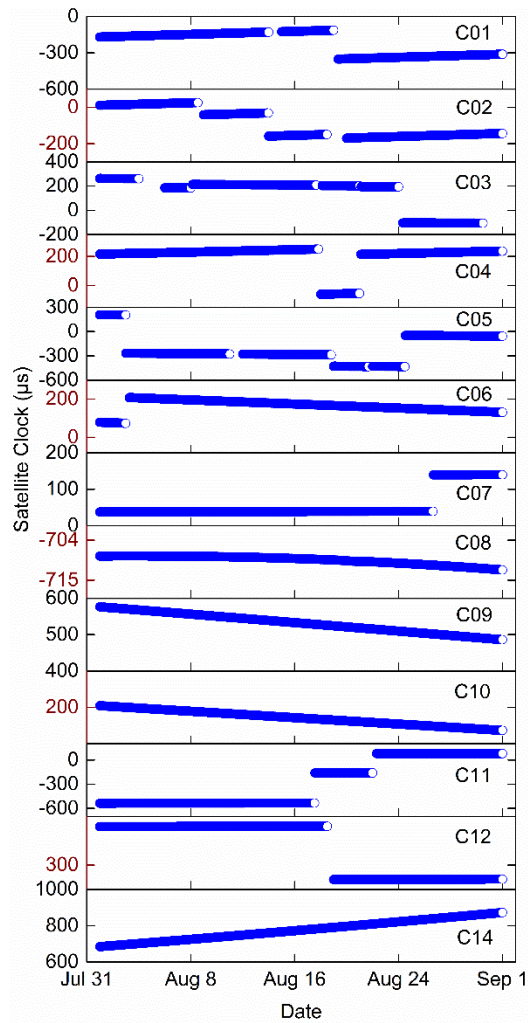


Figure 5.3 Satellite clock offsets of BDS in the time domain during August 2015, in the right part of each subfigure is the satellite ID, from C01 to C14 without C13, the vertical axis is colored in black and wine intervals for a clearer view.

Table 5.2 The time Statistics of data interrupt (DI) and phase modulation (PM) of BDS satellites in August 2015, in the table we only list the day in August without the month

number to simplify the space, satellites C08, C09, C10, C14 have no DI and PM, so they are not listed in the table.

Satellite Number	Data interrupt(DI) periods		Phase modulation(PM) points in the time domain	
	Epochs	Day/Time (Aug., 2015)	Epoch	Day/Time(Aug., 2015)
C01	3745-4032	14/00:00-14/23:55	5285	19/08:20
	5185-5284	19/00:00-19/08:15		
C02	2176-2304	8/13:15-8/23:55	2305	9/00:00
	3740-3745	13/23:35-14/00:00	3746	14/00:05
	5037-5472	18/11:40-19/23:55	5473	20/00:00
	865-1440	4/00:00-5/23:55	1441	6/00:00
C03	2017-2056	8/00:00-8/03:15	2057	8/03:20
	4800-4931	17/15:55-18/02:50	4932	18/02:55
	5761-5797	21/00:00-21/03:00	5798	21/03:05
	6625-6717	24/00:00-24/07:40	6718	24/07:45
	8498-8928	30/12:05-31/23:55		
	4850-4896	17/20:05-17/23:55	4897	18/00:00
C04	5761-5790	21/00:00-21/02:25	5791	21/02:30
	575-578	2/23:50-3/00:05		
C05	2050-2054	8/02:45-8/03:05	579	3/00:10
	2881-3168	11/00:00-11/23:55	5185	19/00:00
	5133-5184	18/19:40-18/23:55	6049	22/00:00
	5962-6048	21/16:45-21/23:55	6774	24/12:25
	6765-6773	24/11:40-24/12:20		
	8415-8425	30/05:10-30/06:00		
C06	577-653	3/00:00-3/06:20	654	3/06:25
C07	7385-7396	26/15:20-26/16:15	7397	26/16:20
C11	4765-4771	17/13:00-17/13:30		
	5074-5078	18/14:45-18/15:05	4772	17/13:35
	5206-5210	19/01:45-19/02:05	6138	22/07:25
	6049-6137	22/00:00-22/07:20		

	6442-6447	23/08:45-23/09:10		
C12	4897-4900	18/00:00-18/00:15	5185	19/00:00
	5047-5184	18/12:30-18/23:55		

As evident from Figure 5.2, together with Figure 5.3, and Table 5.2, the times when ISB jumps happen in Figure 5.2 are not simultaneous with the times of PM occurrence in Figure 5.3 and Table 5.2. Accordingly, it can be concluded that clock PM is not the reason for causing the ISB discontinuity.

A numerical verification is performed to further reveal the linear dependence between the ISB and satellite clock offsets. Here, we take the time period from August 17 to 21 as an example, indicating that tests will be performed on the four day-pairs August 17-18, 18-19, 19-20, and 20-21, 2015. At first, we calculate the residual of satellite clock offsets in a day-pair, denoted as Δt , by differencing the predicted satellite clock Pt from polynomial fitting based on the satellite clocks from the last ten epochs on the first day and the real satellite clock Rt in the first epoch of the second day. This process can be denoted as follows:

$$\begin{aligned}
 Pt_{fe} &= F(Rt_1, Rt_2, \dots, Rt_{10}) \\
 \Delta t_{fe} &= Rt_{fe} - Pt_{fe}
 \end{aligned}
 \tag{5.1}$$

where, $F(Rt_1, Rt_2, \dots, Rt_{10})$ is the polynomial fitting based on the satellite clock offsets of last ten epochs on the first day. Therefore, Pt can be derived through extrapolation with $F(Rt_1, Rt_2, \dots, Rt_{10})$. fe demonstrate the first epoch on the second day. Then, the ISB difference between adjacent days can be derived as hereunder:

$$\begin{aligned}
 \Delta ISB_i &= ISBmean_i - ISBmean_{i-1} \\
 ISBmean &= MEAN(ISB_1, ISB_2, \dots, ISB_n)
 \end{aligned}
 \tag{5.2}$$

where the subscripts i and $i-1$ indicate adjacent days that constitute a day-pair; ISB is the ISB value at one epoch with n ranging from 1 to 288. ΔISB means the ISB difference between first and second day; $ISBmean$ denotes the mean ISB value on one day.

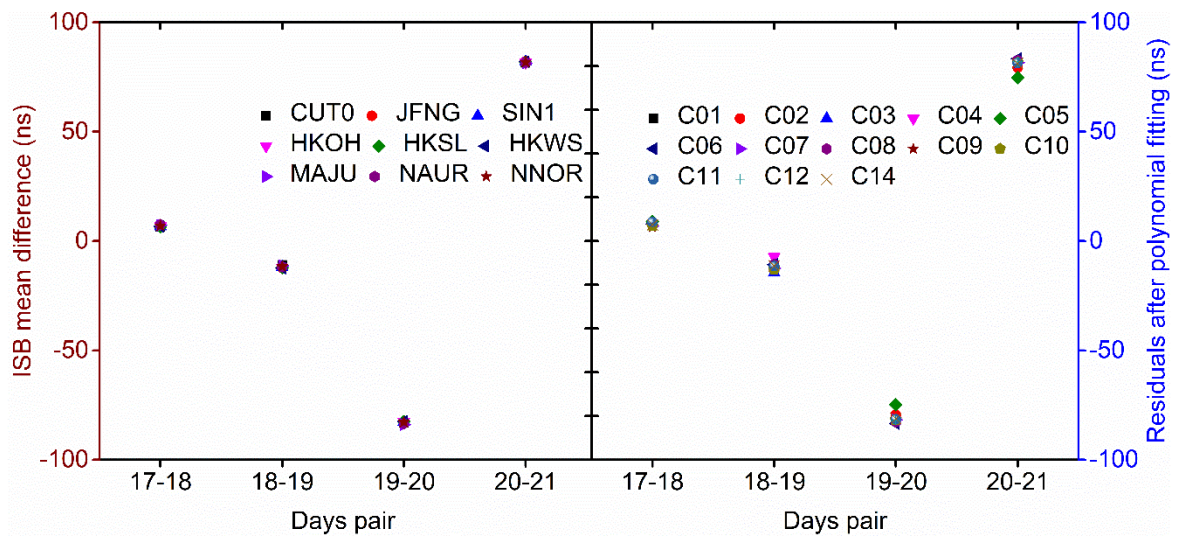


Figure 5.4 ISB differences and satellite clock residuals in adjacent days-pairs 17-18, 18-19, 19-20, 20-21, the left subfigure with wine color vertical axis is the ISB differences, and the right one with a blue color vertical axis is the satellite clock offset residual.

The ISB differences and satellite clock offset residuals in day-pairs August 17-18, 18-19, 19-20, and 20-21, 2015 are displayed in Figure 5.4, from which we can see that the ISB differences in four day-pairs at nine stations exhibit different magnitudes, the most significant variations appear in the day-pairs 19-20 and 20-21, suggesting that the satellite clock offset experienced a large jump on August 20, 2015. Actually, this jump can be attributed to the switch of the reference clock in the *GBM* precise clock product, which can be verified from the comments in the headers of the precise clock files. In each day-pair, the magnitudes of the ISB differences among all nine stations are quite close. Furthermore, the satellite clock offsets exhibit the same phenomenon as the ISB difference, that is, the residual level of the clock offset for each satellite is similar.

Table 5.3 ISB differences statistics in 9 stations at the days-pairs of 17-18, 18-19, 19-20, 20-21 (unit: ns).

Days-pair	CUT0	JFNG	SIN1	HKOH	HKSL	HKWS	MAJU	NAUR	NNOR
17-18	6.34	6.85	6.67	6.81	6.58	6.75	7.29	7.49	6.98
18-19	-10.88	-12.20	-11.81	-12.09	-12.12	-12.34	-11.24	-11.68	-11.64
19-20	-83.09	-82.80	-82.72	-82.66	-82.52	-82.42	-83.89	-83.43	-82.81
20-21	81.47	82.25	82.06	81.61	81.90	82.09	81.33	81.66	81.84

Table 5.4 Satellite clock offset residuals statistics at the days-pairs of 17-18, 18-19, 19-20, 20-21 for BDS satellites (unit: ns).

Days-pair	C01	C02	C03	C04	C05	C06	C07
17-18	7.37				9.02	7.92	7.03
18-19			-14.48	-7.17		-10.69	-12.45
19-20	-80.95	-79.38			-74.81	-83.41	-81.66
20-21	80.95	79.38			74.81	83.41	81.66

Days-pair	C08	C09	C10	C11	C12	C14
17-18	7.83	6.36	6.97	8.65		7.40
18-19	-10.56	-12.30	-12.85	-11.41		-11.23
19-20	-82.61	-81.46	-81.68	-81.47	-81.98	-81.15
20-21	82.61	81.46	81.68	81.47	81.98	81.15

Table 5.3 shows the statistics of the ISB differences among the nine stations, while Table 5.4 denotes the statistics of the satellite clock offset residuals. There are some blank entries in Table 5.4, which means there are no satellite clock offset residuals between these two adjacent days caused by a DI of satellite clock. A comparison of these two tables shows that the ISB differences at each station are consistent with the satellite clock residuals at each satellite among all four day-pairs. ISB jumps appear when satellite clock offset jumps occur, which means that the ISBs correlate with the satellite clock offsets. In the following discussion, the corresponding correlation coefficients will be analyzed.

The correlation coefficients can be employed as an index of the degree of correlation between two parameters. From Table 5.3 and Table 5.4, we can derive the correlation coefficients between the ISB difference and satellite clock offset residuals between each station and each satellite; the statistics are shown in Table 5.5. Since some satellites lack residuals, the correlation analysis is performed only between the satellites with residual data and the stations. From the table, it is evident that the correlation coefficient between each pair of ISB difference and satellite clock offset residual is close to 1, indicating that they have a strong (nearly positive) correlation. Based on this finding, the motivation of preprocessing on the satellite clock products is attained, which is for the purpose of improving the ISB continuity. Therefore, in the following sections, we will propose a preprocessing method on the satellite clock products for detecting and repairing the ISB jumps.

Table 5.5 Correlation coefficients between ISB differences and satellite clock offset residuals, the values in the table are listed as the increments to 1, the smaller the value, the closer it is to 1 (unit: 10^{-5}).

Correlation coefficient	C06	C07	C08	C09	C10	C11	Mean
CUT0	-2	-16	-2	-13	-22	-17	-12
JFNG	-5	-1	-5	-1	-3	-7	-4
SIN1	-3	-3	-3	-2	-6	-8	-4
HKOH	-3	-2	-3	-3	-4	-5	-3
HKSL	-5	-2	-5	-1	-4	-8	-4
HKWS	-7	-1	-7	-1	-2	-8	-4
MAJU	-2	-18	-2	-20	-23	-8	-12
NAUR	-1	-9	-1	-12	-12	-2	-6
NNOR	-1	-5	-1	-5	-8	-6	-4

5.3.2 Convert the satellite clock data (time domain) into the frequency domain

It is easy to detect large clock jumps caused by sizable PMs directly from satellite clock offsets in the time domain from Figure 5.3. However, as mentioned above, such clock jumps do not affect the ISB continuity. Therefore, the kind of clock jump that impacts the ISB continuity needs to be further analyzed and studied. Additionally, some small clock jumps, caused by weaker PMs, clock day boundaries, or reference clock substitutions, may be obscured within satellite clock offset series. Since the satellite clock in the frequency domain is more sensitive to detect the clock jumps, especially smaller clock jumps, than that in the time domain. We will transform the satellite clock from the time domain into the frequency domain.

To attain a successful solution, we first convert the clock offset time series, except for the DIs and vast PM epochs, into clock frequency data (CFD) as hereunder:

$$y_i = \frac{x_{i+1} - x_i}{\tau} \quad (5.3)$$

where x_{i+1} and x_i are the clock offset data at two adjacent epochs $i+1$ and i , τ denotes the interval, which is set to 5 min; and y_i represents the clock data in the frequency domain.

Figure 5.5 shows the series of CFD series during August 2015. Except for the DI periods, each satellite has two extrema with identical magnitudes at epochs 5472 and 5760. The corresponding time is the first epoch of August 20 and 21, 2015, respectively, which is synchronous with the time points of the most massive ISB jumps. That is to say, these ISB jumps are caused by the extrema within the CFD. In addition, other smaller extrema within the CFD can also impact the ISB continuity, which will be studied in the following discussion. To some extent, these ISB jumps can be regarded as the differences in the ISB between two adjacent epochs, while extrema in the CFD denote the most significant clock offset residuals. Therefore, these findings further support the conclusion of the strong correlation between ISB differences and satellite clock offset residuals.

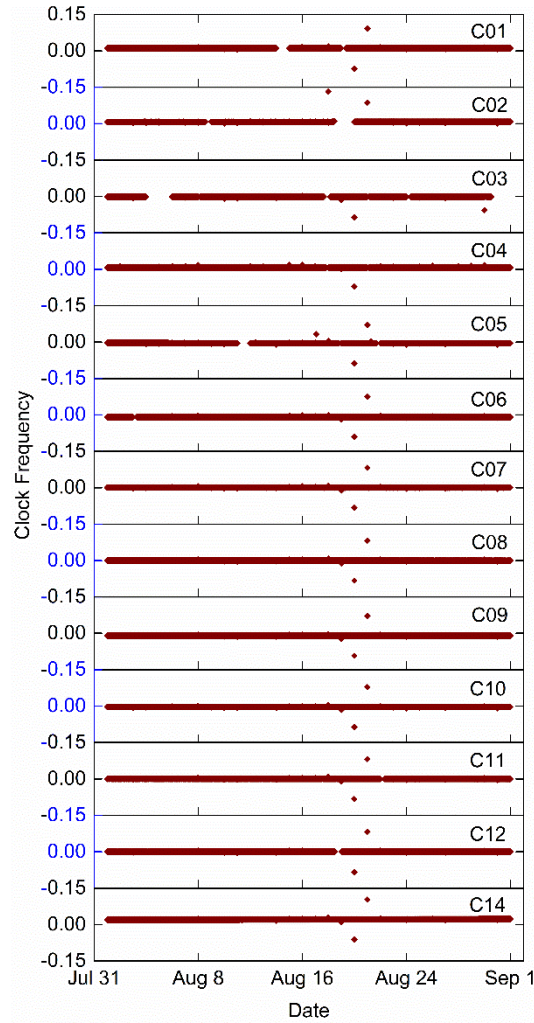


Figure 5.5 Clock frequency data of BDS satellites during August 2015, the satellite ID is included in the top right corner of each panel, from C01 to C14 excluding C13, the vertical axis is colored in black and blue intervals for a clearer view.

5.3.3 Detection of small extrema of CFD

In comparison with the mean value, the median value can better represent the characteristics of the majority data, which means it has a greater ability to avoid the influences of outliers. Therefore, a median filter-based robust estimation can improve the robustness of the detection of CFD extrema (Yang et al. 2001). Considering this advantage, a method based on the median filter is employed to detect the small ISB jumps that cannot be observed directly from CFD series. According to the median principle, the mean square error of unit weight (σ_0) is

defined as the normalized median of absolute deviation between CFD and the median of CFD, which is expressed as hereunder:

$$\begin{aligned}\sigma_0 &= \text{median}\left\{\frac{|v_i|}{0.6745}\right\} \\ v_i &= y_i - m \\ m &= \text{median}\{y_i\}\end{aligned}\tag{5.4}$$

where y_i indicates CFD at epoch i , m represents the median of y_i , v_i is the deviation between y_i and m , σ_0 denotes the mean square error of unit weight. Here, we regard $n \cdot \sigma_0$ as a threshold value. If the equation $|v_i| \geq n \cdot \sigma_0$ is satisfied, y_i is regarded as an extremum of CFD; otherwise, y_i represents a regular CFD point. n can be variable and is determined by an empirical model. Here, it is set to 10.

5.3.4 Classification of extrema of CFD and clock preprocessing

As mentioned above, the clock jumps are attributable to several reasons, and different clock preprocessing strategies need to be applied for each reason. After all the CFD extrema are successfully detected, these reasons need to be classified. Some clock jumps may be caused by small PMs that are not detected within the series of satellite clock offsets in the time domain. For this kind of extrema, we do not employ preprocessing since PMs do not affect the ISB continuity. Other clock jumps probably originate from clock day boundaries derived from the daily solution of precise clock products. The best resolution for this type of extremum is to estimate an integral satellite clock offset series over a more extended period (e.g., one week, or one month). However, in this study, we do not re-estimate the satellite clock offsets; rather, we apply two different strategies for this kind of extremum. If the clock jump exceeds the threshold value, we utilize polynomial fitting based on previous data to predict the new satellite clock offset and replace the original satellite clock offset to generate a new clock product; otherwise, no processing will be employed, and the original clock product is retained. Residual extrema originate from the switch of the reference clock. We can easily verify this from the

comments in the headers of the precise clock product files, which show the station name of the reference clock. The polynomial fitting method is also applied to resolve this type of extremum. The procedures of all above steps are summarized in Figure 5.6.

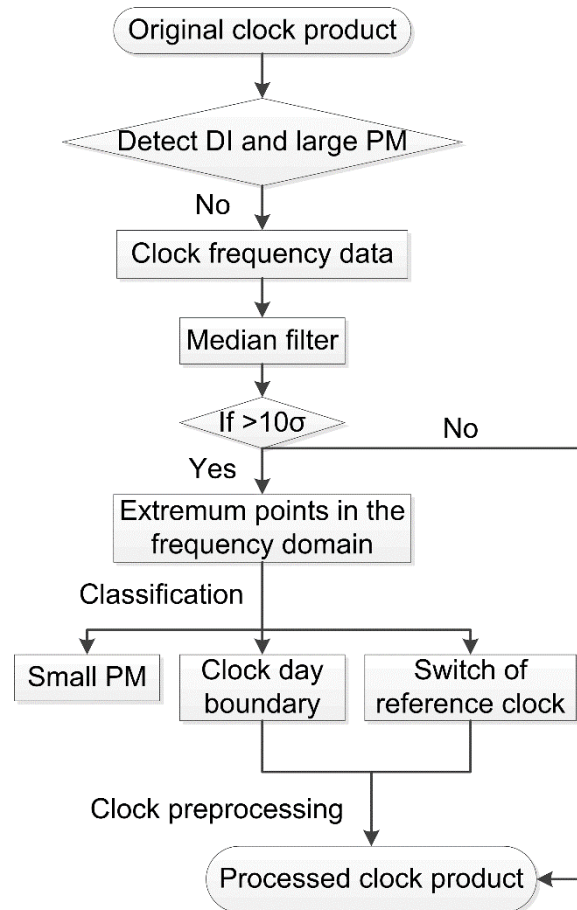


Figure 5.6 Flow chart of satellite clock preprocessing

The classified types of extrema in the CFD are shown in Figure 5.7, and their corresponding time statistics are listed in Table 5.6. From Figure 5.7 and Table 5.6, we can see that the extrema in CFD are caused mainly by three different reasons, i.e., clock day boundaries derived from the daily solution strategy employed for precise clock products, small PMs that are not observed directly in clock offset time domain series, and switches of the reference clocks. It should be noted that the extrema, i.e., jumps, will appear for each satellite if the reference clock is altered. Usually, the magnitude of this kind of extremum is considerable. In this case, we need to apply a method to maintain the continuity of the clock offset series to

obtain a smooth ISB. Thus, a new satellite clock product derived from predictions acquired through polynomial fitting is used. We consider that a clock day boundary under a predefined threshold value (3σ) will not destroy the clock continuity. Nevertheless, when the clock day boundary exceeds the threshold value, we employ the same processing procedure as that used for switches of reference clocks to replace the original clock with the prediction clock. Due to the superior ability of the median filter to detect CFD extrema, we can detect the smaller PMs that are hidden within the satellite clock offsets in the time domain. These small clock PMs do not affect the continuity of the estimated ISB. However, in the areas of satellite clock modeling and prediction, a continuous clock series is required, so even these smaller PMs must be corrected.

Table 5.6 Time statistics of three different types of extremum points appeared in BDS clock frequency data. If the extremum point is detected at the time of first epoch of one day, only the day in Aug. 2015 is listed. The blank means there is no extremum point detected for this satellite.

Satellite Number	Reasons/Corresponding day and time in Aug. 2015		
	Clock day boundary	Small PM	Switch of reference clock
C01	18		20; 21
C02	18		21
C03	30		20
C04	16; 30		20
C05	18	17/01h45m	20; 21
C06	19		20; 21
C07	18; 19		20; 21
C08			20; 21
C09	18; 19		20; 21
C10	18; 19		20; 21
C11	18; 19		20; 21
C12			20; 21
C14			20; 21

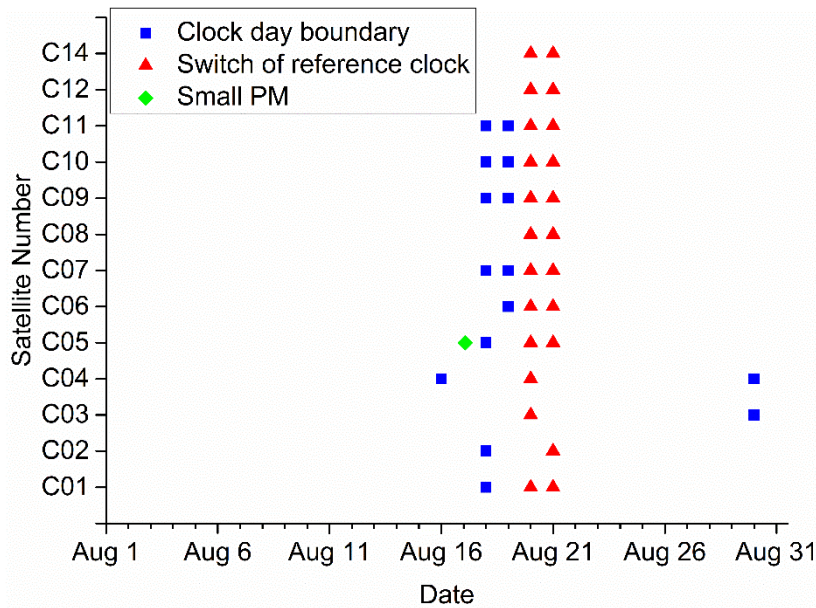


Figure 5.7 Clock frequency data extremum points caused by three different reasons, i.e., clock day boundary, switch of the reference clock, and small PM with diverse colors and symbols, during August 2015.

After the satellite clock data are preprocessed, we attain a new and smooth clock product. Then, we re-estimate the ISB with this preprocessed satellite clock product, and the results are shown in Figure 5.8. In comparison with the ISB derived from the original clock products in Figure 5.2, the re-estimated ISB series derived from the preprocessed precise clock products contain no jumps and is much smoother and more continuous.

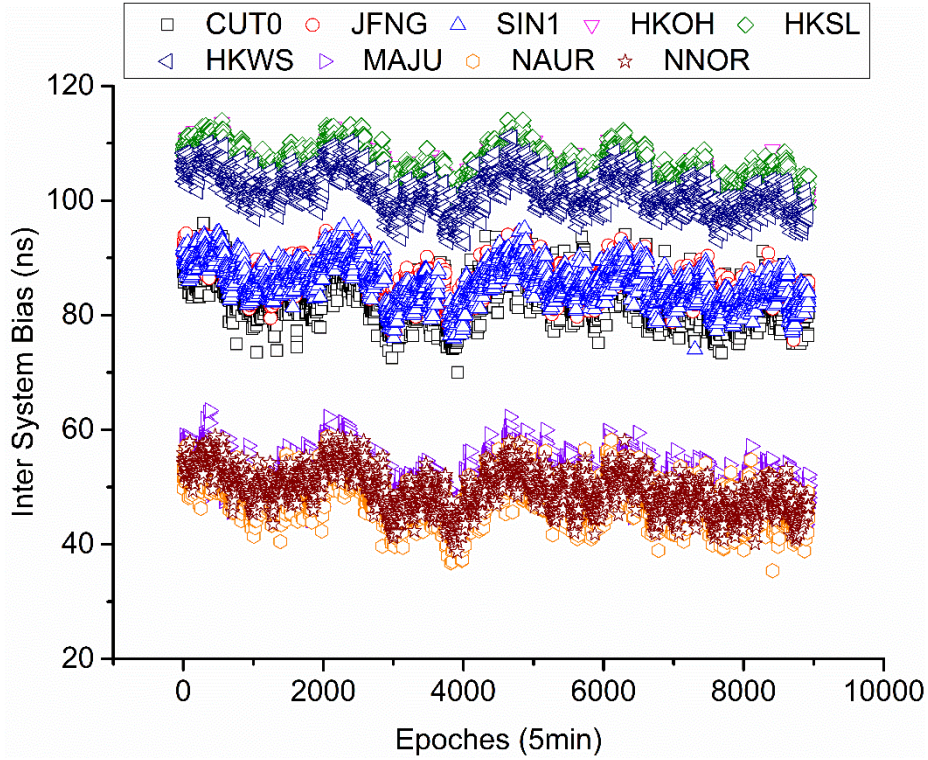


Figure 5.8 Re-estimated ISB with the processed satellite clock product of stations CUT0, JFNG, SIN1, HKOH, HKSL, HKWS, MAJU, NAUR, and NNOR.

5.3.5 Improvement of continuity of ISB

To verify that the ISB continuity improved as a result of the preprocessing on the clock products, we apply a statistical hypothesis method to express the ISB continuity. The test statistics can be formed as hereunder:

$$T_N = \frac{|\bar{x}_a - \bar{x}_b|}{\sqrt{\sigma_a^2 + \sigma_b^2}} \sim N(0,1) \quad (5.5)$$

where T_N indicates continuity factor. σ_a^2 and σ_b^2 denote the variance of the day a and b , correspondingly. \bar{x}_a and \bar{x}_b are the weighted mean value of ISB at day a and b , respectively; and can be derived through the following equation:

$$\bar{x} = \frac{\sum_{i=1}^n x_i / \sigma_i^2}{\sum_{i=1}^n 1 / \sigma_i^2} \quad (5.6)$$

where x_i , σ_i^2 are the estimated ISB and its variance, respectively, and \bar{x} denotes the weighted mean value of ISB per day.

In general, if T_N follows a standard normal distribution and has a significance level of α , the critical value of T_N can be termed as $N_\alpha(0,1)$. Here, the following criterion is used: when $T_N < N_\alpha(0,1)$, there is no significant difference in the ISB between two days, which means that the ISB is continuous; otherwise, the ISB changes substantially between two adjacent days. As T_N is the ISB continuity index, the ISB between adjacent days is smoother when the value of T_N is smaller.

As mentioned before, the precise clock products on August 18 and 20 have been preprocessed. Therefore, we select the period during August 17-21 as an example to analyze the improvement in the ISB continuity. Figure 5.9 shows the original ISB series of stations CUT0, JFNG, SIN1, HKOH, HKSL, HKWS, MAJU, NAUR, and NNOR in the top subgraph; the mean values and their standard deviations of stations CUT0, HKOH, MAJU are displayed in the bottom subfigure as an example. From the top subfigure, we can see that the ISB series are discontinuous on August 18 and 20; this finding can also be verified from the mean daily ISB values in the bottom subfigure. The ISB series derived from the preprocessed precise clock products and the mean daily values of the processed ISB are presented in Figure 5.10, from which it is evident that the discontinuity of ISB between day-pairs can be eliminated with the clock preprocessing.

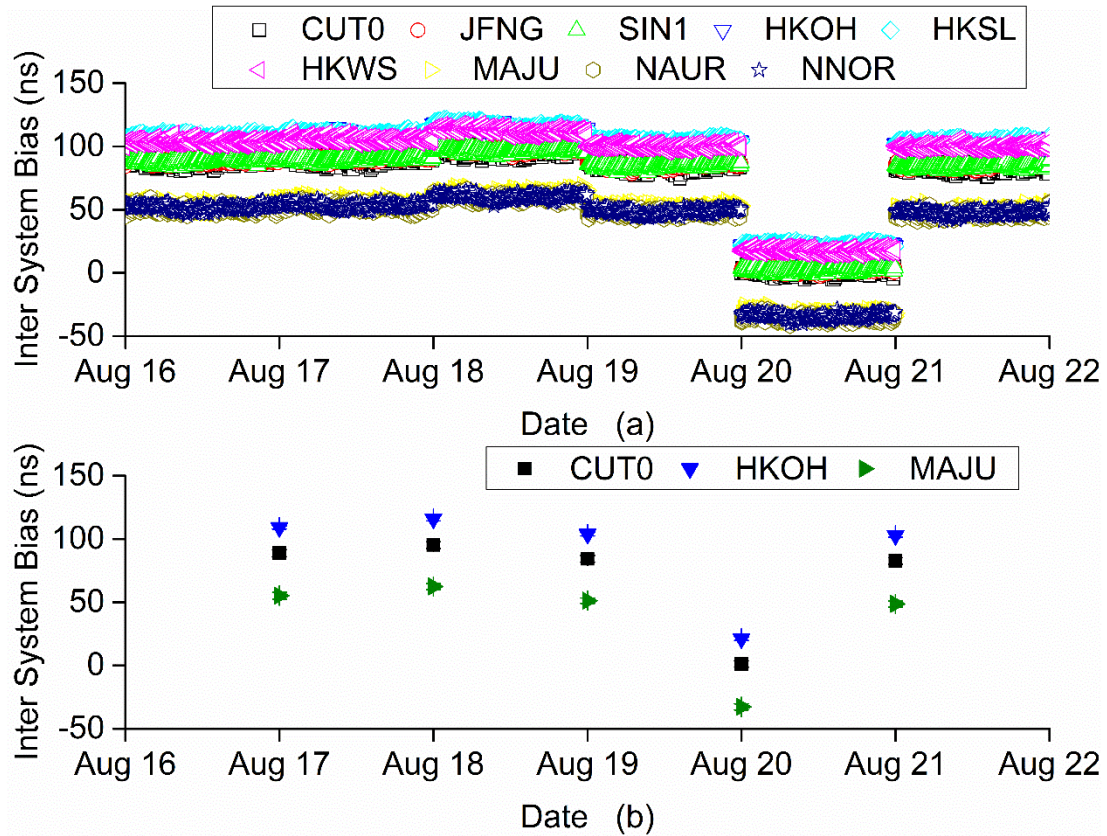


Figure 5.9 Subfigure (a) are the original ISB series of stations CUT0, JFNG, SIN1, HKOH, HKSL, HKWS, MAJU, NAUR, and NNOR; mean value and its standard deviation of stations CUT0, HKOH, MAJU from August 17 to 21 are shown in subfigure (b).

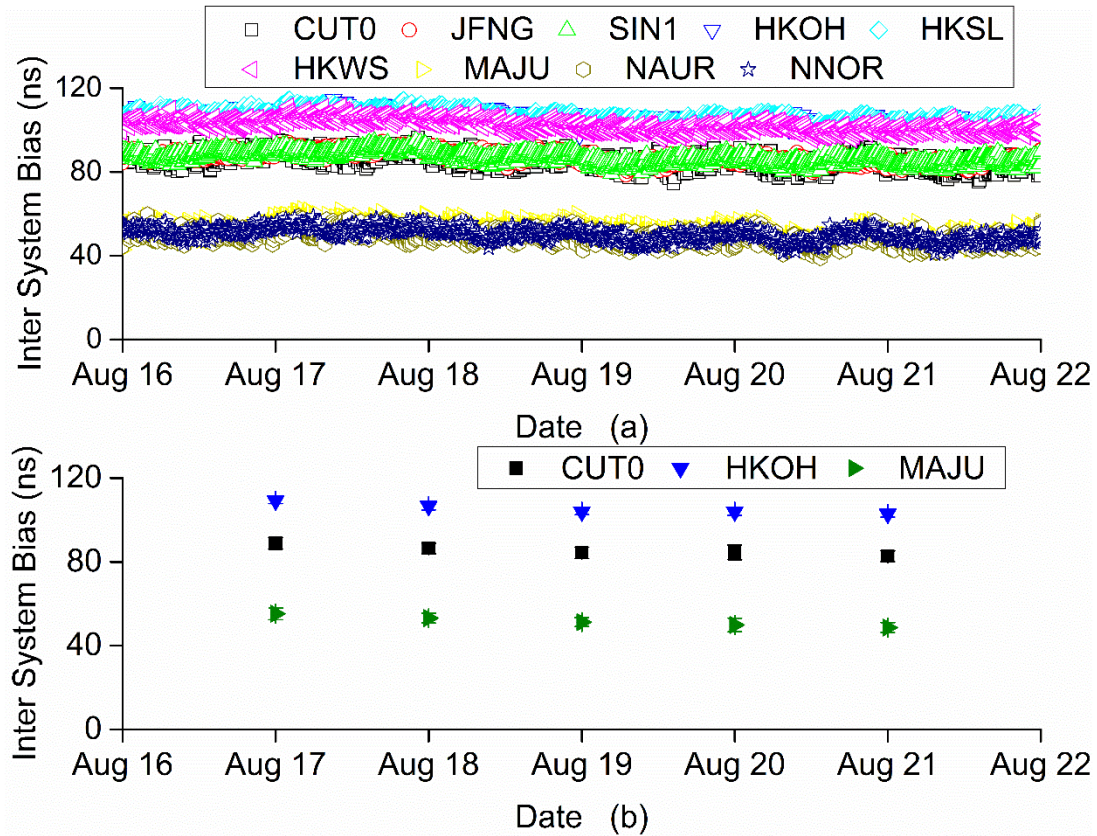


Figure 5.10 ISB series derived from the processed precise clock product of stations CUT0, JFNG, SIN1, HKOH, HKSL, HKWS, MAJU, NAUR, and NNOR are illustrated in subfigure (a); subfigure (b) is the mean value and its standard deviation of stations CUT0, HKOH, MAJU from August 17 to 21.

We establish the solution with the original clock product as scheme (a), and we assign the performance using the preprocessed clock product as scheme (b). The continuity factors of the two schemes are calculated through Equation (5.5). Additionally, the critical value of the standard normal distribution with a significance level of 0.01 is calculated as 2.327, which is shown with an orange line in Figure 5.11.

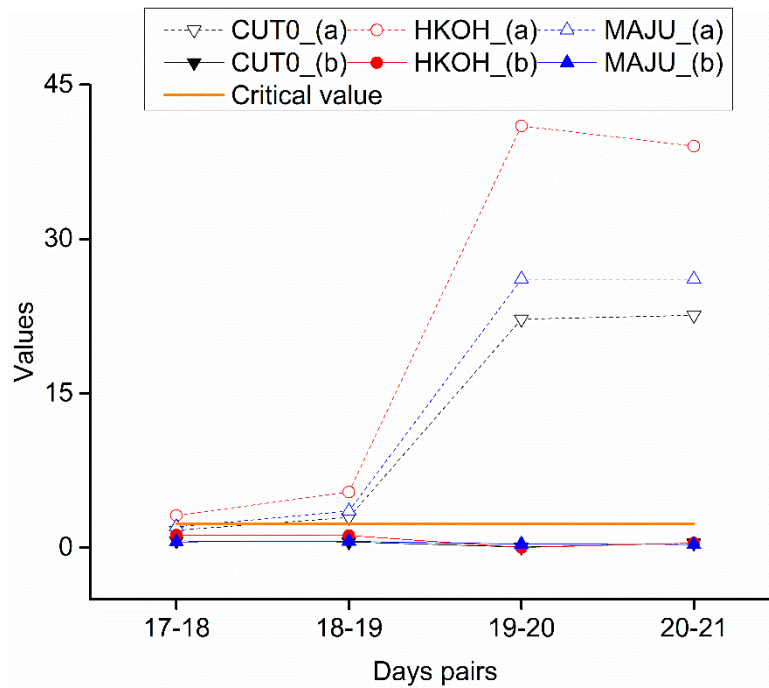


Figure 5.11 Continuity factor in two schemes ((a) is scheme (a), (b) means scheme (b)) of stations CUT0, HKOH, MAJU with different symbols, and the orange line denotes the critical value of standard normal distribution with a significance level of 0.01.

If the continuity factor is lower than the critical value, we consider the ISB to be continuous and stable over adjacent days. The continuity factors using scheme (a) are nearly all higher than the critical value, indicating that the ISBs between adjacent days during August 17-21 are discontinuous. In contrast, the continuity factors in scheme (b) are all below the line of critical value; this finding suggests that the stability of ISB between two days can be improved with the satellite clock product preprocessing. The continuity factors statistics are listed in Table 5.7, where more details can be observed. Clearly, the same conclusion can be derived that with the method of scheme (b), the continuity of ISBs between adjacent days can be obviously improved. The improvement rates are 62.4%, 79.5%, 99.6%, 99.0% at day-pairs of August 17-18, 18-19, 19-20, 20-21, correspondingly. In summary, with the preprocessing on the satellite clock products, the ISB continuity can be greatly improved.

Table 5.7 Continuity statistics of ISB in different days-pairs (August 17-28, 18-19, 19-20, 20-21), two different continuity factors derived from two diverse schemes are listed. Here scheme (a) is the original ISB series without any processing, ISB series with clock product preprocessing is obtained in the scheme (b). The Continuity factors got from these two kinds of ISB are listed as follows.

Days-pairs	17-18		18-19		19-20		20-21	
Station ID	(a)	(b)	(a)	(b)	(a)	(b)	(a)	(b)
CUTO	1.703	0.657	2.930	0.564	22.210	0.053	22.590	0.432
JFNG	2.824	1.154	4.549	0.955	33.288	0.124	37.502	0.102
SIN1	2.858	1.147	4.771	0.994	32.221	0.088	34.371	0.363
HKOH	3.124	1.217	5.405	1.177	41.003	0.008	39.039	0.444
HKSL	2.554	1.087	4.686	1.065	37.390	0.034	36.456	0.278
HKWS	2.568	1.066	4.744	1.078	4.744	0.082	37.216	0.219
MAJU	2.017	0.555	3.556	0.617	26.098	0.343	26.098	0.307
NAUR	2.159	0.629	3.732	0.642	25.770	0.125	25.237	0.321
NNOR	2.521	0.879	4.077	0.779	28.409	0.145	28.409	0.427
Mean	2.481	0.932	4.272	0.875	27.904	0.111	31.880	0.321
Improvement rate	62.4%		79.5%		99.6%		99.0%	

5.4 Summary

Large PMs and DIs within satellite clock products can be detected with ease in the time domain. We found that the PMs of satellite clock products will not cause the ISB jumps. Furthermore, the linear dependence between the ISB and satellite clock offsets in the time domain was studied, and numerical examples revealed a positive correlation between ISB differences and satellite clock offset residuals between adjacent days. That is the reason why we made preprocessing on the precise satellite clock product to eliminate the ISB discontinuity. To detect the small clock jumps, which may be hidden within the large-scale data, satellite clock data were transferred from the time domain into the frequency domain. As compared with time

domain data, frequency domain data are much more sensitive to jumps. Subsequently, a median filter-based robust estimation method was proposed to detect the jumps within the frequency domain data. With this method, we concluded that the extrema within frequency domain data are the true cause of the ISB jumps. In addition, smaller clock offset jumps were successfully detected and classified into three types according to their causes: small PMs, switches of reference clocks, and clock day boundaries. Different clock preprocessing strategies were applied to these three different causes. Then, the ISB was re-estimated with preprocessed clock products. From the test of the improvement in the ISB continuity, we found that the ISB continuity can be improved averagely by 85.1%, which means that the proposed preprocessing method for precise clock products is an appropriate way to detect and repair the ISB jumps.

When modeling discontinuous ISB series, the ISB series must be segregated into several components. With the clock product preprocessing method proposed in this chapter, a smoothed ISB series can be attained. In this manner, a more extended sample sequence can be used for modeling, and the modeling precision can be improved. ISB modeling research will be performed with this clock product preprocessing in the next chapter.

6 Inter-system bias modeling and prediction

6.1 Introduction

As expected, the multi-GNSS PPP is expected to enhance its solution accuracy, together with its reliability, and availability through the improvement of satellite geometry, in particular, in difficult terrain conditions where there exist limit satellites in view. The increase in the number of the observed satellites helps shorten the initialization time, together with eliminating the existing position errors caused by the periodic regression of satellite constellations (Flohrer 2008). Nevertheless, the calibration of inter-system biases (ISB) is regarded as the key point for the fusion of multi-GNSS data. It requires careful consideration in the function models and stochastic models in multi-GNSS combined PPP, which have been carried out in the former chapters.

If the ISB is appropriately represented as a model, it can be considered as a known parameter or at least an a priori constraint applied in the integrated positioning; subsequently, it helps with the initialization and accuracy of PPP. Accordingly, this chapter places emphasis on ISB modeling and prediction. We take a start with a brief description of the experimental data in Section 6.2. Thereafter, the ISB estimation methodology and coefficients estimation methodology are put forward in Section 6.3. In addition, section 6.4 presents both the results and analysis, for instance, the impacts of convergence period for ISB estimation, the elimination of ISB day jumps and smoothing, ISB modeling and predicting, and the impact on convergence time and PPP accuracy. Eventually, the summary of this chapter is presented in Section 6.5.

6.2 Experimental data

The Multi-GNSS Experiment (MGEX) is an IGS project for tracking, collating, and analyzing all of the available GNSS signals. This includes data from GPS, GLONASS, BeiDou, and Galileo, Quasi-Zenith Satellite System (QZSS), the Indian Regional Navigation Satellite System (IRNSS) and space-based augmentation systems (SBAS). Owing to the development of a global and dense multi-GNSS network, MGEX plays quite a pivotal role in the researches of the diversity of new signals and systematic characterization of the new navigation satellite systems. In the meantime, with the precise orbit and clock products generated from the analysis centers (ACs), the observations from the MGEX network have been extensively applied in multi-GNSS positioning experiments as well as other applications. In the subsequent years, one of the key jobs for MGEX is going to focus on the full integration activities in all multi-GNSS, in addition to providing coherent and transparent services for all of the existing satellite navigation systems, then further increasing their joint use in the high-precise science and engineering applications (Montenbruck et al. 2017).

For the purpose of investigating the characteristics of ISB and making a modeling, we choose observations from 26 stations in the MGEX network that are capable of obtaining a minimum of 3 satellite systems (GPS, Galileo, and BDS), which encompass a one-week period from Oct. 15 to 21, 2017, suggesting the GPS week 1971 with the DOY (day of year) from 288-294 in the year of 2017. Furthermore, observations during the next week (GPS week 1972, from Oct. 22 to 28, 2017) are used for assessment of the precision of the prediction using the proposed model. The distribution of these tracking stations is shown in Figure 6.1.

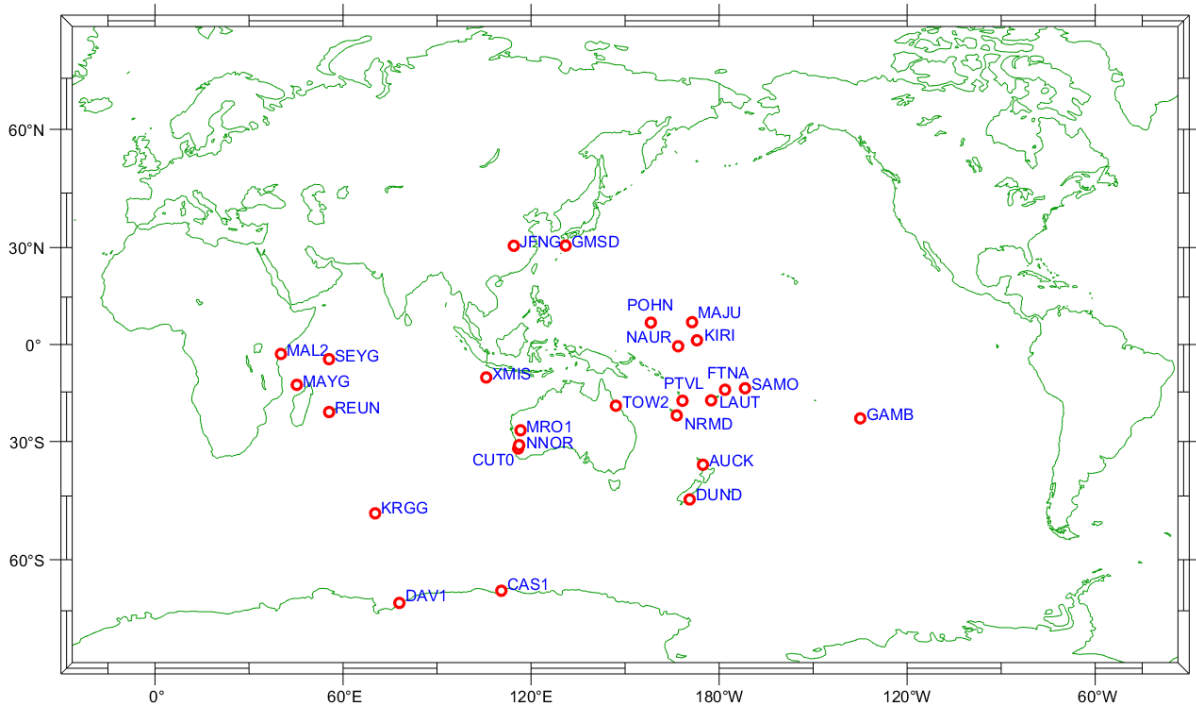


Figure 6.1 Distribution of 26 stations in the MGEX network.

6.3 Estimation model and processing strategy

Herein, the PPP solution strategy is applied for ISB estimation, which can be derived together with other unknown parameters. We make use of an extended Kalman filter for the estimation of the ISB as a piece-wise constant every 30 min. Subsequent to analyzing the properties of ISB, it is regarded that the ISB can be fitted as a quadratic function, besides a number of periodic functions. Hence we employ a frequency spectrum methodology to detect the different periods of periodic functions. The least square method (LS) is applied for the determination of the coefficients of both types of functions.

6.3.1 PPP model for ISB estimation

In general, the ionospheric-free (IF) pseudorange and phase observations are utilized in PPP to eliminate the first-order impact of the ionosphere. The observation equations can be written as hereunder (Kouba 2009):

$$\begin{aligned}
P &= \rho + c \cdot (dt_r - dt^s) + (b_r - b^s) + T + \tau_p \\
L &= \rho + c \cdot (dt_r - dt^s) + (B_r - B^s) + T + N + \tau_L
\end{aligned}
\tag{6.1}$$

where P and L indicate the ionospheric-free combination of pseudorange and carrier phase, correspondingly, c represents the speed of light, dt_r and dt^s denote the receiver and satellite clock biases, b_r , b^s and B_r , B^s are the pseudorange and carrier phase hardware delay biases of the ionospheric-free function for receivers and satellites, T is the tropospheric delay, N implies the phase ambiguity in units of meters; τ_p and τ_L are the indications of unmodeled parameters (for instance, the measurement noise and multipath errors for pseudorange and carrier phase), and ρ denotes the geometric distance between the phase centers of the satellite and the receiver antennas at the signal transmission and reception time, respectively. The phase center offset and variation, relativistic effects, tidal loading, ocean tide, earth rotation effects, and phase wind up, requires mandatory correction in accordance with the existing models (Kouba 2009) despite the fact that they are not explicitly included in the equations.

With regard to GNSS observations, the pseudorange hardware delay biases b_r , b^s are assimilated into the clock offset $c \cdot (dt_r - dt^s)$. In the majority of GNSS data processing, the carrier phase hardware delay biases B_r , B^s are not taken into account. The carrier phase hardware delay bias is satellite-dependent, together with being stable over time. In this manner, it is absorbed by the ambiguity (Defraigne et al. 2007a; Geng et al. 2012). Upon the use of the precise satellite orbits and clocks, Equation (6.1) can be rewritten as hereunder:

$$\begin{aligned}
P &= \rho + c \cdot \overline{dt_r} + T + \tau_p \\
L &= \rho + c \cdot \overline{dt_r} + T + \overline{N} + \tau_L
\end{aligned}
\tag{6.2}$$

where $\overline{dt_r}$ and \overline{N} are the modified receiver clock and ambiguity:

$$\begin{aligned} c \cdot \overline{dt_r} &= c \cdot dt_r + b_r \\ \overline{N} &= N + B_r - b_r \end{aligned} \quad (6.3)$$

The equation (6.2) demonstrates the PPP observation equation, wherein the satellite hardware delays can be removed in the course of the application of the precise satellite clocks (Defraigne et al. 2007a). As evident from Equation (6.3), the ambiguity does not constitute an integer since it contains the bias term; the term $B_r - b_r$ refers to the un-calibrated phase delay (Ge et al. 2008)

GPS/BDS or GPS/Galileo PPP deals with combined PPP that makes use of observations from the GPS and BDS, or Galileo satellite constellations, where precise satellite orbits and clock products can be availed from the MGEX ACs. The fusion PPP model asks for estimating an extra inter-system bias (ISB) parameter. Accordingly, the combined observation model can be expressed as hereunder:

$$\begin{aligned} P^G &= \rho^G + c \cdot \overline{dt_r} + T + \tau_p \\ L^G &= \rho^G + c \cdot \overline{dt_r} + T + \overline{N^G} + \tau_L \\ P^O &= \rho^O + c \cdot (\overline{dt_r} + ISB) + T + \tau_p \\ L^O &= \rho^O + c \cdot (\overline{dt_r} + ISB) + T + \overline{N^O} + \tau_L \end{aligned} \quad (6.4)$$

where $\overline{dt_r}$ denotes a common item, which is the receiver clock term that relates to the GPS system. The superscript G refers to GPS and O means BDS or Galileo system. The ISB is the inter-system bias parameter between GPS/BDS or GPS/Galileo in the units of time. It will be modeled as an unknown parameter and estimated together with the other parameters, for instance, coordinates and receiver clock. Accordingly, we are able to consider the estimated parameter vector \overline{X} as hereunder:

$$\overline{X} = \left[x, y, z, \overline{dt_r}, ISB, T, \overline{N^G}, \overline{N^O} \right] \quad (6.5)$$

where $\overline{N^G}$ $\overline{N^O}$ indicate the modified ambiguity parameters for different systems. In addition, an extended Kalman filter is employed for the purpose of estimating the unknown parameters in the processing.

The estimation of the ISB parameter can be carried out with different stochastic models, such as white noise, random walk, piece-wise constant, or processing arc-dependent constant, which were mentioned and investigated comprehensively in chapter 4. A different model should be applied, when the correspondingly precise products are utilized from different ACs. Herein, we make use of the precise clock product from the Wuhan University (*WUH*), so the model of considering as the ISB as a 30 min interval piece-wise constant is applied.

All through the preprocessing, we detect and repair clock jumps for the avoidance of the misidentification of an observation jump due to the receiver clock jump as a cycle slip. Subsequent to that, the Geometry-Free (GF) and Hatch-Melbourne-Wubben (HMW) (Hatch 1982) combinations are employed for detecting cycle slips. An extended Kalman filter (EKF) is employed to estimate the unknown parameters. A cut-off elevation angle of 7° and an elevation-dependent weighting methodology are applied as well. The MGEX precise satellite orbits and clocks from WUH are put to use in the combined PPP processing. The tropospheric delay is corrected for its dry component with the use of the Saastamoinen model. On the other hand, the residual zenith wet delay is estimated as a random-walk process. We apply the Global Mapping Function (GMF) (Böhm et al. 2006) for the conversion of the zenith delay to slant directions. Also, the phase-wind up effects (Wu et al. 1992), the solid earth tide, the ocean loading tide (Petit and Luzum 2010) and relativistic effects are taken into account as well. Nonetheless, up to now, the receiver phase center correction for the BDS system has not been fully calibrated; accordingly, we make use of the same strategy as the GPS processing. Table 6.1 illustrates the summary of the combined PPP models and data processing strategies.

Table 6.1 Observation models and data processing strategies for combined PPP.

Item	Models and Strategies
Tracking data	26 MGEX stations observations
Processing period	Oct. 15 to 21, 2017 for ISB modeling; Oct. 22 to 28, 2017 for ISB prediction
Estimator	Extended Kalman filter (EKF)
Observations	Undifferenced ionospheric-free code and phase combination
Signal selection	GPS: L1/L2, BDS: B1/B2, Galileo: E1/E5a
Elevation angle cut-off	7°
Sampling rate	30 s
Precise orbit and clock	Fixed, MGEX precise products from <i>WUH</i>
Tropospheric delay	Saastamoinen model & random walk process
Mapping function	Global Mapping Function (GMF)
Ionospheric delay	First order effect eliminated by ionospheric-free linear combination
Phase-windup effect	Corrected
Earth rotation	Fixed, IGS ERP product
Satellite Antenna PCO & PCV	PCO and PCV are used with <i>igs14.atx</i>
Receiver Antenna PCO & PCV	PCO and PCV for GPS and Galileo from <i>igs14.atx</i> are utilized; Corrections of BDS is applied the same as GPS
Relativistic effects	IERS Convention 2010
Tides correction	IERS Convention 2010
Receiver clock biases	Estimated as white noise for each epoch
Phase ambiguity	Estimated as constant for each ambiguity arc
ISB	Estimated as a piece-wise constant every 30min

6.3.2 ISB modeling and coefficients estimation

Considering the attribute of ISB, the fitting model can be stated as a sum of a quadratic function and several periodic functions. We apply frequency spectrum analysis for detection of the varying periods of the periodic functions. The frequency spectrum can be generated by

means of a Fourier transform from the time-domain signal, and the consequent values are typically presented as amplitude versus frequency (Mann et al. 1989). Any signal that can be represented by an amplitude varying with time has a respective frequency spectrum. In this study, we make use of a fast Fourier transform (FFT) for the analysis of the ISB signal frequency spectrum. FFT, an algorithm for computing the discrete Fourier transform (DFT), together with its inverse, rapidly converts time to the frequency and vice versa (Bergland 1969). The specific algorithm of FFT refers to (Duhamel and Vetterli 1990).

Following the detection of the periods, LS is applied for the determination of the coefficients of the periodic functions as well as the quadratic function. For the application of the sliding window median filter, we are capable of obtaining a clean ISB set of values without outliers. Accordingly, LS is deemed as appropriate for estimating the unknown coefficients. Nevertheless, application of the robust least-squares is recommended (Yang et al. 2002; Zhou 1989), on account of its exceptional potential for data quality control (outliers detecting and repairing).

6.4 Results and discussion

For the purpose of presenting the results and analysis for the assessment of the performance of ISB estimation, together with validating the station-dependent model for ISB, and the prediction accuracy of the ISB model, we carry out the PPP processing of 26 stations from the MGEX network for GPS week 1971 and 1972, in accordance with the processing strategy highlighted above in Table 6.1. Herein, we provide the results from 9 chosen stations as an example that are presented in Table 6.2 comprehensively.

Table 6.2 The details of 9 chosen stations, including locations, receiver types, and the clock type inside receiver.

Station ID	Location		Receiver type/Firmware version	Clock type
	Lat.	Long.		
CAS1	-66.2833	110.5194	TRIMBLE NETR9/5.22	INTERNAL
FTNA	-14.3078	-178.1209	TRIMBLE NETR9/5.22	INTERNAL
KRGG	-49.3514	70.2553	LEICA GR10/ 4.11-6.523	INTERNAL
LAUT	-17.6088	177.4466	TRIMBLE NETR9/5.22	INTERNAL
MAJU	7.1189	171.3644	SEPT POLARX4TR/2.9.6	INTERNAL
MAL2	-2.9958	40.1939	SEPT POLARX4/2.9.5	-
POHN	6.9597	158.2100	TRIMBLE NETR9/5.22	INTERNAL
PTVL	-17.7494	168.3150	TRIMBLE NETR9/5.22	INTERNAL
REUN	-21.2083	55.5717	TRIMBLE NETR9/4.85	INTERNAL

6.4.1 Impacts of convergence period for ISB estimation

As already established, in comparison with the relative positioning mode, PPP has advantages, for instance, high processing efficiency, no need of reference stations, and flexible operating mode without any limitation by distance, meanwhile still requiring a long convergence period of 30 min or more for the achievement of the centimeter-level accuracy (Geng et al. 2011; Li and Zhang 2014). Owing to this initialization time, the estimated ISB series also contains a period of convergence, which is apparently indicated in Figure 6.2. It takes the estimated ISB series in station KRGG on Oct. 15, 2017, as an example. Inside Figure 6.2, the black curve, in accordance with the left axis, is the ISB between GPS and BDS (GC), and the blue one that corresponds to the right axis shows the ISB between GPS and Galileo (GE).

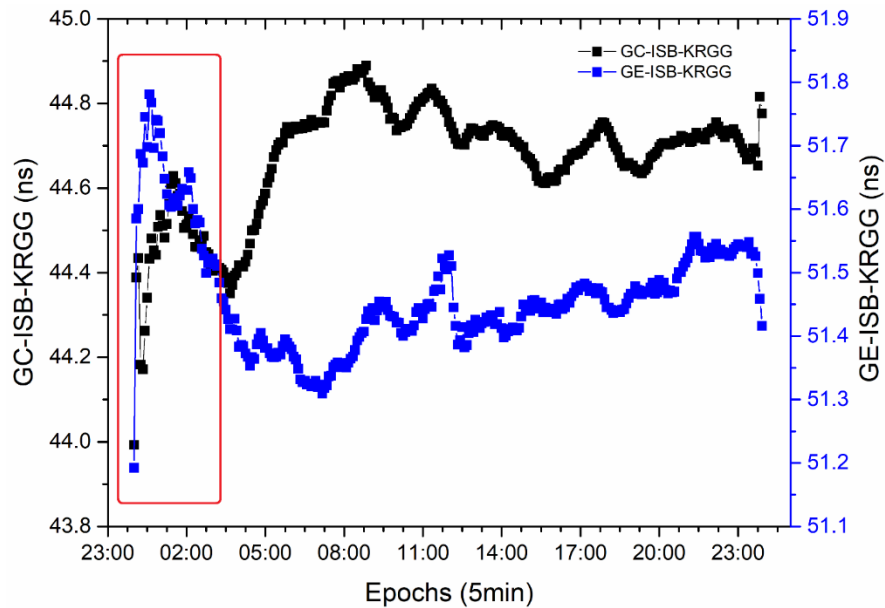


Figure 6.2 The ISB series of station KRGG on Oct. 15, 2017, in the 5min interval as an example, the black curve is the ISB between GPS and BDS, and the blue one is the ISB between GPS and Galileo, in the red box is the convergence period of ISB.

As evident from Figure 6.2, both in the case of GC, and GE, owing to the initialization phase in the forward filter processing, the estimated ISB exists a convergence period with turbulent values. In a case where we take the ISB of this period into modeling, it is expected to give rise to the unstable of ISB fitting, besides impacting the modeling accuracy. Hence, prior to ISB modeling, we require removing this impact from the convergence phase, so a methodology of the combined filter is employed here. In comparison with the forward filter only with a single direction data processing, combined filter offers the benefits of double directions data handling on the basis of the final information of forward filter.

Standard deviation (STD) can be used as a measurement for data stability. STD comparison between forward and the combined filter is presented in Figure 6.3. In GC case we take stations FTNA, KRGG, LAUT, MAJU, MAL2, and PTVL for instance, while for GE case, stations CAS1, KRGG, MAJU, MAL2, POHN, and REUN are taken as an example. The corresponding statistics of daily and mean ISB STD for GC case, and GE case are demonstrated in Table 6.3 and Table 6.4.

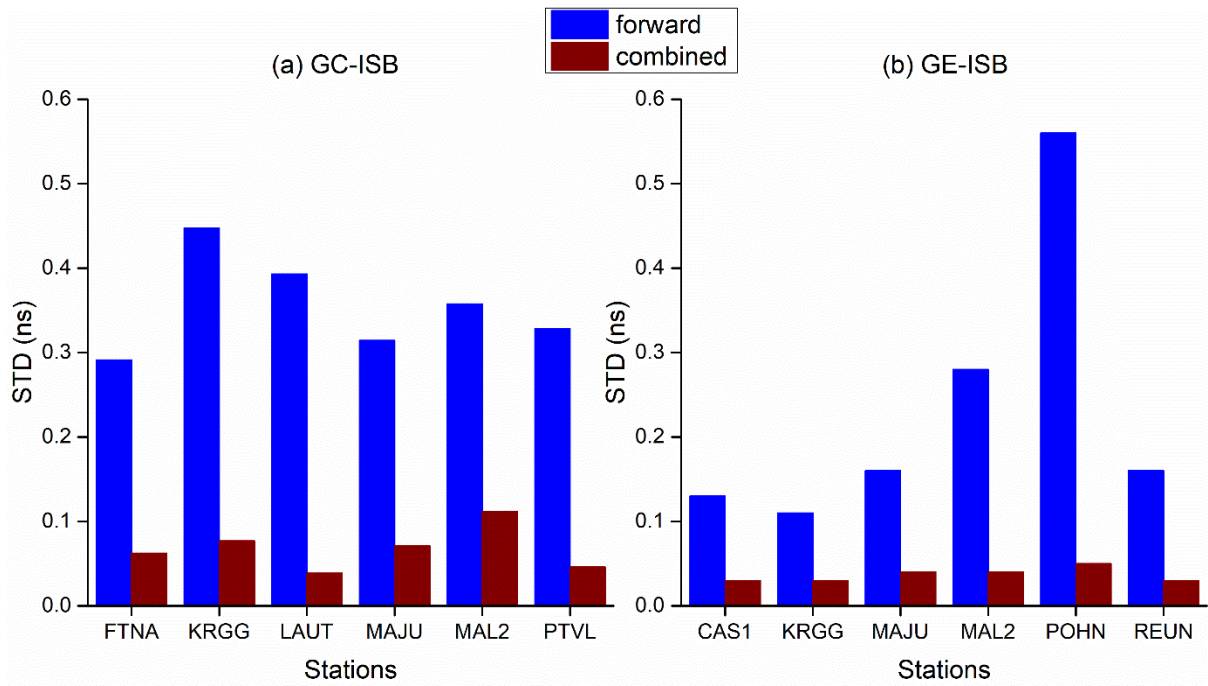


Figure 6.3 Weekly mean STD comparison of ISB between forward and combined filter, (a) is the consequence of GC case, while (b) is the GE case, the blue color column shows the STD of forward filter, and the STD of the combined filter is indicated as wine color column.

Table 6.3 Statistics of daily and mean ISB from forward and combined filter in GC case, f means forward filter, while c is combined filter, unit: ns.

Station ID	FTNA		KRGG		LAUT		MAJU		MAL2		PTVL	
	f	c	f	c	f	c	f	c	f	c	f	c
288	0.30	0.07	0.12	0.11	0.23	0.03	0.37	0.04	0.27	0.08	0.43	0.05
289	0.20	0.06	0.47	0.10	0.24	0.05	0.29	0.10	0.45	0.19	0.31	0.07
290	0.22	0.11	0.54	0.07	0.49	0.04	0.20	0.05	0.42	0.12	0.38	0.04
291	0.29	0.05	0.78	0.08	0.67	0.03	0.26	0.08	0.45	0.14	0.35	0.03
292	0.30	0.06	0.41	0.05	0.43	0.06	0.44	0.12	0.24	0.09	0.33	0.03
293	0.41	0.05	0.33	0.09	0.28	0.04	0.29	0.05	0.35	0.09	0.29	0.05
294	0.31	0.03	0.47	0.05	0.41	0.03	0.35	0.06	0.32	0.08	0.22	0.05
Mean	0.29	0.06	0.45	0.08	0.39	0.04	0.31	0.07	0.36	0.11	0.33	0.05

Table 6.4 Statistics of daily and mean ISB from forward and combined filter in GE case, f means forward filter, while c is combined filter, unit: ns.

Station ID	CAS1		KRGG		MAJU		MAL2		POHN		REUN	
	f	c	f	c	f	c	f	c	f	c	f	c
288	0.08	0.03	0.09	0.03	0.11	0.04	0.31	0.05	0.63	0.04	0.09	0.03
289	0.13	0.02	0.1	0.04	0.18	0.05	0.27	0.04	0.56	0.02	0.17	0.03
290	0.1	0.02	0.1	0.01	0.14	0.02	0.25	0.04	0.61	0.06	0.23	0.05
291	0.17	0.02	0.12	0.04	0.11	0.04	0.24	0.03	0.6	0.05	0.11	0.02
292	0.15	0.06	0.07	0.02	0.16	0.05	0.33	0.04	0.44	0.06	0.25	0.05
293	0.12	0.04	0.20	0.05	0.22	0.04	0.38	0.05	0.49	0.08	0.20	0.03
294	0.14	0.02	0.09	0.03	0.19	0.06	0.21	0.03	0.59	0.05	0.10	0.02
Mean	0.13	0.03	0.11	0.03	0.16	0.04	0.28	0.04	0.56	0.05	0.16	0.03

It is noted that in Figure 6.3 together with Table 6.3 and Table 6.4, with the combined filter, the ISB stability can be efficiently enhanced, suggesting that, in comparison with the forward filter PPP processing, the impact of convergence period for the ISB is significantly weakened by the combined filter way. The improvement rate has the potential to averagely reach 80.8% in GC case, and 84.3% in the GE case, correspondingly.

6.4.2 Elimination of ISB day jumps and smoothing

We estimate ISB as a piece-wise parameter every 30 mins, together with other unknowns in PPP mode. The observations combinations of GPS/BDS (GC), and GPS/Galileo (GE) in GPS week 1971 are applied for the purpose of testing the ISB estimation.

The estimated ISB series for GC case in GPS week 1971 is presented in Figure 6.4. Herein, we termed these untreated series as original ISB series (ISB_o). The same period ISB series of GE case are displayed in Figure 6.5.

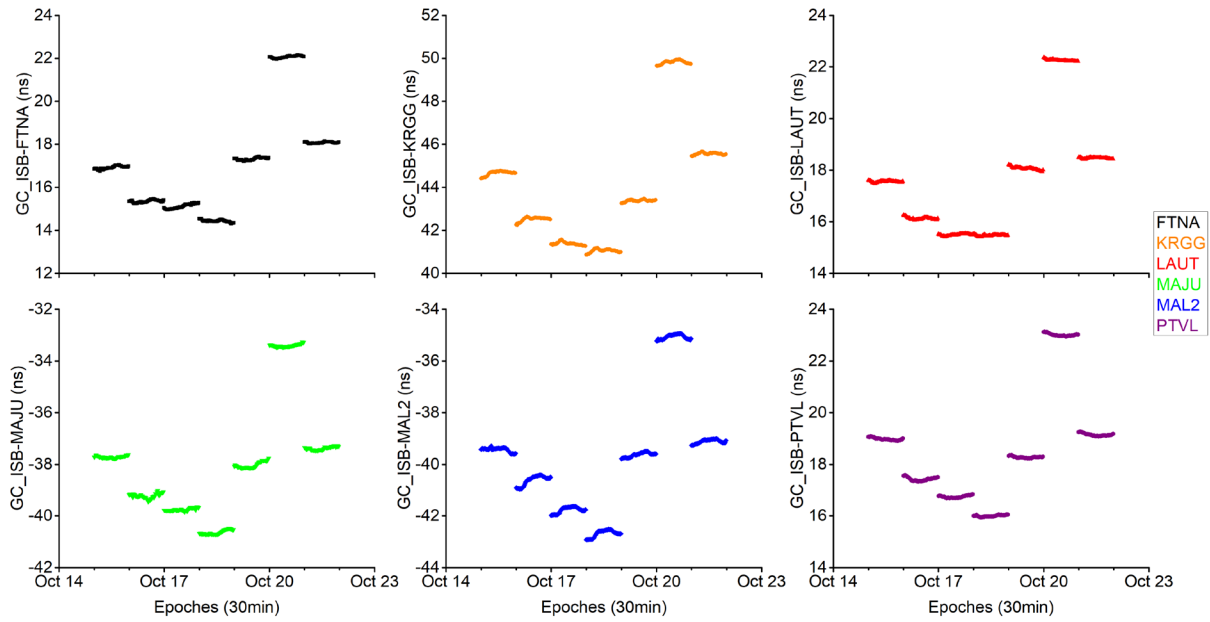


Figure 6.4 Original ISB series during GPS week 1971 in GC case, taking stations FTNA, KRGG, LAUT, MAJU, MAL2, and PTVL for example.

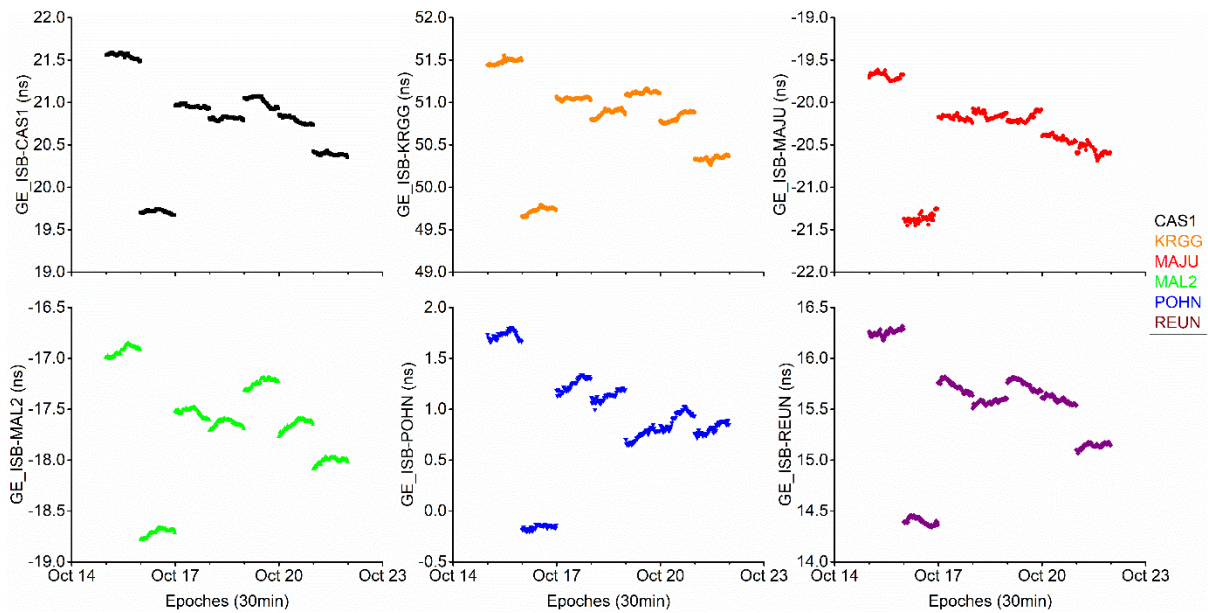


Figure 6.5 Original ISB series during GPS week 1971 in GE case, with the use of stations CAS1, KRGG, MAJU, MAL2, POHN, and REUN as an example.

As indicated by the two figures above, it can be seen that the estimated ISB is a station-dependent parameter, that is because ISB is primarily associated with the types of receivers (Nadarajah et al. 2015); also, the surrounding environment impacts the ISB estimation (Zhang et al. 2018). Each station is likely to have a different surrounding condition, which means different ISB will be derived in different stations. In particular, it is of concern that, both in GC and GE case, a mass of day jumps are discovered in the ISB series, primarily caused by the truncation error by the daily processing strategy of precise clock product in AC. Such ISB day jumps are expected to exert an impact on the fitting accuracy of ISB; so prior to ISB modeling, it is deemed as essential to maintaining the continuity of the IBS series.

Elimination of ISB day jumps

Since ISB is strongly correlated with the satellite clock error, the method of precise clock product preprocessing based on the study in chapter 5 is applied for making the treatment of ISB day jumps. When the ISB increment in adjacent days is beyond an experiential threshold, here we set this threshold value as STD of ISB on the former day; in addition, the precise clock product preprocessing should be carried out, and the original precise clock product is replaced by the processed one. Then the ISB derived from the processing clock product (named as processed ISB) substitutes for that from the original clock product. Otherwise, if the increment is below the threshold, we make no operations, and the processed ISB remains as the original series. Following the removal of day jumps, the continuous processed ISB (ISB_p) series of GC and GE case are indicated in Figure 6.6 and Figure 6.7.

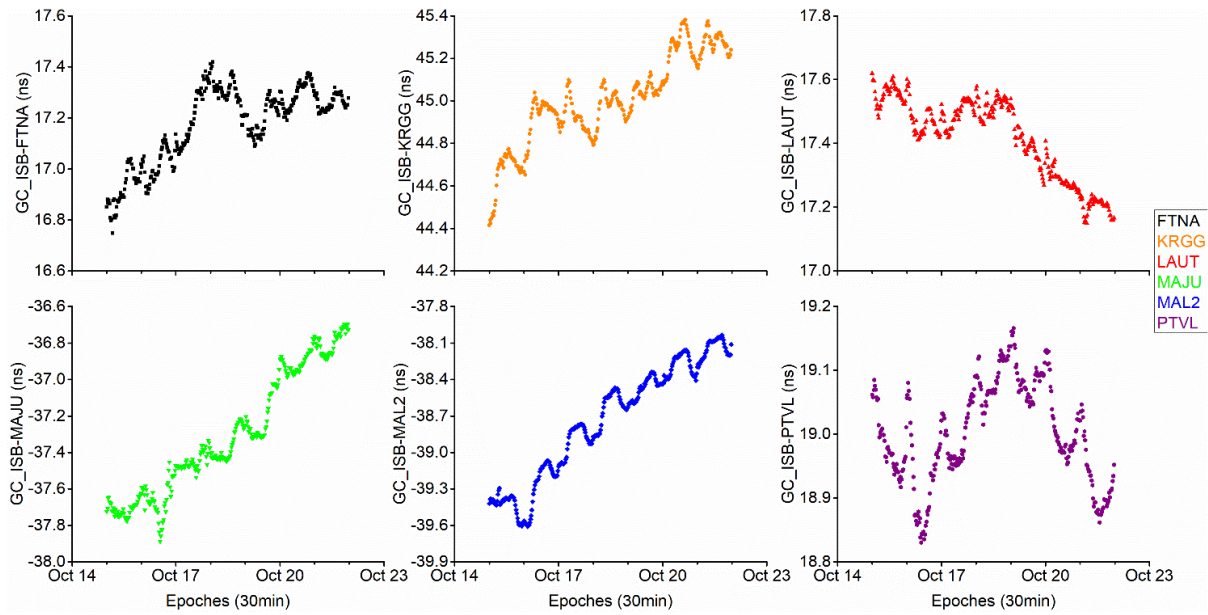


Figure 6.6 Processed ISB series without day jumps during GPS week 1971 in GC case, taking stations FTNA, KRGG, LAUT, MAJU, MAL2, and PTVL for example.

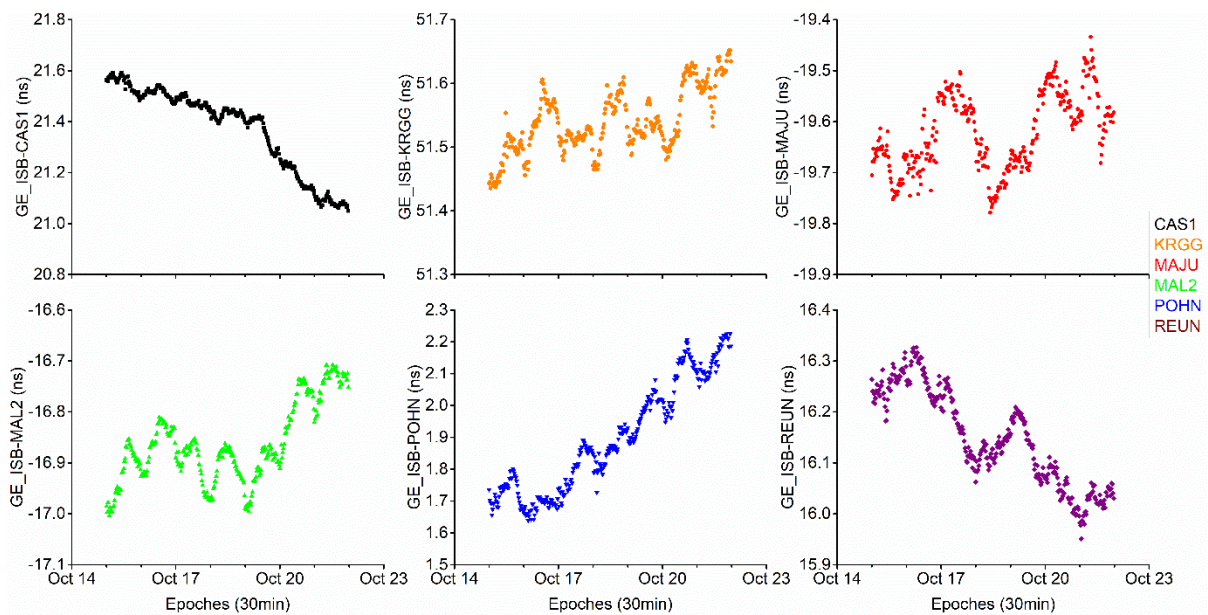


Figure 6.7 Processed ISB series without day jumps GPS week 1971 in GE case, with the use of stations CAS1, KRGG, MAJU, MAL2, POHN, and REUN as an example.

As evident from both figures above, subsequent to the preprocessing of precise clock product, a continuous ISB series is successfully attained both in GC and GE case. However, it also can be found that some outliers and error points are still existent in the processed ISB series. That is why we apply a sliding window median filter for the purpose of generating the smoothed ISB series since the median has a good potential to reject outliers.

Smoothing of processed ISB

Following the two steps of the elimination of ISB day jumps, together with making use of the sliding window median filter into ISB_p, the smoothed ISB (ISB_s) series are formed eventually. The comparisons of ISB_p and ISB_s during the period of GPS week 1971 for GC and GE case are shown in Figure 6.8 and Figure 6.9, correspondingly.

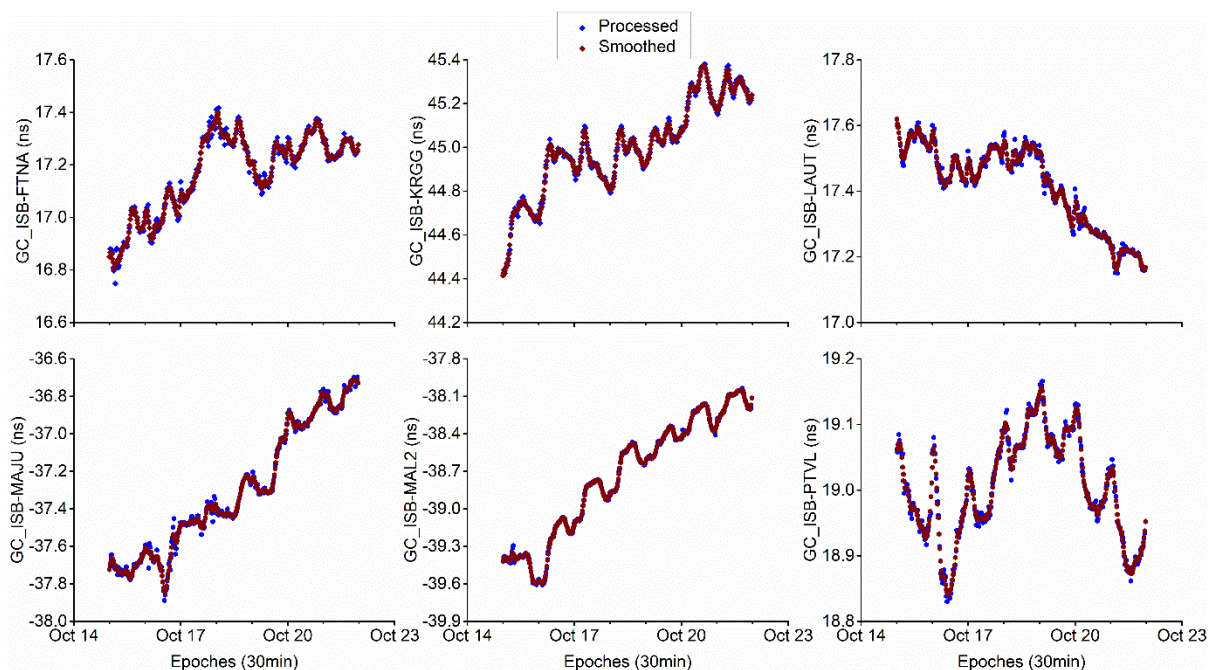


Figure 6.8 Comparison of processed ISB and smoothed ISB for GC case in GPS week 1971, ISB_p is shown in blue color, while the wine color denotes ISB_s.

As evident from Figure 6.8 and Figure 6.9, the filtered ISB series (ISB_s) is more robust and smoother in comparison with the processed series, indicating that the sliding window

median filter is capable of effectively eliminating the outliers and improving the reliability of the ISB series.

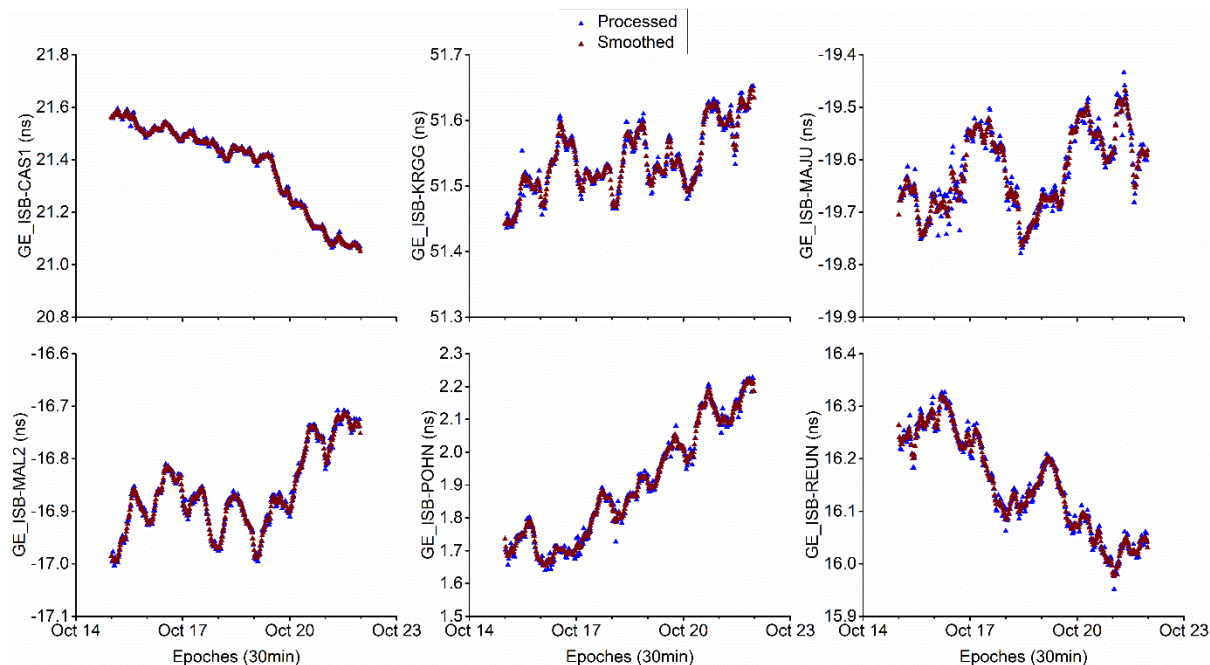


Figure 6.9 Comparison of processed ISB and smoothed ISB for GE case in GPS week 1971, ISB_p is presented in blue color, while the wine color represents ISB_s.

6.4.3 ISB modeling

By means of the analysis of the characteristics of ISB_s, together with considering the correlation between ISB and the residual satellite orbit and clock errors, the ISB can be approximately expressed as a quadratic function, together with a number of periodic functions with different periods. Accordingly, the ISB model can be presented as hereunder:

$$ISB = A \cdot t^2 + B \cdot t + C + \sum_{i=1}^n \left(D_i \cdot \cos\left(\frac{2\pi t}{P_i}\right) + E_i \cdot \sin\left(\frac{2\pi t}{P_i}\right) \right) \quad (6.6)$$

$$t = T - T_{or}$$

where A , B , and C represent the coefficients of the quadratic, first-order, and constant terms for the polynomial, respectively. The symbols D_i and E_i are the coefficients of the

periodic functions, P_i denotes the periods of the periodic functions. t represents the sampling points; with regard to T and T_{or} , they indicate the time of current epoch and the time of reference epoch, correspondingly. Herein, we considered T_{or} as the first epoch time of GPS week 1971, besides marking as 0. A , B , C , D_i , and E_i are termed as the unknown parameters that require estimation in accordance with LS method, and the different periods of the periodic functions are derived from the frequency spectrum analysis outlined earlier.

Table 6.5 The coefficients estimated by LS for the polynomial and periodic functions in GC case, A , B , and C are quadratic, first-order, and constant terms of the polynomial; in addition, D_i and E_i denote the coefficients of the periodic functions, and P_i means the coefficients of the periods.

Station ID/Coefficients	A (10^{-6})	B (10^{-4})	C (10^{-4})	D_i (10^{-4})	E_i (10^{-4})	P_i (day)
FTNA	-8	37.92	168344.27	406.30	-538.57	7/2
				-268.99	386.16	7/3
				67.53	-494.89	1
KRGG	1	14.96	447164.86	-667.92	-285.36	7/2
				-682.33	56.00	1
LAUT	-6	8.74	174922.04	531.03	15.40	7/2
				-0.89	-214.79	1
MAJU	5	18.46	-377836.76	59.53	445.86	7/3
				617.43	59.56	1
MAL2	-8	73.68	-396795.56	-1026.02	-207.45	1
PTVL	-6	22.52	188583.48	272.30	414.90	7/2
				369.70	151.45	1

The results of each coefficient for GC and GE case are presented in Table 6.5 and Table 6.6, respectively. Both GPS/BDS and GPS/Galileo ISB in all stations are constituted by a polynomial, together with a minimum of one periodic function, whereas some stations have two or three different periods. All of them typically contain one day, semi-weekly, or 1/3 weekly periods. The probable reason is that ISB can still be impacted by the residual errors, for instance, the residual satellite clock error, satellite orbit error, and the unconsidered errors, like a multipath error. The residual satellite clock offsets show in the characteristics of a quadratic polynomial, and the satellite orbit error contains a daily period. For the multipath error, it has a property of irregularly repeated periodicity.

Table 6.6 The coefficients estimated by LS for the polynomial and periodic functions in GE case.

Station ID/Coefficients	A (10^{-6})	B (10^{-4})	C (10^{-4})	Di (10^{-4})	Ei (10^{-4})	Pi (day)
CAS1	-6	3.93	215255.14	218.58	219.20	7/2
				192.26	-95.51	7/3
				-113.27	-3.06	1
KRGG	1	0.15	515090.74	-181.96	-299.12	7/3
				-83.07	-274.39	1
				-463.60	-496.84	7/2
MAJU	1	-0.81	-196472.16	336.60	195.48	7/3
				100.91	182.01	1
				-325.13	-313.22	7/2
MAL2	5	-11.84	-168368.45	-278.99	-219.88	1
				60.25	340.68	7/3
				-149.28	-298.62	1
POHN	3	5.45	16720.55	-174.67	308.17	7/2
				78.42	-262.94	7/3
REUN	0	-8.36	162886.98			

In order to assess the fitting accuracy of the proposed model, we compare the ISB series derived from the model (ISB_m) with the smoothed one (assumed to be the true values). Figure 6.10 and Figure 6.11 show the values of ISB_s and ISB_m during the period of GPS week 1971 (from Oct. 15 to 21, 2017) for the stations mentioned before in GC and GE cases. One can see that the modeled ISB series agree well with the smoothed ISB both in GC and GE cases.

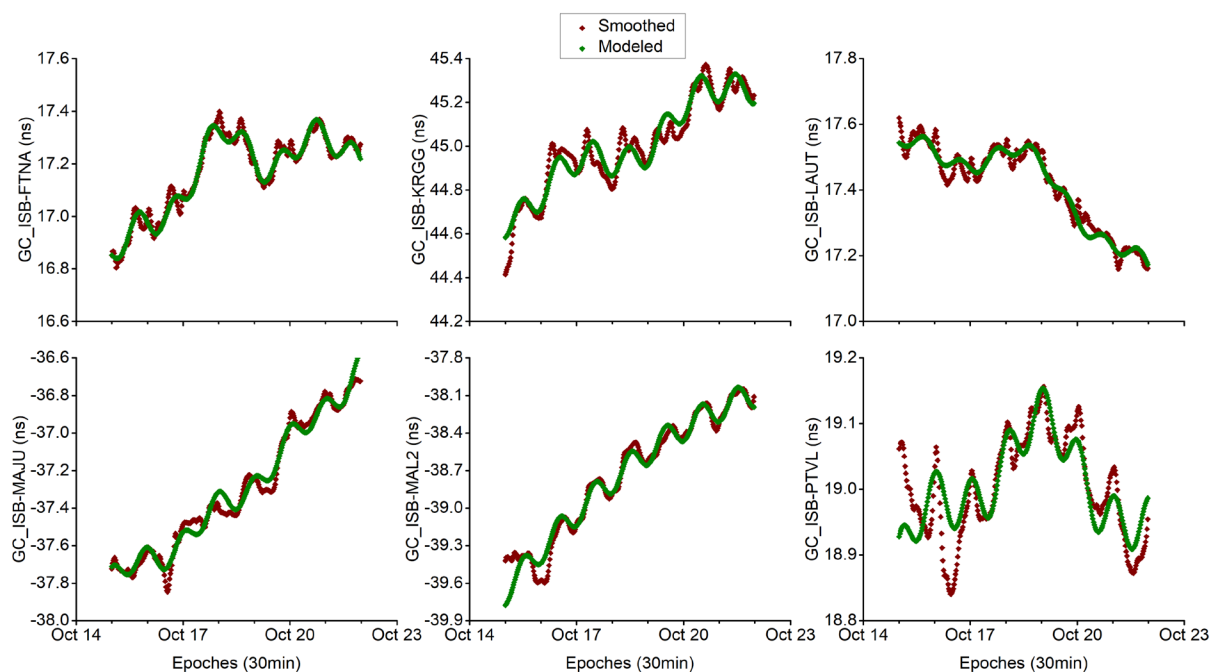


Figure 6.10 Smoothed (ISB_s) and modeled (ISB_m) series during GPS week 1971 at stations FTNA, KRGG, LAUT, MAJU, MAL2, and PTVL for the 30 min sampling interval in GC case.

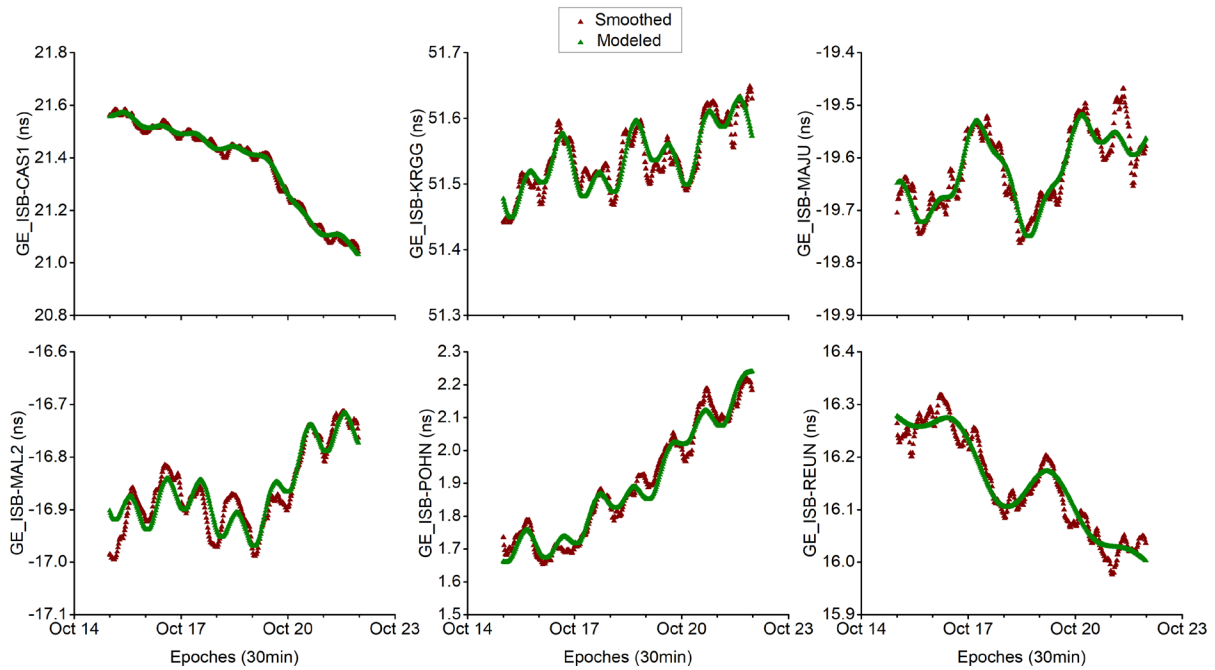


Figure 6.11 Smoothed (ISB_s) and modeled (ISB_m) series during GPS week 1971 at stations CAS1, KRGG, MAJU, MAL2, POHN, and REUN for the 30 min interval in GE case.

The distribution of differences derived from modeled and smoothed ISB series, together with the standard normal distribution curves are presented in Figure 6.12 and Figure 6.13, wherein the former one indicates the result for GC case, while the latter demonstrates the consequence for GE case. Evidently, the frequency counts of all deviations closely follow to a normal distribution, suggesting that, after modeling, the residuals remained in differences between ISB_s and ISB_m are only with random errors; in other words, the ISB model proposed above shows a reasonable fitting accuracy. The fitting precision is going to be comprehensively discussed in the following part.

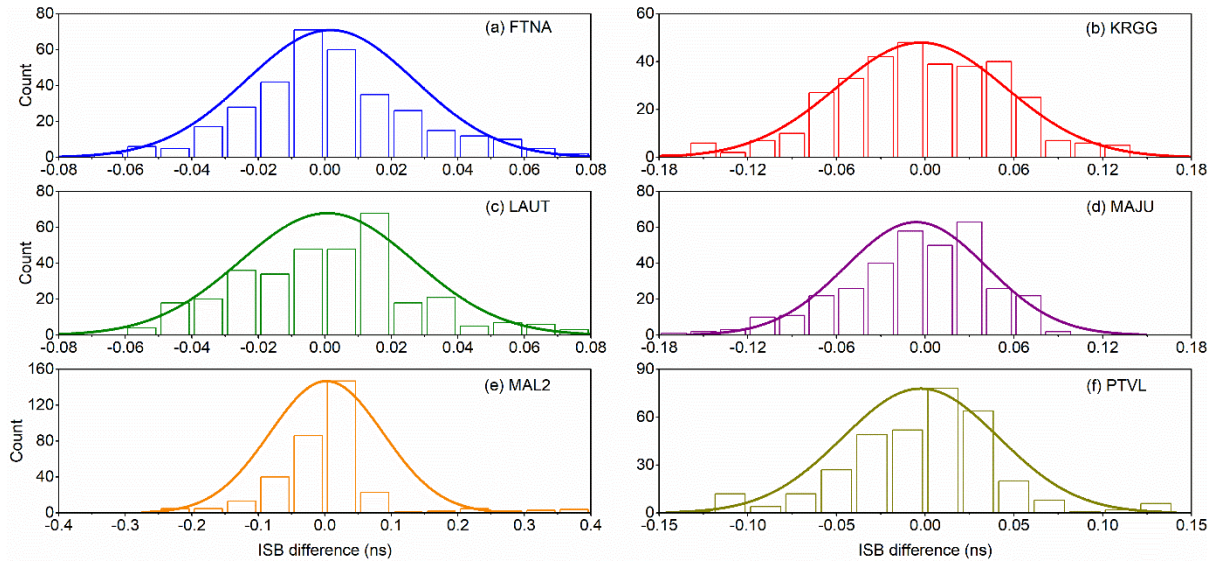


Figure 6.12 Distribution of the differences derived from modeled and smoothed ISB between GPS and BDS (GC) during GPS week 1971 at stations FTNA, KRGG, LAUT, MAJU, MAL2, PTVL.

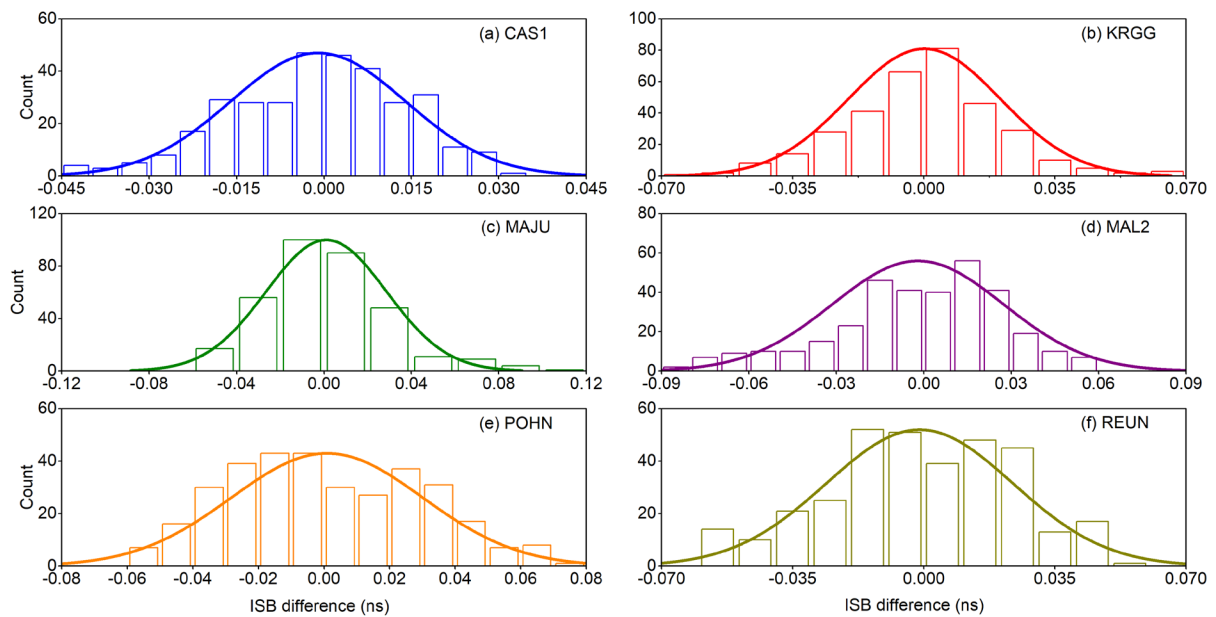


Figure 6.13 Distribution of the differences derived from modeled and smoothed ISB between GPS and Galileo (GE) during GPS week 1971 at stations CAS1, KRGG, MAJU, MAL2, POHN, REUN.

Table 6.7 and Table 6.8 shed light on the statistical results of the differences between the modeled and the smoothed ISB series in GC and GE cases, wherein the mean values of the differences for stations in GC case are 0.002 ns, -0.003 ns, 0.001 ns, -0.006 ns, 0.002 ns, and -0.003 ns, and the RMS of the differences are 0.025 ns, 0.057 ns, 0.026 ns, 0.048 ns, 0.085 ns, and 0.044 ns, indicating a mean accuracy level of approximately 0.048 ns; with regard to the GE case, the mean differences are -0.001 ns, 0.001 ns, 0.001 ns, -0.002 ns, 0.001 ns, and -0.001 ns, and the RMS for the differences are 0.015 ns, 0.020 ns, 0.028 ns, 0.029 ns, 0.029 ns, and 0.025 ns, and the average RMS is 0.024 ns. This indicates that the proposed ISB model in this study has a high fitting precision of 0.048ns, and 0.024 ns in GC, and the GE case, respectively. On the basis of these levels of fitting accuracy, this model is applicable to ISB prediction. In the following, we are going to perform the test of ISB prediction using this proposed model.

Table 6.7 The statistics of the fitting accuracy of the proposed model in the GC case at stations FTNA, KRGG, LAUT, MAJU, MAL2, PTVL (unit: ns).

Station ID	Max.	Min.	Mean	RMS	Mean RMS
FTNA	0.077	-0.067	0.002	0.025	
KRGG	0.130	-0.169	-0.003	0.057	
LAUT	0.076	-0.059	0.001	0.026	0.048
MAJU	0.082	-0.163	-0.006	0.048	
MAL2	0.374	-0.223	0.002	0.085	
PTVL	0.134	-0.123	-0.003	0.044	

Table 6.8 The statistics of the fitting accuracy of the proposed model in the GE case at stations CAS1, KRGG, MAJU, MAL2, POHN, REUN (unit: ns).

Station ID	Max.	Min.	Mean	RMS	Mean RMS
CAS1	0.030	-0.043	-0.001	0.015	
KRGG	0.064	-0.063	0.001	0.020	
MAJU	0.102	-0.058	0.001	0.028	
MAL2	0.059	-0.083	-0.002	0.029	0.024
POHN	0.074	-0.059	0.001	0.029	
REUN	0.050	-0.059	-0.001	0.025	

6.4.4 ISB prediction with the model

We perform with the aforementioned nine stations as an experiment in GPS week 1972 (from Oct. 22 to 28, 2017) for GC and GE cases, aimed at investigation the ISB prediction. Based on the model (Equation (6.6)) from the data of former GPS week 1971, the predicted ISB series (ISB_p) are generated with the variation of epoch time T in Equation (6.6). We estimate the ISB_o with PPP in combined filter mode for the removal of the impact of the convergence period, then ISB_p is attained from ISB_o by eliminating ISB day jumps, and eventually, the smoothed ISB (ISB_s) is attained based on ISB_p with the methodology of sliding window median filter in order to kick out the outliers. The accuracy of prediction is assessed through the comparison of ISB_p with ISB_s in GPS week 1972. The comparisons for GC, GE cases all through the seven-day period are presented in Figure 6.14 and Figure 6.15. It can be seen that from both figures as time goes on, the accuracy of prediction has a tendency to degrade. Nonetheless, both in GC and GE cases, the prediction precision in station KRGG has a phenomenon of increasing at the end part of the week period, wherein the possible reason is likely to be caused by the type of clock inside receiver, differing from other stations. So except station KRGG, the ISB_p of other stations shows full agreement with ISB_s during the first day period. Nevertheless, subsequent to this period, the agreement undergoes a marked decline, especially on the later days.

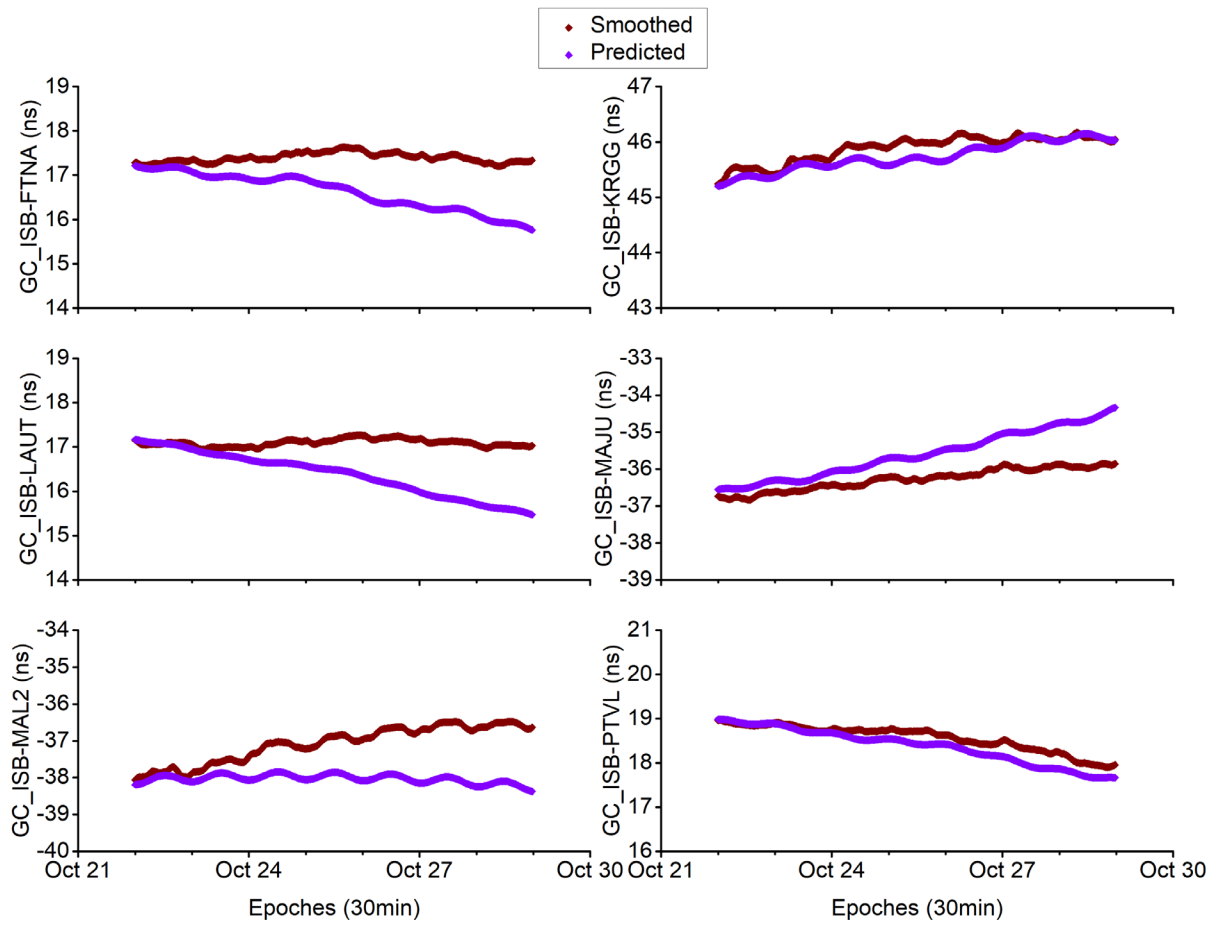


Figure 6.14 The comparison between predicted ISB (ISB_p) and the smoothed ISB (ISB_s) during the period of GPS week 1972 in the stations of FTNA, KRGG, LAUT, MAJU, MAL2, and PTVL for GC case.

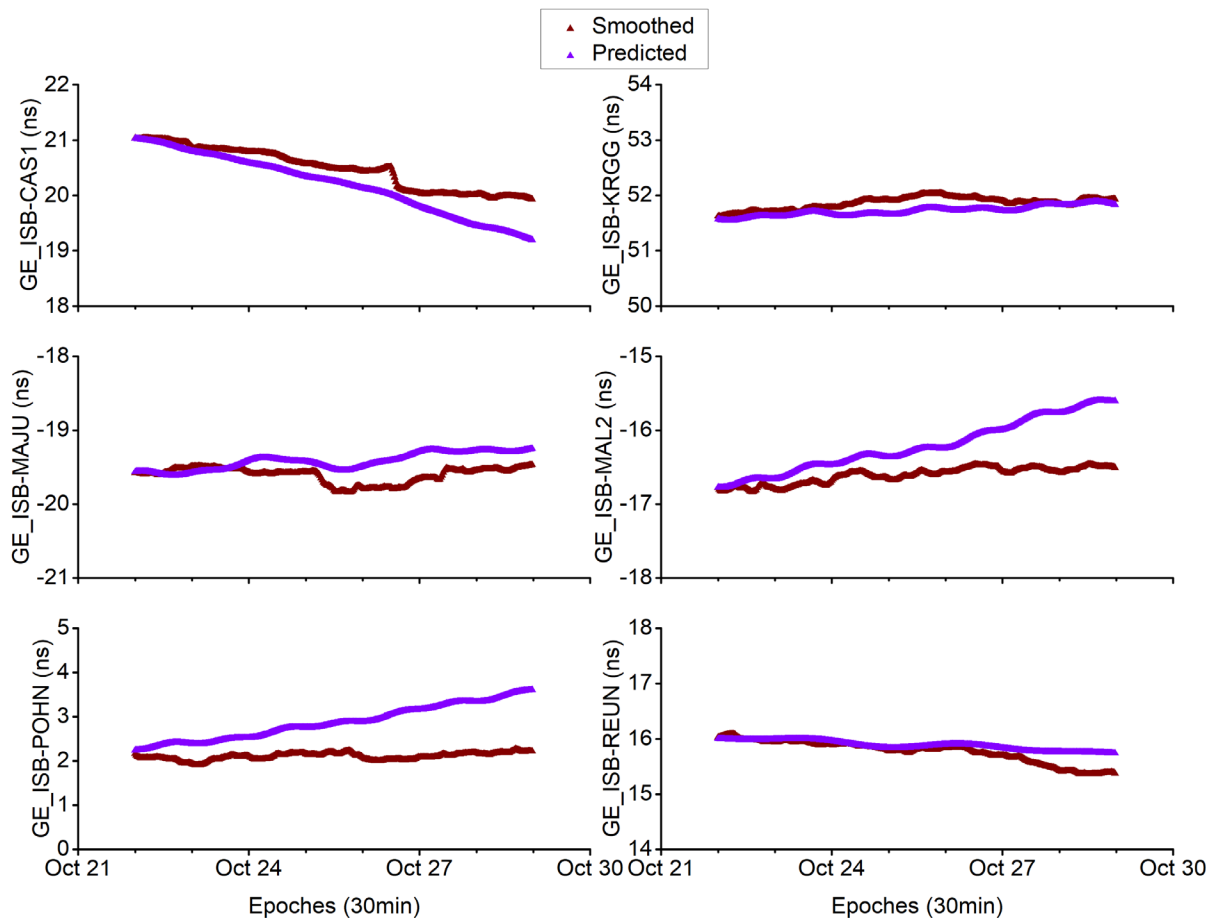


Figure 6.15 The comparison between predicted ISB (ISB_p) and the smoothed ISB (ISB_s) during the period of GPS week 1972 in the stations of CAS1, KRGG, MAJU, MAL2, POHN, and REUN for GE case.

Table 6.9 and Table 6.10 demonstrate the RMS values of the ISB differences between the smoothed and predicted values from the first day to the seventh day. As indicated in Table 6.9, the RMS of the ISB differences for GC case is 0.032-0.276 ns at the first day period in 6 stations, together with having a mean prediction accuracy level of 0.134 ns. With regard to the second day period, the average accuracy is 0.224 ns. As the day period goes on, the RMS becomes increasingly bad, which is consistent with Figure 6.14. With regard to Table 6.10, the prediction RMS of the GE case on the first day has a mean accuracy level of 0.116 ns. Nonetheless, with regard to station POHN, the RMS (0.322 ns) is more than three times larger as compared with the mean RMS of other stations, which is 0.058 ns. In this way, we regard

it as an outlier. As these tests suggest, we recommend the ISB prediction duration to be one day. The comparison of the ISB prediction further verifies the external accuracy of the proposed ISB model as well as its benefit for prediction purpose. Since the ISB prediction derived from this model can be regarded as an a priori information, this is likely to help enhance the accuracy and shorten the processing time. The potential effects of this proposed model for GPS/BDS and GPS/Galileo PPP are going to be investigated in the following section.

Table 6.9 Statistics of predictions for GC ISB from the first day to the seventh day in GPS week 1972 from Oct. 22 to 28 (from 1st day to 7th day), 2017 (unit: ns).

Station ID	1 st	2 nd	3 rd	4 th	5 th	6 th	7 th
FTNA	0.133	0.356	0.509	0.827	1.088	1.180	1.353
KRGG	0.141	0.106	0.260	0.329	0.251	0.062	0.035
LAUT	0.060	0.174	0.443	0.703	1.036	1.275	1.427
MAJU	0.276	0.289	0.451	0.605	0.796	1.017	1.297
MAL2	0.163	0.363	0.799	0.975	1.253	1.490	1.630
PTVL	0.032	0.057	0.173	0.254	0.231	0.372	0.289
Mean	0.134	0.224	0.439	0.616	0.776	0.899	1.005

Table 6.10 Statistics of predictions for GE ISB from the first day to the seventh day in GPS week 1972 from Oct. 22 to 28 (from 1st day to 7th day), 2017 (unit: ns).

Station ID	1 st	2 nd	3 rd	4 th	5 th	6 th	7 th
CAS1	0.079	0.135	0.228	0.255	0.325	0.410	0.641
KRGG	0.094	0.084	0.223	0.262	0.209	0.104	0.056
MAJU	0.058	0.062	0.184	0.238	0.364	0.310	0.242
MAL2	0.096	0.214	0.233	0.322	0.413	0.696	0.853
POHN	0.322	0.419	0.552	0.666	1.008	1.144	1.279
REUN	0.048	0.062	0.026	0.060	0.112	0.208	0.365
Mean	0.116	0.163	0.241	0.300	0.405	0.479	0.573

6.4.5 Analysis of convergence time and PPP accuracy

Since the mean prediction RMS of the ISB on the first day of GPS week 1972 (Oct. 22, 2017) is approximately 0.134 ns for GC case and 0.116 in GE case, the accuracy is high that we can consider the ISB as an a priori information. In accordance with the accuracy of the a priori information, it can be segregated into two cases: utilizing ISB as an a priori constraint, or a known parameter in the observation equation. These two kinds of a priori information have the same point, which is the a priori value of ISB is used with the predicted ISB of each station mentioned above; nonetheless, they also have different points, and the difference between them is located at the level of constraint accuracy; in addition, the accuracy of the former one is set as the precision of ISB prediction, and the latter one makes use of a sufficiently high accuracy for fixing the ISB. For the purpose of investigating the impacts of these two types of a priori information on the convergence time and accuracy of combined PPP, here three schemes are designed as hereunder:

- Scheme 1, normal combined PPP model estimated ISB as an unknown without an a priori information (Normal);
- Scheme 2, combined PPP model estimated ISB as an unknown with an a priori constraint (Cons.);
- Scheme 3, combined PPP model considered ISB as a known parameter (Fix).

The offset, derived from the difference between combined PPP result and truth value (IGS weekly solution), is analyzed for the convergence time and accuracy of PPP. With regard to the exact time of convergence, until now there has been no clear definition. Nevertheless, in this study, a common criterion is applied, defining the convergence time as the moment when the error of positioning is below 0.1 m in each of the components of North (N), East (E), and Up (U). As this initial convergence point has been figured out, considering the reliability of this criterion, it is deemed as essential to check the errors of next 50 epochs following this point.

If all of them are below 0.1 m, the initial convergence epoch can be defined as the true convergence time.

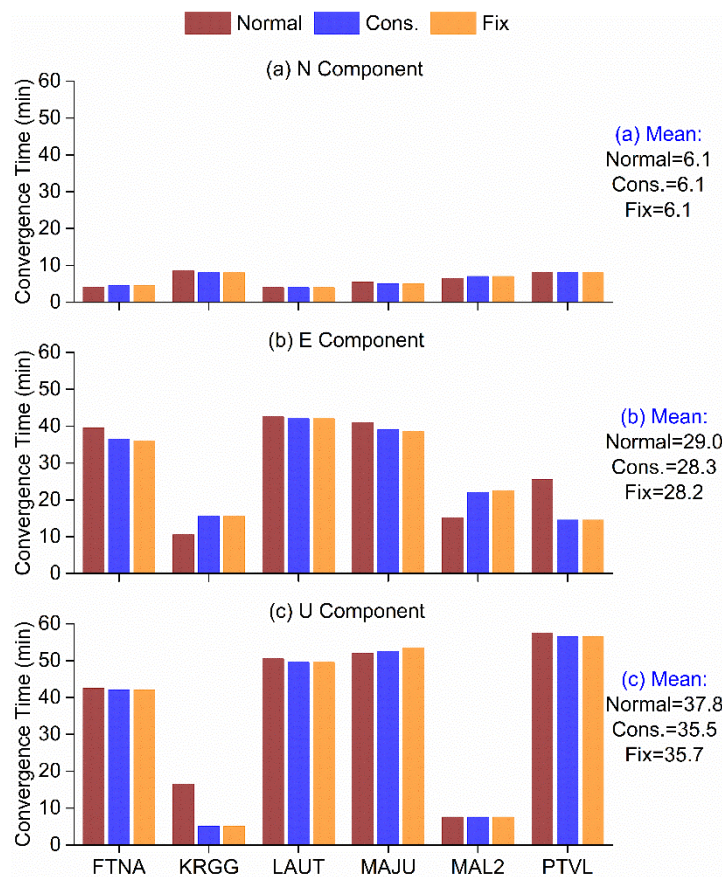


Figure 6.16 Comparison of the convergence time with three schemes (“Normal” in wine color column is the scheme 1, “Cons.” in blue color indicates scheme 2, and “Fix” with orange color denotes scheme 3) in N, E, and U components at stations FTNA, KRGG, LAUT, MAJU, MAL2, and PTVL on Oct. 22, 2017 for GC case.

Figure 6.16 sheds light on the convergence time in three different schemes for GC case. It can be noticed that the mean convergence time of scheme “Normal” is 6.1, 29.0, and 37.8 min in N, E, and U components, respectively. In scheme “Cons.,” the average convergence time is 6.1, 28.3, 35.5 min in three components. While making use of scheme “Fix,” the mean convergence time in three components is 6.1, 28.2, and 35.7 min, respectively. That is why the convergence time of scheme “Cons.” and “Fix” is quite close. In comparison with the scheme “Normal”, we discover the fact that the convergence times of scheme “Cons.” and

“Fix” are primarily enhanced in U component, which can reach 6.1% in GC case. Apparently, the convergence time for stations “KRGG” and “MAL2” are much shorter as compared with other stations in U component. The reason is perhaps caused by the distribution of the stations, and the geometry of the satellites in view. The same phenomenon is occurring in Figure 6.17 as well, which illustrates the convergence time for the GE case. The improvement of convergence times in U component with scheme “Cons.” and “Fix” can achieve 7.4% for GE case.

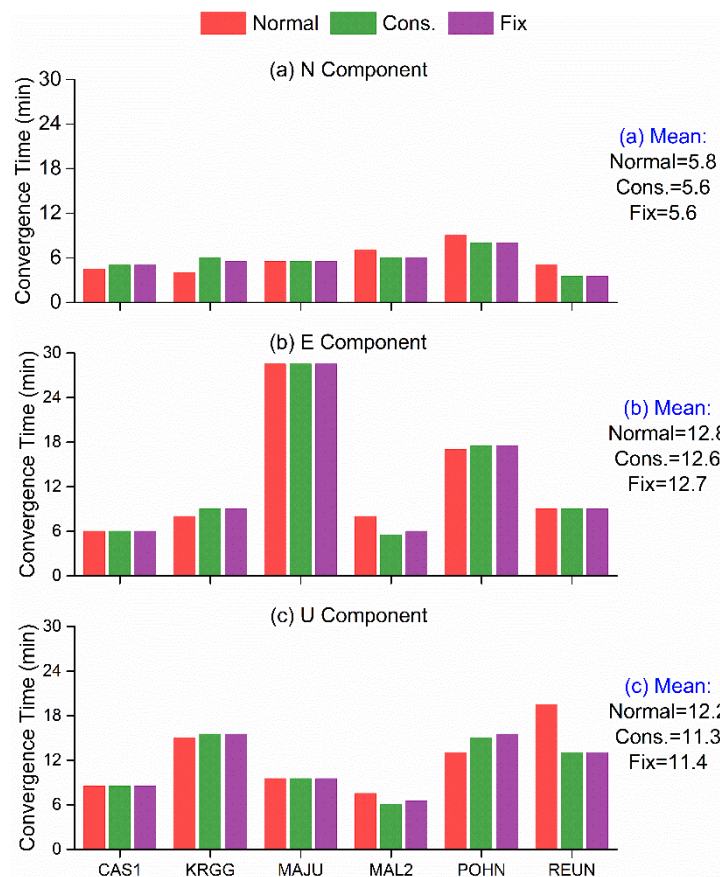


Figure 6.17 Comparison of the convergence time with three schemes (“Normal” in red color column indicates the scheme 1, “Cons.” in olive color denotes scheme 2, and “Fix” with violet color is a representation of scheme 3) in N, E, and U components at stations CAS1, KRGG, MAJU, MAL2, POHN and REUN on Oct. 22, 2017 for GE case.

Table 6.11 Statistics of the accuracy of combined PPP for the GC case with different schemes in N, E, and U components (unit: cm).

Scheme	Normal			Cons.			Fix		
	N	E	U	N	E	U	N	E	U
FTNA	1.41	1.67	2.02	1.41	1.52	1.99	1.40	1.49	1.97
KRGG	0.51	0.89	0.84	0.49	0.84	0.85	0.48	0.82	0.86
LAUT	1.68	1.34	2.33	1.68	1.35	2.34	1.68	1.36	2.34
MAJU	1.39	0.87	3.77	1.39	0.83	3.78	1.42	0.88	3.80
MAL2	0.71	0.91	1.16	0.70	1.08	1.15	0.71	1.31	1.20
PTVL	0.57	0.74	1.58	0.55	0.45	1.51	0.54	0.44	1.51
Mean	1.05	1.07	1.95	1.04	1.01	1.93	1.03	1.05	1.95

Table 6.12 Statistics of the accuracy of combined PPP for the GE case with different schemes in N, E, and U components (unit: cm).

Scheme	Normal			Cons.			Fix		
	N	E	U	N	E	U	N	E	U
CAS1	0.46	0.33	1.34	0.46	0.33	1.33	0.46	0.33	1.33
KRGG	0.52	0.92	0.65	0.49	0.90	0.65	0.49	0.87	0.65
MAJU	1.32	0.64	3.16	1.31	0.69	3.16	1.31	0.69	3.16
MAL2	0.60	1.20	0.60	0.59	0.97	0.76	0.59	0.98	0.75
POHN	1.51	2.48	3.56	1.51	2.56	3.52	1.49	2.77	3.40
REUN	1.06	0.17	1.87	1.07	0.14	1.84	1.07	0.14	1.83
Mean	0.91	0.96	1.86	0.91	0.93	1.88	0.90	0.96	1.85

With regard to the accuracy of combined PPP, we perform a comparison of the results of the three different schemes in GC and GE cases. The statistics of RMS are shown in Table 6.11, and Table 6.12, respectively. As indicated by both tables, the mean RMS of combined PPP in GC and GE case are quite similar between all of the three schemes in N, E, U components. It can be known that in comparison with the normal PPP mode with estimating

ISB, the combined PPP with an a priori information (both scheme “Cons,” and “Fix”) primarily improve the convergence speed in U component, besides being able to attain the same accuracy level as scheme “Normal”.

6.5 Summary

ISB is considered as the key point on the combined PPP with multi-GNSS observations, so it requires full calibration. Typically, ISB is estimated as an unknown together with other parameters in integrated PPP solutions. In this contribution, we have proposed an ISB model with GPS and BDS, GPS and Galileo observations. The initial ISB series is derived from the combined PPP model using the data during GPS week 1971 with 26 stations from the MGEX network. Nonetheless, in this series, there is not only initialization impact, but also ISB jumps, and outliers. Aimed at removing these three types of effects, at first, we apply the combined filter for the elimination of the impact of the convergence period to obtain the original ISB series (ISB_o); thereafter, the precise clock product preprocessing is carried out to wipe off the ISB jumps for the formation of the processed ISB series (ISB_p); eventually, a sliding window median filter is utilized for the removal of ISB jumps from ISB_p and generate the smoothed ISB series (ISB_s). Subsequent to the investigation of the attributes of the ISB_s, we propose an ISB model, which is based on one-week period data, normally containing a polynomial with quadratic-term, in addition to the first-order-term and constant-term, and some periodic functions with different periods.

In order to detect the periods of the periodic function, a frequency spectrum methodology is employed. With regard to the coefficients of the polynomial and the periodic functions, we apply the least squares (LS) methodology for estimating them. Subsequently, we make use of ISB_s as a true value for the verification of the precision of ISB_m derived from the model. It is known that the offset between ISB_m and ISB_s closely adheres to a normal distribution, and ISB_m agrees well with ISB_s. The fitting accuracy of the ISB model for GC case is 0.048

ns, and that for GE case it is 0.024 ns. The normal distribution of difference and the accuracy level implies that the ISB model proposed has high fitting accuracy and is appropriate for ISB prediction.

Data from the following week (GPS week 1972) for the same stations are processed for the prediction with the model. In comparison with the predicted ISB series (ISB_p) with ISB_s, we discover the fact that the prediction accuracy during the one-week period undergoes a decline with the length of the period. The mean RMS values for all stations on the first day have the highest level, which has the potential to reach 0.134 ns in GC case, while in GE case it is 0.116 ns. Accordingly, we recommend a predicting duration of one day.

Aimed at verifying the benefit associated with the ISB model for the combined PPP, we design three schemes or testing. In comparison with scheme "Normal", the convergence time of scheme "Cons." and "Fix" can be shortened primarily in N component by 6.1%, 7.4% for GC, and GE case, respectively. As the findings suggest, all of the three schemes are capable of attaining the same level of PPP accuracy. The integrated PPP with scheme "Cons." and "Fix" without estimated ISB has the capability of making a good substitute for the "Normal" PPP mode. In particular, subjected to some extreme circumstances without sufficient satellite observations, such as in the valley, the downtown of the city, the PPP model with an a priori information of ISB is still likely to attain results because it avoids the rank deficiency without the estimation of ISB.

7 Conclusions and outlooks

7.1 Conclusions

With the development of multi-GNSS, the model of multi-systems combined precise point positioning requires carefully considering the differences existing between different systems. The ISB is introduced for the purpose of covering these differences, indicating that it constitutes the key point realizing the interoperability and compatibility between different constellations. Accordingly, ISB requires careful calibration. Normally, the calibration methodology deals with considering it as an unknown parameter and estimating it together with other parameters in PPP solutions. In this thesis, we made use of a new and different calibration approach for setting up a model for ISB. ISB modeling is based on the data of the estimated ISB series from PPP processing.

The ISB estimation accuracy has a significant association with its function model and stochastic model. At first, we comprehensively introduced and compared two different function models (MIS and MDS) for ISB, and the equivalence proof of these two models was successfully carried out in theory as well. For the purpose of further investigating this equivalence, experiments were carried out. Both in the cases of GPS/BDS and GPS/Galileo, the accuracy and convergence time of positioning with two models were evaluated, reaching almost equal results. The comparison of ISB derived from two models was carried out; the difference in GPS/BDS experiment was about 1 cm in the distance; while for the GPS/Galileo case, it amounted to be 0.9mm, further verifying the equivalence of these two models.

In addition to investigating the function model, we carried out the discussion of the stochastic model as well. Four different stochastic models were assessed and studied comprehensively. For the purpose of further reveal the impact of ISB on the positioning, the model without introducing ISB (ISB-OFF) was also performed, i.e., five different schemes,

including ISB-OFF, ISB-PW, ISB-RW, ISB-AD, and ISB-WN, were designed for testing in this study. As the results of pseudorange residuals suggest, it can be noticed that, through the consideration of ISB, the RMS of ionosphere-free combined pseudorange is smaller as compared with that without ISB (ISB-OFF). The results of convergence time and positioning accuracy analysis shed light on the fact that the PPP performance of ISB-AD, considered ISB as arc-dependent constant, is even worse as compared with ISB-OFF with the use of the *GBM* precise products from the analysis center GFZ, the strategies of regarding ISB as random walk (ISB-RW), and considering as white noise (ISB-WN) attain the best results. With regard to the *WUM* products from Wuhan University, a completely different result is achieved. The PPP with ISB as a piece-wise constant (ISB-PW) and ISB-AD delivers the best performance. The most likely reason was whether the ISB stochastic models applied by the analysis center and PPP users showed consistency. Accordingly, it was recommended to utilize ISB-RW, or ISB-WN when *GBM* products were used; in addition, for the *WUM* products, ISB-PW, or ISB-AD was chosen. From the statistics of PPP precision during the convergence period, it can be concluded that considering ISB also had a significant improvement on the combined PPP accuracy during the initialization phase.

Following the estimation of the ISB series by the PPP processing, we discovered the fact that there are both jumps and outliers inside. If we required modeling ISB at higher accuracy, the basis was getting a continuous and smooth data series. That is why we applied a methodology of the precise clock product preprocessing to detect and repair the ISB jumps since ISB was strongly correlated with the satellite clock. We also figured it out that the actual reason leading to ISB gaps was caused by the extreme points (maximum or minimum points) of satellite clock data in the frequency domain. The larger jumps were conveniently found out from the frequency domain clock figure directly; besides that, for the smaller extreme points detection, a robust estimation methodology with the median filter was applied. Subsequent to that, all of these extreme points were classified into three kinds. For each of the types, we applied a different preprocessing methodology, and the test of ISB continuity illustrated the

significance associated with the satellite clock product preprocessing. Because in comparison with the results without preprocessing, ISB jumps have been effectively repaired, the improvement of ISB continuity in 4 days-pairs has the potential to reach 62.4%, 79.5%, 99.6%, and 99.0%, respectively. In this manner, if the appropriate satellite clock preprocessing were employed, ISB jumps could be efficiently detected and repaired.

Ultimately, on the basis of the above research works dealing with the function model, stochastic model, and precise clock product preprocessing, a high accuracy, smooth and sequential ISB series can be attained. It was put to use as the essential data for the establishment of the ISB model. The fitting accuracy of the ISB model was tested as well; with regard to GC case, it is 0.048 ns, whereas, for the GE case, it amounts to be 0.024 ns. It was indicated that the ISB model proposed had high fitting accuracy, in addition to being appropriate for ISB prediction. In a comparison of the predicted ISB series (ISB_p) from the model with ISB_s, it can be found that the prediction accuracy during the one-week period underwent a gradual decline. The mean RMS values for all stations on the first day have the highest level, which is able to attain 0.134 ns in GC case; on the other hand, with regard to GE case, it was 0.116 ns. Therefore, the optimal predicting duration was one day. We designed three schemes for the purpose of testing the impact of the ISB model for the combined PPP. In comparison with scheme "Normal", the convergence time of scheme "Cons." and "Fix" can be lowered primarily in N component by 6.1%, 7.4% for GC, and GE case, respectively. With regard to the results of PPP accuracy, it is evident that all of the three schemes are capable of attaining the same level. In this manner, it suggests that the integrated PPP with scheme "Cons." and "Fix" without estimated ISB can take a good place as the "Normal" PPP mode. Even in some extreme cases without sufficient observations, for instance, in the valley, the downtown of the city, the PPP model with an a priori information of ISB is still likely to keep the results output, since it avoided the rank deficiency without the estimation of the extra ISB parameter.

7.2 Outlooks

Following the research progress and achievements of this thesis, several points and ideas for future studies can be considered and proposed at least in the following aspects.

At first, the ISB model proposed in this thesis is based on a short period of one week; it can only demonstrate the short-term characteristic of ISB. If the ISB can be modeled with a longer period, it will contain more details and has a higher modeling accuracy. Also, this thesis is mainly focused on the data processing on GPS/BDS, and GPS/Galileo, in the future, the further study of inter-frequency bias and ISB of GPS/GLONASS can be made. Ultimately, ionosphere-free combined observation is utilized for PPP processing and ISB estimating; we can also try to use uncombined data to investigate the ISB characteristic.

References:

- Abdel-Salam M A-t. (2005). Precise point positioning using un-differenced code and carrier phase observations.
- Barnes J B. (2000). Real time kinematic GPS and multipath: characterisation and improved least squares modelling. University of Newcastle upon Tyne.
- Bergland G D. (1969). A guided tour of the fast Fourier transform. *IEEE Spectrum*, 6(7):41-52. doi: 10.1109/mspec.1969.5213896.
- Bierman G J. (2006). Factorization methods for discrete sequential estimation. Courier Corporation.
- Bisnath S, Wells D, Dodd D. (2003). Evaluation of commercial carrier phase-based WADGPS services for marine applications. In: the 16th International Technical Meeting of the Satellite Division of The Institute of Navigation (ION GPS/GNSS 2003), pp. 17-27.
- Blewitt G. (1989). Carrier phase ambiguity resolution for the Global Positioning System applied to geodetic baselines up to 2000 km. *Journal of Geophysical Research Solid Earth*, 94(B8):10187-10203.
- Böhm J, Niell A, Tregoning P, Schuh H. (2006). Global Mapping Function (GMF): A new empirical mapping function based on numerical weather model data. *Geophysical Research Letters*, 33(7).
- Böhm J, Schuh H. (2004). Vienna mapping functions in VLBI analyses. *Geophysical Research Letters*, 31(1).
- Bree R J P V, Tiberius C C J M. (2012). Real-time single-frequency precise point positioning: accuracy assessment. *GPS Solutions*, 16(2):259-266.
- Brunner F, Hartinger H, Troyer L. (1999). GPS signal diffraction modelling: the stochastic SIGMA- Δ model. *Journal of Geodesy*, 73(5):259-267.
- Cai C, Gao Y. (2013). Modeling and assessment of combined GPS/GLONASS precise point positioning. *GPS Solutions*, 17(2):223-236.
- Chen J, Wang J, Zhang Y, Yang S, Chen Q, Gong X. (2016). Modeling and Assessment of GPS/BDS Combined Precise Point Positioning. *Sensors*, 16(7):1151.
- Choy S, Bisnath S, Rizos C. (2017). Uncovering common misconceptions in GNSS Precise Point Positioning and its future prospect. *GPS Solutions*, 21(1):13-22. doi: 10.1007/s10291-016-0545-x.

- Dach R, Schaer S, Lutz S, Meindl M, Beutler G. (2010). Combining the Observations from Different GNSS. *Agu Fall Meeting Abstracts*, 12.
- Dach R, Walser P. (2015). *Bernese GNSS Software Version 5.2*.
- Defraigne P, Bruyninx C. (2007). On the link between GPS pseudorange noise and day-boundary discontinuities in geodetic time transfer solutions. *GPS Solutions*, 11(4):239-249.
- Defraigne P, Bruyninx C, Guyennon N. (2007a). GLONASS and GPS PPP for time and frequency transfer. In: *EFTF '07, Geneva, Switzerland*, pp. 909-913.
- Defraigne P, Guyennon N, Bruyninx C. (2007b). GPS Time and Frequency Transfer: PPP and Phase-Only Analysis. In: *the IEEE International Frequency Control Symposium Jointly with the 21st European Frequency and TimeForum (EFTF '07)*, pp. 904-908.
- Dow J M, Neilan R E, Rizos C. (2009). The International GNSS Service in a changing landscape of Global Navigation Satellite Systems. *Journal of Geodesy*, 83(7):689.
- Duhamel P, Vetterli M. (1990). Fast Fourier-Transforms - a Tutorial Review and a State-of-the-Art. *Signal processing*, 19(4):259-299. doi: Doi 10.1016/0165-1684(90)90158-U.
- Flohrer C. (2008). Mutual Validation of Satellite-geodetic Techniques and Its Impact on GNSS Orbit Modeling. *Inst. für Geodäsie und Photogrammetrie*.
- Gao Y, Wojciechowski A, Chen K. (2005). Airborne kinematic positioning using precise point positioning methodology. *Geomatica*, 59(1):29-36.
- Ge M, Gendt G, Rothacher M, Shi C, Liu J. (2008). Resolution of GPS carrier-phase ambiguities in Precise Point Positioning (PPP) with daily observations. *Journal of Geodesy*, 82(7):389-399.
- Geng J, Meng X, Dodson A H, Teferle F N. (2010a). Integer ambiguity resolution in precise point positioning: method comparison. *Journal of Geodesy*, 84(9):569-581.
- Geng J, Teferle F N, Meng X, Dodson A H. (2010b). Kinematic precise point positioning at remote marine platforms. *GPS Solutions*, 14(4):343-350.
- Geng J, Teferle F N, Meng X, Dodson A H. (2011). Towards PPP-RTK: Ambiguity resolution in real-time precise point positioning. *Advances in Space Research*, 47(10):1664-1673. doi: <https://doi.org/10.1016/j.asr.2010.03.030>.
- Geng J H, Shi C, Ge M R, Dodson A H, Lou Y D, Zhao Q L, Liu J N. (2012). Improving the estimation of fractional-cycle biases for ambiguity resolution in precise point positioning. *Journal of Geodesy*, 86(8):579-589. doi: DOI 10.1007/s00190-011-0537-0.
- Ghilani C D. (2017). *Adjustment computations: spatial data analysis*. John Wiley & Sons.

- Gioia C, Borio D. (2016). A statistical characterization of the Galileo-to-GPS inter-system bias. *Journal of Geodesy*, 60:1279-1291.
- Gu S, Lou Y, Shi C, Liu J. (2015a). BeiDou phase bias estimation and its application in precise point positioning with triple-frequency observable. *Journal of Geodesy*, 89(10):979-992. doi: 10.1007/s00190-015-0827-z.
- Gu S, Shi C, Lou Y, Liu J. (2015b). Ionospheric effects in uncalibrated phase delay estimation and ambiguity-fixed PPP based on raw observable model. *Journal of Geodesy*, 89(5):447-457.
- Guo F, Li X, Zhang X, Wang J. (2017). Assessment of precise orbit and clock products for Galileo, BeiDou, and QZSS from IGS Multi-GNSS Experiment (MGEX). *GPS Solutions*, 21(1):279-290. doi: 10.1007/s10291-016-0523-3.
- Guo J, Xu X, Zhao Q, Liu J. (2016). Precise orbit determination for quad-constellation satellites at Wuhan University: strategy, result validation, and comparison. *Journal of Geodesy*, 90(2):143-159. doi: 10.1007/s00190-015-0862-9.
- Hackel S, Steigenberger P, Hugentobler U, Uhlemann M, Montenbruck O. (2014). Galileo orbit determination using combined GNSS and SLR observations. *GPS Solutions*, 19(1):15-25.
- He H, Li J, Yang Y, Xu J, Guo H, Wang A. (2014). Performance assessment of single- and dual-frequency BeiDou/GPS single-epoch kinematic positioning. *GPS Solutions*, 18(3):393-403. doi: 10.1007/s10291-013-0339-3.
- Héroux P, Kouba J, Collins P, Lahaye F. (2001). GPS Carrier-Phase Point Positioning with Precise Orbit Products. *Proceedings of the Kis*.
- Herring T, King R, McClusky S. (2010). Documentation of the GAMIT GPS Analysis Software release 10.4. Department of Earth and Planetary Sciences, Massachusetts Institute of Technology, Cambridge, Massachusetts:1-171.
- Hofmann-Wellenhof B, Lichtenegger H, Wasle E. (2008). *GNSS — Global Navigation Satellite Systems*. Springer.
- Hopfield H. (1969). Two-quartic tropospheric refractivity profile for correcting satellite data. *Journal of Geophysical research*, 74(18):4487-4499.
- Ishijima Y, Inaba N, Matsumoto A, Terada K, Yonechi H, Ebisutani H, Ukawa S, Okamoto T. (2009). Design and Development of the First Quasi-Zenith Satellite Attitude and Orbit Control System. In: *Proceedings of the IEEE Aerospace Conference*, Big Sky, MT, USA.
- Jiang N, Xu Y, Xu T, Xu G, Sun Z, Schuh H. (2017). GPS/BDS short-term ISB modelling and prediction. *GPS Solutions*, 21(1):163-175.

- Jr P S D O, Morel L, Fund F, Legros R, Monico J F G, Durand S, Durand F. (2017). Modeling tropospheric wet delays with dense and sparse network configurations for PPP-RTK. *GPS Solutions*, 21(1):237-250.
- Kalman R E. (1960). A new approach to linear filtering and prediction problems. *Journal of basic Engineering*, 82(1):35-45.
- Klobuchar J A. (1987). Ionospheric time-delay algorithm for single-frequency GPS users. *IEEE Transactions on aerospace and electronic systems*(3):325-331.
- Koch K-R. (2013). *Parameter estimation and hypothesis testing in linear models*. Springer Science & Business Media.
- Koch K, Yang Y. (1998). Robust Kalman filter for rank deficient observation models. *Journal of Geodesy*, 72(7-8):436-441.
- Kouba J. (2002). A Guide to Using International GPS Service (IGS) Products. Taken from IGS Website), 4(3):106.
- Kouba J. (2009). A guide to using International GNSS Service (IGS) Products. *International GNSS Service (IGS)*.
- Kouba J, Héroux P. (2001). Precise Point Positioning Using IGS Orbit and Clock Products. *GPS Solutions*, 5(2):12-28.
- Leick A, Beser J, Rosenboom P, Wiley B. (1998). Assessing GLONASS observation. In: *ION GPS 1998*, Nashville, TN, pp. pp 1605–1612.
- Leick A, Rapoport L, Tatarnikov D. (2015). *GPS Satellite Surveying*, Fourth Edition.
- Li P, Zhang X. (2014). Integrating GPS and GLONASS to accelerate convergence and initialization times of precise point positioning. *GPS Solutions*, 18(3):461-471. doi: 10.1007/s10291-013-0345-5.
- Li X, Ge M, Dai X, Ren X, Fritsche M, Wickert J, Schuh H. (2015a). Accuracy and reliability of multi-GNSS real-time precise positioning: GPS, GLONASS, BeiDou, and Galileo. *Journal of Geodesy*, 89(6):607-635. doi: 10.1007/s00190-015-0802-8.
- Li X, Zhang X, Ren X, Fritsche M, Wickert J, Schuh H. (2015b). Precise positioning with current multi-constellation Global Navigation Satellite Systems: GPS, GLONASS, Galileo and BeiDou. *Sci Rep*, 5:8328. doi: 10.1038/srep08328.
- Li X, Zhang X, Ren X, Fritsche M, Wickert J, Schuh H. (2015c). Precise positioning with current multi-constellation Global Navigation Satellite Systems: GPS, GLONASS, Galileo and BeiDou. *Scientific Reports*, 5:8328.

- Li X, Zus F, Lu C, Dick G, Ning T, Ge M, Wickert J, Schuh H. (2015d). Retrieving of atmospheric parameters from multi-GNSS in real time: Validation with water vapor radiometer and numerical weather model. *Journal of Geophysical Research Atmospheres*, 120(14):7189-7204.
- Li X, Zus F, Lu C, Ning T, Dick G, Ge M, Wickert J, Schuh H. (2015e). Retrieving high-resolution tropospheric gradients from multiconstellation GNSS observations. *Geophysical Research Letters*, 42(10):4173-4181.
- Liu T, Yuan Y, Zhang B, Wang N, Tan B, Chen Y. (2017). Multi-GNSS precise point positioning (MGPPP) using raw observations. *Journal of Geodesy*, 91(3):253-268. doi: 10.1007/s00190-016-0960-3.
- Lou Y, Zheng F, Gu S, Wang C, Guo H, Feng Y. (2016). Multi-GNSS precise point positioning with raw single-frequency and dual-frequency measurement models. *GPS Solutions*, 20(4):849-862.
- Lu C, Li X, Nilsson T, Ning T, Heinkelmann R, Ge M, Glaser S, Schuh H. (2015). Real-time retrieval of precipitable water vapor from GPS and BeiDou observations. *Journal of Geodesy*. doi: 10.1007/s00190-015-0818-0.
- Mann K A, Werner F W, Palmer A K. (1989). Frequency spectrum analysis of wrist motion for activities of daily living. *J Orthop Res*, 7(2):304-306. doi: 10.1002/jor.1100070219.
- Marques H A, Monico J F, Aquino M. (2011). RINEX_HO: second-and third-order ionospheric corrections for RINEX observation files. *GPS Solutions*, 15(3):305-314.
- Melbourne W. (1985). The case for ranging in GPS-based geodetic systems. In: *Proceedings of the first international symposium on precise positioning with the global positioning system*. In: Commerce U S D o (ed), Rockville, MD, pp. pp 373-386.
- Melgard T, Vigen E, Jong K D, Lapucha D, Visser H, Oerpen O. (2009). G2-the first real-time GPS and GLONASS precise orbit and clock service. In: *the 22nd International Technical Meeting of The Satellite Division of the Institute of Navigation (ION GNSS 2009)*, pp. 1885-1891.
- Mikhail E M, Ackermann F E. (1976). *Observations and least squares*.
- Montenbruck O, Hauschild A, Hessels U. (2011). Characterization of GPS/GIOVE sensor stations in the CONGO network. *GPS Solutions*, 15(3):193-205. doi: 10.1007/s10291-010-0182-8.

- Montenbruck O, Helleputte T V, Kroes R, Gill E. (2005). Reduced dynamic orbit determination using GPS code and carrier measurements. *Aerospace Science & Technology*, 9(3):261-271.
- Montenbruck O, Schmid R, Mercier F, Steigenberger P, Noll C, Fatkulin R, Kogure S, Ganeshan A S. (2015). GNSS satellite geometry and attitude models. *Advances in Space Research*, 56(6):1015-1029.
- Montenbruck O, Steigenberger P, Khachikyan R, Weber G, Langley R, Mervart L, Hugentobler U. (2014). IGS-MGEX: preparing the ground for multi-constellation GNSS science. *Inside GNSS*, 9(1):42-49.
- Montenbruck O, Steigenberger P, Khachikyan R, Weber G, Langley R B, Mervart L, Hugentobler U. (2013). IGS-MGEX: preparing the ground for multi-constellation GNSS science. In: 4th Int. Colloquium on Scientific and Fundamental Aspects of the Galileo System, Prague.
- Montenbruck O, Steigenberger P, Prange L, Deng Z, Zhao Q, Perosanz F, Romero I, Noll C, Stürze A, Weber G, Schmid R, MacLeod K, Schaer S. (2017). The Multi-GNSS Experiment (MGEX) of the International GNSS Service (IGS) – Achievements, prospects and challenges. *Advances in Space Research*, 59(7):1671-1697. doi: <https://doi.org/10.1016/j.asr.2017.01.011>.
- Nadarajah N, Teunissen P J G, Raziq N. (2013). BeiDou Inter-Satellite-Type Bias Evaluation and Calibration for Mixed Receiver Attitude Determination. *Sensors*, 13(7):9435-9463.
- Nadarajah N, Teunissen P J G, Raziq N. (2014). Instantaneous BeiDou-GPS attitude determination: A performance analysis. *Advances in Space Research*, 54(5):851-862.
- Nadarajah N, Teunissen P J G, Sleewaegen J-M, Montenbruck O. (2015). The mixed-receiver BeiDou inter-satellite-type bias and its impact on RTK positioning. *GPS Solutions*, 19(3):357-368. doi: 10.1007/s10291-014-0392-6.
- Niell A. (1996). Global mapping functions for the atmosphere delay at radio wavelengths. *Journal of Geophysical Research: Solid Earth*, 101(B2):3227-3246.
- Niell A. (2001). Preliminary evaluation of atmospheric mapping functions based on numerical weather models. *Physics and Chemistry of the Earth, Part A: Solid Earth and Geodesy*, 26(6-8):475-480.
- Odijk D, Zhang B, Khodabandeh A, Odolinski R, Teunissen P J. (2016). On the estimability of parameters in undifferenced, uncombined GNSS network and PPP-RTK user models by means of S-system theory. *Journal of Geodesy*, 90(1):15-44.
- Odolinski R, Teunissen P J G, Odijk D. (2015a). Combined BDS, Galileo, QZSS and GPS single-frequency RTK. *GPS Solutions*, 19(1):151-163. doi: 10.1007/s10291-014-0376-6.

- Odolinski R, Teunissen P J G, Odijk D. (2015b). Combined GPS plus BDS for short to long baseline RTK positioning. *Measurement Science & Technology*, 26(4).
- Paziewski J, Wielgosz P. (2014). Assessment of GPS + Galileo and multi-frequency Galileo single-epoch precise positioning with network corrections. *GPS Solutions*, 18(4):571-579. doi: 10.1007/s10291-013-0355-3.
- Paziewski J, Wielgosz P. (2015). Accounting for Galileo–GPS inter-system biases in precise satellite positioning. *Journal of Geodesy*, 89(1):81-93. doi: 10.1007/s00190-014-0763-3.
- Petit G, Luzum B. (2010). IERS Conventions (2010). In: IERS Technical Note 36. Verlag des Bundesamts für Kartographie und Geodäsie, Frankfurt am Main.
- Petit G, Luzum B, Ai E. (2010). IERS Conventions (2010). Iers Technical Note, 36:1 - 95.
- Raby P, Daly P. (1993). Using the GLONASS system for geodetic survey. In: *Navigation I o* (ed), ION GPS 1993. Institute of Navigation, Salt Lake City, UT, pp. pp 1129–1138.
- Rebischung P, Schmid R. (2016). IGS14/igs14.atx: a new framework for the IGS products.
- Revnivykh S. (2010). GLONASS Status and Progress. In: *Proc. ION GNSS 2010*, Institute of Navigation, Poland, Oregon, pp. 609-633.
- Saastamoinen J. (1972). Contributions to the theory of atmospheric refraction. *Bulletin Géodésique (1946-1975)*, 105(1):279-298.
- Schüler T. (2001). On ground-based GPS tropospheric delay estimation. Univ. der Bundeswehr München.
- Schwarz K. (1989). A comparison of GPS kinematic models for the determination of position and velocity along a trajectory. *Manuscripta geodaetica*, 14:345-353.
- Shi C, Gu S, Lou Y, Ge M. (2012a). An improved approach to model ionospheric delays for single-frequency precise point positioning. *Advances in Space Research*, 49(12):1698-1708.
- Shi C, Yi W, Song W, Lou Y, Yao Y, Zhang R. (2013). GLONASS pseudorange inter-channel biases and their effects on combined GPS/GLONASS precise point positioning. *GPS Solutions*, 17(4):439-451.
- Shi C, Zhao Q, Li M, Tang W, Hu Z, Lou Y, Zhang H, Niu X, Liu J. (2012b). Precise orbit determination of Beidou Satellites with precise positioning. *Science China Earth Sciences*, 55(7):1079-1086. doi: 10.1007/s11430-012-4446-8.
- Steigenberger P, Hauschild A, Montenbruck O, Rodriguez-Solano C, Hugentobler U. (2013). Orbit and clock determination of QZS-1 based on the CONGO network. *Navigation*, 60(1):31–40.

- Tegedor J, Øvstedal O, Vigen E. (2014). Precise orbit determination and point positioning using GPS, Glonass, Galileo and BeiDou. *Journal of Geodetic Science*, 4(1):65-73.
- Teunissen P J G. (1996). *GPS carrier phase ambiguity fixing concepts*. Springer Berlin Heidelberg.
- Torre A D, Caporali A. (2014). An analysis of intersystem biases for multi-GNSS positioning. *Gps Solutions*, 19(2):297-307. doi: 10.1007/s10291-014-0388-2.
- Torre A D, Caporali A. (2015). An analysis of intersystem biases for multi-GNSS positioning. *GPS Solutions*, 19(2):297-307. doi: 10.1007/s10291-014-0388-2.
- Wang M, Cai H Z, Pan Z P. (2015). BDS/GPS relative positioning for long baseline with undifferenced observations. *Advances in Space Research*, 55(1):113-124.
- Wei Z, Ge M. (1998). *The Mathematical Model of GPS Relative Positioning*. Surveying and Mapping Press.
- Weiss J P, Bar-Sever Y, Bertiger W, Romans L J. (2010). Near real time precise orbit and clock determination for GLONASS. *Proceedings of International Technical Meeting of the Satellite Division of the Institute of Navigation*, 7672(6):2771-2777.
- Wu J, Wu S, Hajj G, Bertiger W, Lichten S. (1992). Effects of antenna orientation on GPS carrier phase. *Astrodynamic*, 1:1647-1660.
- Xu G. (2002). GPS data processing with equivalent observation equations. *GPS Solutions*, 6(1-2):28-33.
- Xu G, Xu Y. (2016). *GPS: Theory, Algorithms and Applications*. Springer Publishing Company, Incorporated.
- Yang Y. (2010a). Adaptively robust kalman filters with applications in navigation. In: *Sciences of Geodesy-I*. Springer, pp. 49-82.
- Yang Y. (2010b). Progress, Contribution and Challenges of Compass/Beidou Satellite Navigation System. *Acta Geodaetica Et Cartographica Sinica*, 39(1):1-6.
- Yang Y, He H, Xu G. (2001). Adaptively robust filtering for kinematic geodetic positioning. *Journal of Geodesy*, 75(2):109-116. doi: 10.1007/s001900000157.
- Yang Y, Li J, Wang A, Xu J, He H, Guo H, Shen J, Dai X. (2014). Preliminary assessment of the navigation and positioning performance of BeiDou regional navigation satellite system. *Science China Earth Sciences*, 57(1):144-152. doi: 10.1007/s11430-013-4769-0.
- Yang Y, Song L, Xu T. (2002). Robust estimator for correlated observations based on bifactor equivalent weights. *Journal of Geodesy*, 76(6-7):353-358. doi: DOI 10.1007/s00190-002-0256-7.

- Zeng A, Yang Y, Ming F, Jing Y. (2017). BDS–GPS inter-system bias of code observation and its preliminary analysis. *GPS Solutions*, 21(4):1573-1581. doi: 10.1007/s10291-017-0636-3.
- Zhang B-C, Ou J-K, Li Z-S, Yuan Y-B. (2011). Determination of ionospheric observables with precise point positioning. *Chinese Journal of Geophysics (in Chinese)*, 54(4):950-957.
- Zhang B, Liu T, Yuan Y. (2018). GPS receiver phase biases estimable in PPP-RTK networks: dynamic characterization and impact analysis. *Journal of Geodesy*, 92(6):659-674. doi: 10.1007/s00190-017-1085-z.
- Zhang B, Ou J, Yuan Y, Li Z. (2012). Extraction of line-of-sight ionospheric observables from GPS data using precise point positioning. *Science China Earth Sciences*, 55(11):1919-1928.
- Zhao Q, Guo J, Hu Z, Shi C, Liu J. (2013). Initial results of precise orbit and clock determination for COMPASS navigation satellite system. *Journal of Geodesy*, 87(5):475-486.
- Zhao Q, Wang C, Guo J, Wang B, Liu J. (2017). Precise orbit and clock determination for BeiDou-3 experimental satellites with yaw attitude analysis. *GPS Solutions*, 22(1):4. doi: 10.1007/s10291-017-0673-y.
- Zhao S H, Cui X W, Guan F, Lu M Q. (2014). A Kalman Filter-Based Short Baseline RTK Algorithm for Single-Frequency Combination of GPS and BDS. *Sensors*, 14(8):15415-15433.
- Zhou F, Dong D, Ge M, Li P, Wickert J, Schuh H. (2017). Simultaneous estimation of GLONASS pseudorange inter-frequency biases in precise point positioning using undifferenced and uncombined observations. *GPS Solutions*, 22(1):19. doi: 10.1007/s10291-017-0685-7.
- Zhou F, Dong D, Ge M, Li P, Wickert J, Schuh H. (2018). Simultaneous estimation of GLONASS pseudorange inter-frequency biases in precise point positioning using undifferenced and uncombined observations. *GPS Solutions*, 22(1):19.
- Zhou J. (1989). Classical Theory of Errors and Robust Estimation. *Acta Geodaetica et Cartographica Sinica*, 18(2):115-120.
- Zumberge J, Heflin M, Jefferson D, Watkins M, Webb F H. (1997). Precise point positioning for the efficient and robust analysis of GPS data from large networks. *Journal of Geophysical Research: Solid Earth*, 102(B3):5005-5017.

Acknowledgments

The completion of this thesis would not have been possible without the support of many people and organizations.

First of all, I would like to express my profound respect and gratitude to my supervisors, Prof. Dr. Dr. h.c. Harald Schuh at TU Berlin and GFZ, Prof. Prof. h.c. Dr. Guochang Xu formerly at GFZ and now at Shandong University at Weihai, China, for giving me the opportunity to pursue my Ph.D. study at TU Berlin, and supervising this thesis, for their continuous support, guidance and encouragement of my studies and research. Also, I would like to thank Prof. Dr. Jürgen Oberst at TU Berlin for his chairing on my thesis defense. Many special thanks would go to Prof. Dr. Robert Weber from TU Wien for reviewing the thesis and attending the thesis defense, thanks very much for his comments and works which are absolutely beneficial for my thesis.

I will also give my profound respect and gratitude to Prof. Dr. Tianhe Xu at Shandong University at Weihai China for his professional insight and advice on my study which inspires my research interest and enthusiasm. Without his help, this thesis would hardly have been completed.

I would also like to thank my colleagues and friends at TU Berlin, especially Daniel Wujanz, Sven Weisbrich, Daniel Wahl, Georgios Malissiovas, and Mathias Burger, for their help on various procedures and language improvement, as well as Dr. Tianyu Miao, Jinpeng Feng, Xunqiang Gong, Liang Wang, Tiantian Liu for their kindly help, cooperation and discussions. Many thanks are also expressed to the colleagues and students of GFZ and Shandong University at Weihai, Prof. Dr. Hermann Kaufmann, Dr. Nina Bösche, Dr. Kaifei He, Dr. Rui Tu, Dr. Kejie Chen, Min Li, Biao Lu, Jia Xu, Dr. Yujun Du, Dr. Fan Gao, Zhangzhen Sun, Chunhua

Jiang, Jian Wang, Wenfeng Nie, Jing Qiao, Honglei Yang, Yuguo Yang and others, for their kindly help and discussions.

Gratefully acknowledged are the China Scholarship Council (CSC), and the Education Section of the Embassy of the People's Republic of China in the Federal Republic of Germany, for the financial support during my Ph.D. period.

I am indebted to my host university TU Berlin where I was doing my research from 2013 to 2018. GFZ is also thanked for my study during this period. The International GNSS Service (IGS) is thanked for providing GNSS data and products.

Eventually, I would like to express my gratitude to my parents for their endless support and understanding. The persons I wish to thank most are my wife and lovely little son, who support and accompany me, give me courage, confidence, and love all the time.